

**Molecular Engineering and Electrochemical
Characterization of Redox-active Electrolytes for
Aqueous Redox Flow Batteries**

by

Hao Wang

A thesis submitted in partial fulfillment of the requirements for the degree of

Doctor of Philosophy

Department of Chemistry

University of Alberta

© Hao Wang, 2021

Abstract

Energy is one of the most indispensable ingredients in modern economies and is a critical cornerstone for the development of human society. In contrast to carbon-intensive legacy fossil fuels, low-carbon renewable energy sources (such as solar and wind) provide a significant opportunity to alleviate carbon emissions and global anthropogenic climate change. Due to the intermittent nature of solar and wind energy, the need for energy storage to complement these vast but fluctuating sources of wind and solar energy is pressing. Redox flow batteries (RFBs) are promising thanks to their inherent decoupling of stored chemical energy and tunable power density, as well as their low cost, safe operation, and long lifetimes. Traditional inorganic RFBs, such as all-vanadium RFBs, have been studied for over three decades and have undergone successful commercialization. These batteries are, however, subject to problematic issues related to their chemistry, including corrosivity (e.g., sulfuric acid is the solvent), cost (ca. \$27/kg for vanadium (V) oxide raw material and \$500/m² for Nafion membranes), parasitic reactions, and crossover of electrolytes that reduces efficiency. RFBs based on organic electrolytes may be promising alternatives for the next-generation of aqueous RFBs due to the tunability of their chemical and physical properties. To achieve high performance aqueous flow batteries, much development is needed as well as detailed fundamental studies of the electrochemical properties of these redox electrolytes. This thesis focuses on developing new organic materials and improved electrochemical methods for the next generations of aqueous RFBs for storage of low-carbon energy.

The thesis can be divided into two parts. In the first part of the thesis, mathematical modeling was applied to simulate the electrochemical behavior of electrochemically reversible, quasi-reversible, and irreversible systems by using different electrochemical techniques. The advantages and limitations of these electrochemical methods to acquire kinetics parameters were analyzed and discussed, and their limitations addressed and reconsidered. The result of this work was a new method and protocols to obtain electrochemical rate constants and diffusion

coefficients for both reduced and oxidized species. The effects of heterogeneous rate constants of redox compounds on the performance of the flow batteries also were simulated and evaluated.

In the second part, a water-soluble octahedral bis(imino)pyridine cobalt complex was synthesized. Due to the introduction of carboxylic groups to the bis(imino)pyridine ligand periphery, the complex is water soluble, with two redox couples within the water splitting window. Its electrochemical kinetics, pH-dependent cyclic voltammetric behavior, and solubility in the water solution were investigated thoroughly. Symmetric aqueous RFBs with the complex acting as both catholyte and anolyte were fabricated, and they were found to have high capacity retention and good Coulombic efficiencies over 100 cycles. Upon completion of this work on the cobalt complex, the project was extended to a series of phenazine derivatives with different numbers of sulfonated terminated short carbon chains that were designed and prepared. The redox potentials, solubility, and stability of the phenazine moieties are modulated through the tailoring of the number and position of the functional groups. The electrochemical properties and the performance of full cell aqueous RFBs also were investigated.

Preface

This thesis comprises five chapters. Chapter 1 provides a short introduction to redox flow batteries (RFBs), with a focus on aqueous systems. Chapter 2 discusses the limitations of very commonly applied electrochemical techniques to determine kinetic parameters of RFBs and related electrochemical systems and provides a protocol that better elucidates the kinetics of redox-active species. Chapter 3 investigates the electrochemical properties of a water-soluble octahedral bis(imino)pyridine cobalt complex and its performance in symmetric aqueous flow batteries. Chapter 4 introduces a new water-soluble phenazine derivative as an anolyte for aqueous flow batteries. Chapter 5 summarizes the thesis and suggests some research direction for future work.

The work presented in Chapter 2 is based on the publication: Wang, H.; Sayed, S. Y.; Lubner, E. J.; Olsen, B. C.; Shirurkar, S. M.; Venkatakrishnan, S.; Tefashe, U. M.; Farquhar, A. K.; Smotkin, E. S.; McCreery, R. L.; Buriak, J. M., Redox Flow Batteries: How to Determine Electrochemical Kinetic Parameters. *ACS Nano* 2020, 14 (3), 2575-2584. Dr. Sayed Youssef Sayed and I wrote the initial manuscript draft, conducted computational modeling, and analyzed data. Dr. Sayed Youssef Sayed and Brian C. Olsen helped with figure preparation. Dr. Erik J. Lubner helped with mathematical derivations. Shubham M. Shirurkar, Sankaranarayanan Venkatakrishnan and Prof. Eugene S. Smotkin from the Department of Chemistry and Chemical Biology, Northeastern University conducted the simulations on discharge polarization and corresponding power curves for RFBs. Dr. Ushula M. Tefashe, Dr. Anna K. Farquhar, and Prof. Richard L. McCreery contributed to the manuscript writing. Prof. Jillian M. Buriak was the supervisor and assisted with figure preparation and manuscript writing. All the authors contributed to discussion and final manuscript editing.

The work presented in Chapter 3 is based on the publication: Wang, H.; Sayed, S. Y.; Zhou, Y.; Olsen, B. C.; Lubner, E. J.; Buriak, J. M., Water-soluble pH-switchable cobalt complexes for aqueous symmetric redox flow batteries. *Chem. Commun.* 2020, 56 (25), 3605-3608. I designed the experiment, synthesized the compounds, conducted

experiment, analyzed data, as well as prepared figures and manuscript. Dr. Sayed Youssef Sayed helped set up the battery testing system. Dr. Yuqiao Zhou helped with acquiring crystallographic data. Brian C. Olsen helped with flow battery design and fabrication and drew the table of contents and cover figures. Dr. Erik J. Luber helped with manuscript revision. Prof. Jillian M. Buriak was the supervisor and assisted with manuscript writing. All the authors contributed to discussion and final manuscript editing.

Chapter 4 as written as a manuscript for submission. I designed the research plan, synthesized the compounds, conducted experiments, analyzed research data, as well as prepared figures that took place both before and after pandemic shutdown. Dr. Sayed Youssef Sayed assisted with assembly and testing of the full RFBs. Prof. Jillian M. Buriak was the supervisor and assisted in writing the manuscript.

Chapter 5 is the thesis summary and outlook for several future research directions in the field.

Acknowledgment

Firstly, I would like to express my deepest gratitude to my supervisor, Professor Dr. Jillian Buriak, for her continuous support, guidance, and encouragement. As a pioneer to conduct research on RFBs in the group, I could not have overcome the challenges successfully and built up the redox flow battery facilities and systems without her support and encouragement. Her knowledge, passion, and attitude towards science has influenced me a lot. For me, she is not only a respectful supervisor but also a great mentor and close friend. Your help and encouragement helped me go through a hard time during the pandemic and is still vivid in my mind. I am very grateful to have joined the Buriak group and be one of her students.

I would like to thank my committee members: Dr. Steven Bergens, Dr. Julianne Gibbs, Dr. Richard McCreery, and Dr. Jingli Luo from the Department of Chemical and Materials Engineering for their valuable advice and guidance. Thanks to my examination committee members, Dr. Richard L. McCreery and Dr. Jingli Luo for your thoughtful examination and suggestions. In addition, I would thank Dr. Roland Roesler from University of Calgary for agreeing to be my external examiner. Thanks to Dr. Mark T. McDermott for chairing my candidacy examination, respectively. I also would like to thank collaborators for their kindly help and support to my projects, including Dr. Yuqian Zhou, Dr. Ushula Tefashe, Dr. Anna Farquhar, Dr. Richard McCreery, as well as Shubham Shirurkar, Sankaranarayanan, Venkatakrisnan, and Dr. Eugene Smotkin from the Department of Chemistry and Chemical Biology, Northeastern University.

I would like to express my sincere gratitude to previous and current members from the Buriak group. Thanks to Dr. Sayed Youssef Sayed for your tremendous help with my research and papers writing. Brian Olsen and Tate Hauger, thank you for your generous technical support in my battery design, fabrication, and trouble shooting. Again, Brian Olsen and Dr. Erik Lubber, thank you for offering help with figure drawing and manuscript revision. Thanks as well to Dr. Hezhen Xie, Dr. Chengcheng Rao, Dr. Bing Cao, Dr. Cong Jin, Dr. Minjia Hu, Dr. Peter Kalisvaart, Dr. Christopher Fetterly,

Kelli Luber, Jennifer Ozdoba, Adrian Velazquez, Jasper Woodard, Dr. Mahmoud Almadhoun, Aaron Kirkey, and Gayashani Ginige for providing some useful suggestions for my research, along with a rich and colorful experience during my Ph.D. studies.

I also would like to thank the following staff of the Department of Chemistry, nanoFAB, and Nanotechnology Research Centre: Dieter Starke, Vincent Bizon, Wayne Moffat, Mark Miskolzie, Jason Dibbs, Andrew Yeung, Dr. Shihong Xu, and Dr. Michael Fleischauer for the technical support and kind help. Also, A special thank you to Dr. Anna Jordan for her patience and expertise in editing my thesis. I am also truly grateful for the scholarship support from University of Alberta and Alberta Innovates.

At last, I would like to thank my parents and grandparents for their unconditional love and support through my life. A special thanks is reserved for my love, Yangzhe Cao. I couldn't have gotten so far without you.

Table of Contents

Abstract	ii
Preface	iv
Acknowledgment	vi
Table of Contents	viii
List of Tables	xi
List of Figures	xii
List of Abbreviations	xxiii
Chapter 1 Introduction	1
1.1 Why Redox Flow Batteries?	1
1.1.1 Current Status of Intermittent Renewable Energy Storage.....	1
1.1.2 Advantages of Redox Flow Batteries	2
1.2 Basic Principles and Types of Redox Flow Batteries	3
1.2.1 Working Principles of Redox Flow Batteries	3
1.2.2 Performance Parameters for Redox Flow Batteries.....	4
1.2.3 Aqueous and Non-aqueous Redox Flow Batteries	6
1.2.4 Materials for Redox-active Materials, Electrodes, and Membranes.....	7
1.2.4.1 Materials for Redox-active Electrolytes, Electrodes, and Membranes in Aqueous RFBs	8
1.3 Evaluation Criteria for Redox-active Electrolytes in Aqueous Redox Flow Batteries	13
1.3.1 Physicochemical Properties of Redox-active Molecules.....	13
1.3.2 Electrochemical Characterization of Redox-active Molecules.....	14
1.3.2.1 Ex-situ Electrochemical Characterization of Redox-active Molecules	15
1.3.2.2 In-situ Electrochemical Characterization of Redox-active Molecules	17
1.4 Principle of Molecular Engineering of Redox-active Molecules	21
1.5 Scope of the Thesis	28
Chapter 2 Determining Electrochemical Kinetic Parameters in Redox Flow Batteries[†]	30

2.1 Introduction	30
2.2 Determination of Reversibility and Basic Kinetic Information of a New Redox System	31
2.2.1 Determination of Reversibility	31
2.2.2 Determination of the Diffusion Coefficient.....	37
2.2.3 Determination of Standard Rate Constant (k^0) Using Cyclic Voltammetry	40
2.3 Determining the Standard Rate Constant (k) Using a Rotating Disk Electrode	43
2.4 Conclusions	54
Chapter 3 Water-soluble pH-switchable Cobalt Complexes for Aqueous Symmetric Redox Flow Batteries[†]	55
3.1 Introduction	55
3.2 Results and Discussion	57
3.3 Conclusions	72
3.4 Experimental Section	73
3.4.1 Determination of Kinetic Parameters.....	76
3.4.2 Crystallographic Data for BCPIP-Co.....	77
Chapter 4 Molecular Engineering of a Biomimetic Phenazine-based Anolyte for Neutral Aqueous Redox Flow Batteries	80
4.1 Introduction	80
4.2 Results and Discussion	81
4.3 Experimental Section	89
Chapter 5 Thesis Summary and Outlook	95
5.1 Thesis Summary	95
5.1.1 Chapter 1	95
5.1.2 Chapter 2	95
5.1.3 Chapter 3	96
5.1.4 Chapter 4.....	96
5.2 Future work	97

5.2.1 Evaluation of Phenazine-based Anolyte for Redox Flow Batteries: Impact of Function Group Structure on Solubility and Electrochemistry	97
5.2.2 Stability and Mechanism of Capacity Decay of Phenazine-based Aqueous Flow Batteries.....	98
5.2.3 Air Stable Aqueous Redox Flow Batteries	98
5.2.4 All Phenazine Non-aqueous Redox Flow Battery	100
5.2.5 Investigate structure of BCPIP-Co(I) and possible absorption mechanism to develop symmetric ARFBs with high capacity	100
References	102

List of Tables

Table 1.1. Rank of Functional Groups by Polarity	23
Table 2.1. List of Commonly Used Symbols ^o	39
Table 2.2. Variation of ΔE_p with ψ at 25 °C for a One-Step and One-Electron Reaction, $\alpha = 0.5$, and Reverse Potential Greater than the Peak Potential by $112.5/n^o$	43
Table 2.3. Simulated Parameters for Irreversible and Quasireversible Systems in Figure 2.6a and 2.6d.....	45
Table 2.4. Inverse Currents $1/i$ for Angular Velocities, ω (rpm) and Potentials (V) as Indicated Used to Construct the Koutecký–Levich Plot for an Irreversible System in Figure 2.6b	46
Table 2.5. Characteristics for the Current–potential Wave Observed in Sampled Current Voltammetry Plots of E Versus $\text{Log}(i_d - i)/i$ at 25 °C. *Using Ultramicroelectrodes (UME), Electrodes of Radii Less Than 25 μm . This Table was Adapted from the Textbook of A. J. Bard. ^[114]	53
Table 3.1. Solubility of BCPIP-Co(II) Complex at Different pH Values, Corresponding to the Subsequent Neutralization of the Four Carboxylic Groups	62
Table 3.2. Crystallographic Experimental Details	79
Table 4.1. Solubility of Different Phenazine Derivatives at Nearly Neutral Solution	85
Table 4.2. Overview of Phenazine Derivatives as Anolyte for Aqueous Organic RFB	88

List of Figures

Figure 1.1. Comparison of system power and discharge time of different electrical energy storage systems. Reprinted with permission from reference 8, Copyright (2018), with permission from Elsevier.	2
Figure 1.2. (a) Schematic diagram of a redox flow battery for electrochemical energy storage. Reprinted with permission from reference 10. Copyright (2020) American Chemical Society. (b) The flow cell compartments: 1-endplate, 2-electron collectors, 3-graphite plates with flow channels, 4-gaskets, 5-electrodes (usually carbon paper or carbon felt), 6-membrane. Reproduced from reference 11. Copyright 2018 Royal Society of Chemistry.....	3
Figure 1.3. Considerations for the development of flow batteries. Reprinted with permission from reference 31. Copyright © 2016 Rights Managed by Springer Nature.	8
Figure 1.4. Distribution of costs for 4 MWh all vanadium RFB. Reprinted with permission from reference 49. Copyright (2014) Elsevier.	9
Figure 1.5 Chemical structure and cyclic voltammograms (CV) of BTMAP-Vi and BTMAP-Fc. Condition for CV: 1.0 mM in 0.5 M NaCl (aq) at a scan rate of 10 mV s ⁻¹ . Reprinted with permission from reference 58. Copyright (2017) American Chemical Society.....	10
Figure 1.6. Schematic representation of a typical cyclic voltammetry setup with a counter electrode (CE) a working electrode (WE), and a reference electrode (RE). Reprinted with permission from reference 106. Copyright © 2017 Rights Managed by Springer Nature.	16

Figure 1.7. Schematic representation of a typical rotating disk electrode cell setup. Reprinted with permission from reference 107 with permission from IOP Publishing.	17
Figure 1.8. Polarization curve for a redox flow battery device. Reprinted with permission from reference 10. Copyright (2020) American Chemical Society.	18
Figure 1.9. Equivalent circuit for typical redox flow battery. Reprinted with permission from reference 107 with permission from IOP Publishing.	20
Figure 1.10. Experimental redox potential of various quinones at three different pH values. Reprinted with permission from reference 128 with permission from Springer Nature.	24
Figure 1.11. Macromolecular design strategies for size excursion effect: (a) small size of electroactive organic molecules crossover the membrane; (b) and (c) larger size of oligomers are blocked from the microporous membrane. Reprinted with permission from reference 119. Copyright (2017) John Wiley and Sons.	25
Figure 1.12. Down-selection of candidates for energy storage molecules based on quantum chemical calculations. Reprinted with permission from reference 50. Copyright (2015) American Chemical Society.	27
Figure 2.1. A simulated cyclic voltammogram for a reversible system showing the exact determination of peak current from the base line. This plot is expected with low background current (without redox species present), or after subtraction of the background current. Reprinted with permission from reference 10. Copyright (2020) American Chemical Society.	33

Figure 2.2. First set of cyclic voltammetry (CV) experiments to define the kinetic regimes (reversible, quasireversible, and irreversible) for an electron transfer (ET) mechanism (steps 1–3a). CVs for reversible, quasireversible, and irreversible systems were simulated using Bio-Logic EC-Lab software. Parameters: $k^0 = 0.5 \text{ cm s}^{-1}$ (reversible, red), 0.001 cm s^{-1} (quasireversible, blue), and $1 \times 10^{-6} \text{ cm s}^{-1}$ (irreversible, green); $v = 50 \text{ mV s}^{-1}$; diffusion coefficient ($D_0 = D_R = 1 \times 10^{-5}$). *The final potential range for the quasireversible system in step 2 [(200/n) mV] was chosen based on values obtained from the Nicholson equation, Table 2.2. Step 3b illustrates the representative linear relationship between the peak currents and the square root of scan rates $v^{1/2}$ for reversible and irreversible systems. Refer to Table 2.1 for a more detailed description of the symbols used in this figure. Reprinted with permission from reference 10. Copyright (2020) American Chemical Society..... 36

Figure 2.3. (a) Linear sweep voltammograms at different angular velocity. (b) Levich plot. Solving for D provides the diffusion coefficient for a quasireversible system (as well as reversible and irreversible systems). Reprinted with permission from reference 10. Copyright (2020) American Chemical Society..... 39

Figure 2.4. (a) Cyclic voltammetry for an irreversible system at different scan rates. (b,c) Plots for $\ln(i_p)$ versus $(E_p - E^{0'})$ for both cathodic and anodic peaks, provided that $E^{0'}$ is known for the studied system. Reprinted with permission from reference 10. Copyright (2020) American Chemical Society..... 41

Figure 2.5. Example of the plot of ψ , determined by the peak separations (Table 2.2 or eq 2.5) of cyclic voltammograms observed at different scan rates versus the square root of the scan rates for quasireversible systems. Reprinted with permission from reference 10. Copyright (2020) American Chemical Society..... 42

Figure 2.6. Simulated rotating disk electrode (RDE) scans at different rotation rates for irreversible (a) and quasireversible (d) systems. Koutecký–Levich plots for irreversible

(b) and quasireversible (e) systems. (c) Plot of $\log(i_k)$ vs $E - E^0$ for the irreversible system. (f) Change of the slopes with overpotentials for the $i^{-1} - \omega^{-1/2}$ plots in (b, e). Simulated parameters for irreversible and quasireversible systems are listed in Table 2.3. Reprinted with permission from reference 10. Copyright (2020) American Chemical Society. 44

Figure 2.7. Plot the slope of the $i - 1$ vs. $\omega - 1/2$ plots for quasireversible system (Figure 2.6e) vs. $eFRT(E - E^0)$. Reprinted with permission from reference 10. Copyright (2020) American Chemical Society..... 49

Figure 2.8. Sampled current voltammetry procedures. (a) Potential step experiments at different increasing reducing potentials. (b) Current–time decay for each of the applied potential steps and illustrates the sampling time (same for all potential steps). (c) Sampled current voltammogram. Reprinted with permission from reference 10. Copyright (2020) American Chemical Society..... 50

Figure 2.9. Examples of sampled current voltammetry for the three different kinetics regimes. Reprinted with permission from reference 10. Copyright (2020) American Chemical Society. 51

Figure 2.10. (a) A discharging polarization curve for a redox flow battery (RFB) device, illustrating three voltage regions that are associated with kinetics, ohmic, and mass-transfer losses. (b) Simulated discharge polarization and corresponding power curves at 50% state of charge (equal concentrations for the O and R species) for three RFBs of different combinations of reversible and quasireversible redox systems with k^0 of $3 \times 10^{-1} \text{ cm s}^{-1}$ and $2 \times 10^{-4} \text{ cm s}^{-1}$, respectively. Reprinted with permission from reference 10. Copyright (2020) American Chemical Society..... 53

Figure 3.1. (a) Fully protonated BCPIP-Co(II) complex. (b) Thermal ellipsoid plot of BCPIP-Co(II) chloride, obtained from single-crystal X-ray diffraction. Cobalt is shown

in yellow, carbon in gray, nitrogen in blue, oxygen in red, and chloride in green. Atoms are represented by ellipsoids at the 50% probability level, and hydrogen atoms and solvent have been omitted for clarity. (c) CV curves of 2 mM BCPIP-Co in 0.5 M NaCl at pH 3.0 acquired at a scan rate of 50 mV/s. Reproduced from reference 61. Copyright (2020) Royal Society of Chemistry. 57

Figure 3.2. (a) ^1H NMR spectrum of the ligand, BCPIP (DMSO- d_6 , 27 °C). (b) ^{13}C NMR spectrum of the ligand, BCPIP (DMSO- d_6 , 27 °C). (c) Transmission mode FTIR spectra of BCPIP-Co(II) on a native oxide-capped silicon wafer. Features at 1600 and 1575 cm^{-1} correspond to pyridyl and aryl-ring breathing mode deformations. (d) UV spectra of BCPIP-Co(II) at different pH values (0.02 mM) using NaOH (aq) to adjust pH. Reproduced from reference 61. Copyright (2020) Royal Society of Chemistry. 58

Figure 3.3. CV for the Co(II)/Co(III) (a) and Co(I)/Co(II) (b) redox reactions as a function of pH in 2 mM of BCPIP-Co(II) and 0.5 M NaCl (aq) at 50 mV/s. (c) Average redox peak potentials, $E_{1/2}$, of BCPIP-Co redox pairs vs pH. $E_{1/2} = (\text{anodic peak potential} + \text{cathodic peak potential})/2$. Reproduced from reference 61. Copyright (2020) Royal Society of Chemistry. 59

Figure 3.4. CV of 1 mM of BCPIP-Co(II) on a glassy carbon electrode in 0.5 M NaCl (aq) at pH 3.0, after increasing the pH to 5.5, and then lowering it back to pH 3.0. (a) Cathodic event [Co(II/I)] for the BCPIP-Co(II) redox reactions. (b) Anodic event [Co(II/III)] for the BCPIP-Co(II) redox reactions. Reproduced from reference 61. Copyright (2020) Royal Society of Chemistry. (See experimental details in the Experimental Section, Reversibility.) 60

Figure 3.5. Speciation of different BCPIP-Co(n) species in their sequential deprotonated forms, where $n = \text{I, II, or III}$, spanning the pH range of 1.5 to 5.5 (Highlights of -COOH groups: orange = protonated; blue = deprotonated). Reproduced from reference 61. Copyright (2020) Royal Society of Chemistry. 61

Figure 3.6. (a) CV curves of 2 mM BCPIP-Co(II-III) at pH 3.0 at various scan rates from 0.025 V/s to 1.0 V/s in 0.5 M NaCl (aq). (b) CV curves of 2 mM BCPIP-Co(II-I) at pH 3.0 at various scan rates from 0.025 V/s to 1.0 V/s in 0.5 M NaCl (aq). The potential axes were corrected for the uncompensated ohmic resistance. Reproduced from reference 61. Copyright (2020) Royal Society of Chemistry. 63

Figure 3.7. (a) Reductive and oxidative peak potential change with the square root of scan rate $v^{1/2}$ for the corresponding CV curves of BCPIP-Co(II), Co(II/III) redox couple, at pH 3.0. (b) Nicholson's analysis for examination of heterogeneous electron-transfer rate constant k^0 : plot of the dimensionless kinetic parameter (ψ) vs square root of scan rate (v). Reproduced from reference 61. Copyright (2020) Royal Society of Chemistry. 63

Figure 3.8. (a) Linear sweep voltammograms for the Co(II)/Co(III) redox reactions of the 2.0 mM BCPIP-Co(II) at different rotation speeds of the RDE in 0.5 M NaCl at a nominal pH of 3.0. (b) Limiting currents vs the square root of rotation rate (Levich plots) for BCPIP-Co(II); (c) Koutecký–Levich plot (i^{-1} vs $\omega^{-1/2}$) of BCPIP-Co(II). (d) Plot of the overpotential vs $\log_{10}(i_k)$. The overpotential is defined as $E_{\text{meas}} - E^0$. Reproduced from reference 61. Copyright (2020) Royal Society of Chemistry. 64

Figure 3.9. (a) Linear sweep voltammograms of 2.0 mM BCPIP-Co(II), Co(II/I) redox couple, in 0.5 M NaCl (aq) at pH 3.0 under various rotation speeds. Due to the weak interaction between the BCPIP-Co(I) complex with the electrode surface, a peak at ca. -0.3 V vs NHE and seemingly coincident plots are observed in the current–potential region typically used for the mass transfer correction and extraction of kinetic information, thus, impeding further kinetic analysis for the redox reaction [Co(II)/Co(I)] using RDE. (b) Cyclic Voltammograms of 1 mM BCPIP-Co(II), Co(II/I) redox couple, at various scan rates from 0.025 V/s to 1.0 V/s in 0.5 M NaCl (aq) at pH 5.0. Reproduced from reference 61. Copyright (2020) Royal Society of Chemistry. 65

Figure 3.10. (a) Schematic and (b) optical image of the lab-designed flow battery system.	66
Figure 3.11. (a) SEM of pristine carbon paper as received from Sigracet 29 AA. (b) SEM of O ₂ -plasma-pretreated carbon paper. After O ₂ plasma, the carbon fibers have fewer scattered particles and show negligible morphological changes of the carbon fibers themselves. Water wetting properties of carbon paper (c) before oxygen plasma (d) after oxygen plasma treatment. Reproduced from reference 61. Copyright (2020) Royal Society of Chemistry.	66
Figure 3.12. CV curves as a function of cycle number for 1 mM BCPIP(II), Co(II/III) redox couple, in 0.5 M NaCl (aq) at a rate of 100 mV/s for different pH levels. (a) pH 3.0, (b) pH 3.5, (c) pH 4.5, and (d) pH 5.0. The number of cycles is shown as an inset in each panel. Reproduced from reference 61. Copyright (2020) Royal Society of Chemistry.	67
Figure 3.13. CV curves as a function of cycle number for 1 mM BCPIP(II), [Co(II/I)] redox couple, in 0.5 M NaCl (aq) at a rate of 100 mV/s for different pH levels. (a) pH 3.0, (b) pH 3.5, (c) pH 4.5, and (d) pH 5.0. The number of cycles is shown in the inset in each panel. Reproduced from reference 61. Copyright (2020) Royal Society of Chemistry.	67
Figure 3.14. Analyses of peak currents and areas from Figure 3.12. (a) The absolute values of the peak currents for the anodic (solid lines) and cathodic (dashed lines) sweeps of the 1 mM catholyte CV per cycle. (b) The normalized area is given as a percentage of the area between the anodic and cathodic sweeps of the 1 mM catholyte CV per cycle. Reproduced from reference 61. Copyright (2020) Royal Society of Chemistry.	68

Figure 3.15. (a) Charge–discharge profile of the 10 mM BCPIP-Co(II) symmetric flow battery at pH 3.5. Reproduced from reference 61. Copyright (2020) Royal Society of Chemistry..... 69

Figure 3.16. (a) Charge–discharge profile of the symmetric BCPIP-Co(II) RFB at 2 mA/cm² with 1 mM of BCPIP-Co(II) as catholyte and anolyte at a pH of 3.5. The specific capacity was calculated based on the mass of BCPIP-Co(II). (b) Cycling stability and coulombic efficiency of the symmetric BCPIP-Co(II) flow battery at 2 mA/cm² with 1 mM and 10 mM of BCPIP-Co(II) as catholyte and anolyte. Reproduced from reference 61. Copyright (2020) Royal Society of Chemistry. 69

Figure 3.17. (a) EDX of gold-coated fumasep FAS-30 membrane from the 10 mM BCPIP-Co(II) symmetric cell at pH 3.5 after 100 cycles. (b) EDX of gold-coated Nafion 212 membrane from the 10 mM BCPIP-Co(II) symmetric cell at pH 3.5 after 100 cycles. Reproduced from reference 61. Copyright (2020) Royal Society of Chemistry..... 70

Figure 3.18. Photographs: (a) Membrane from the 1 mM BCPIP-Co(II) symmetric cell at pH 3.5 after 100 cycles; (b) fumasep FAS-30 membrane from the 10 mM BCPIP-Co(II) symmetric cell at pH 3.5 after 100 cycles.(c) Nafion 212 membrane from the 10 mM BCPIP-Co(II) symmetric cell at pH 3.5 after 100 cycles. (In the case of 10 mM BCPIP-Co(II) symmetric cell, upon pumping water into the cell, one would expect to observe colourless solutions at the outlets of both the catholyte and anolyte compartments. However, upon rinsing the cell, a colorless solution emerged from the catholyte side, but a red solution was observed to come out of the anolyte compartment, most likely due to adsorption of anolyte on the membrane.) Reproduced from reference 61. Copyright (2020) Royal Society of Chemistry. 70

Figure 3.19. (a) Carbon papers removed from both catholyte and anolyte sides from the 10 mM BCPIP-Co(II) symmetric cell at pH 3.5 after 100 cycles, after soaking in

ultrapure 18 M Ω cm water overnight. (b) The catholyte and anolyte solutions diluted 15x with ultrapure 18 M Ω cm water, from the 10 mM BCPIP-Co(II) symmetric cell at pH 3.5 after 100 cycles. Reproduced from reference 61. Copyright (2020) Royal Society of Chemistry..... 71

Figure 3.20. CV cycling of 1 mM of BCPIP-Co(II) in 0.5 M NaCl (aq) at pH 3.5 over an extended voltage window from 0.3 to 1.5 V vs NHE. Reproduced from reference 61. Copyright (2020) Royal Society of Chemistry. 72

Figure 3.21. (a)UV-vis spectra of BCPIP-Co(II) at different concentrations. The solutions were prepared by using ultrapure 18 M Ω cm water, and the pH was not controlled (the ‘native’ pH). (b) Absorbance at 338 nm as a function of concentration. The solutions were prepared by using ultrapure 18 M Ω cm water, and the pH was not controlled (‘native’ pH). Reproduced from reference 61. Copyright (2020) Royal Society of Chemistry..... 75

Figure 3.22. Perspective view of the whole contents of 2,6-Bis[1-(4-carboxyphenylimino)ethyl] pyridine cobalt(II) chloride, 2,6-Bis[1-(4-carboxyphenylimino)ethyl] pyridine cobalt(II) chloride acetonitrile solvate, showing the atom labelling scheme. Non-hydrogen atoms are represented by Gaussian ellipsoids at the 30% probability level. Hydrogen atoms are shown with arbitrarily small thermal parameters. Reproduced from reference 61. Copyright (2020) Royal Society of Chemistry..... 78

Figure 4.1. (a)Phenazine two-electron electrochemical redox reaction. (b) The molecular structures of the synthesized phenazine derivatives. 80

Figure 4.2. (a) ¹H NMR spectrum of the HP (DMSO-d₆, 27 °C). (b) ¹³C NMR spectrum of the HP (DMSO-d₆, 27 °C). (See details about peak assignments in the Experimental Section) 82

Figure 4.3. (a) ^1H NMR spectrum of the PPSNa (DMSO- d_6 , 27 °C). (b) ^{13}C NMR spectrum of the PPSNa (DMSO- d_6 , 27 °C). (See details about peak assignments in the Experimental Section).....	82
Figure 4.4. (a) ^1H NMR spectrum of the DHP (DMSO- d_6 , 27 °C). (b) ^{13}C NMR spectrum of the DHP.....	82
Figure 4.5. (a) ^1H NMR spectrum of the 2,3-DPPSNa ₂ (D ₂ O, 27 °C). (b) ^{13}C NMR spectrum of the 2,3-DPPSNa ₂ (D ₂ O, 27 °C). (See details about peak assignments in the Experimental Section).....	83
Figure 4.6. (a) ^1H NMR spectrum of the DHPS (DMSO- d_6 , 27 °C). (b) ^{13}C NMR spectrum of the DHPS (DMSO- d_6 , 27 °C). (See details about peak assignments in the Experimental Section).....	83
Figure 4.7. (a) ^1H NMR spectrum of the 2,3-SPDPSNa ₃ (D ₂ O, 27 °C). (b) ^{13}C NMR spectrum of the 2,3-SPDPSNa ₃ (D ₂ O, 27 °C). (See details about peak assignments in the Experimental Section).....	83
Figure 4.8. (a) The molecular structures of the synthesized phenazine derivatives. (b) CV curves of 2 mM HP, DHP, DHPS, PPSNa, 2,3-DPPSNa ₂ , and 2,3-SPDPSNa ₃ in 0.5 M NaCl (aq) at pH 7 acquired at a scan rate of 50 mV s ⁻¹ . HP and DHP were measured in a saturated solution at pH 7.	84
Figure 4.9. (a) Cyclic voltammograms of 2 mM PPSNa as a function of pH in 0.5 M NaCl (aq) at 50 mV s ⁻¹ . (b) Pourbaix diagram of PPSNa in 0.5 M NaCl (aq).....	86
Figure 4.10. (a) Linear sweep voltammograms of 2 mM PPSNa in 0.5 M NaCl (aq); (b) Levich plots of the limiting current vs the square root of rotation rates for PPSNa.	86

Figure 4.11. (a) Charge–discharge profile of the 0.1M PPSNa K ₄ Fe(CN) ₆ ARFB in 1 M KCl (aq) at pH 7 at a current density of 20 mA cm ⁻² . (b) Cycling stability and Coulombic efficiency of 0.1 M PPSNa K ₄ Fe(CN) ₆ ARFB in 1 M KCl (aq) at pH 7 at a current density of 20 mA cm ⁻²	87
Figure 4.12. (a) UV-vis spectra of DHPS in buffer solution (pH 7) at different concentrations. (b) Absorbance at 404 nm as a function of concentration.	92
Figure 4.13. (a) UV-vis spectra of PPSNa in water at different concentrations (pH 7). (b) Absorbance at 367 nm as a function of concentration.	92
Figure 4.14. (a) UV-vis spectra of 2,3-DPPSNa ₂ in water at different concentrations (pH 7). (b) Absorbance at 393 nm as a function of concentration.....	93
Figure 4.15. (a) UV-vis spectra of 2,3-SPDPSNa ₃ in water at different concentrations (pH is 7). (b) Absorbance at 397 nm as a function of concentration.	93
Figure 5.1. Molecular structure of phenazine derivatives.....	98
Figure 5.2. Linear sweep voltammograms of 0.132 mM of (2) 2,3,5,6-tetramethylpyrazine, (3) 2,3-dimethylquinoxaline, (4) 2,3-diphenyl -quinoxaline, (5) 0.132 mM phenazine at 1600 rpm of RDE in 0.08 M NaClO ₄ and HClO ₄ DMF [20% (v/v)]-water solutions. (---) and (-) represent N ₂ and air-saturated solution, respectively. Reprinted with permission from 214. Copyright (2004) American Chemical Society.	99
Figure 5.3. Redox potential (vs Fc/Fc ⁺) of phenazine functionalized with different number of cyano groups (green) and amino groups (blue). For reproduction of material from all other RSC journals:	100

List of Abbreviations

AC	Alternating current
ARFB	Aqueous Redox Flow Battery
BTMAP-Fc	Bis((3-trimethylammonio)propyl)ferrocene Dichloride
BTMAP-Vi	Bis(3-trimethylammonio)propyl Viologen Tetrachloride
BCPIP-Co	2,6-Bis[1-(4-carboxyphenylimino)ethyl]pyridine cobalt chloride
CE	Coulombic Efficiency
CE	Counter Electrode
CV	Cyclic Voltammetry
CPE	Constant Phase Element
CCDC	Cambridge Crystallographic Data Centre
DHAQ	Dihydroxyanthraquinone
DFT	Density Functional Theory
DMSO	Dimethyl Sulfoxide
EIA	Energy Information Administration
EE	Energy Efficiency
EIS	Electrochemical Impedance Spectroscopy
ET	Electron Transfer
E_p	Peak Potential
EDX	Energy Dispersive X-ray Analysis
ESI-MS	Electrospray Ionization Mass Spectrometry
FTIR	Fourier-transform Infrared Spectroscopy
HOMO	Highest Occupied Molecular Orbital
HER	Hydrogen Evolution Reaction
HPLC	High Performance Liquid Chromatography
LC-MS	Liquid Chromatography–mass Spectrometry
i_f	Faradic Current
i_c	Double Layer Charging Current
i_{pa}	Anodic Peak Current

i_{pc}	Cathodic Peak Current
i_l	Limiting Current
i_k	Kinetic Current
k^0	Heterogeneous Electron Transfer Rate Constant
LUMO	Lowest Unoccupied Molecular Orbital
LSV	Linear sweep Voltammetry
MV	Methyl Viologen Dichloride
NASA	National Aeronautics and Space Administration
NHE	Standard Hydrogen Electrode
NMR	Nuclear Magnetic Resonance
OER	Oxygen Evolution Reaction
PTFE	Polytetrafluoroethylene
PEEK	Polyether ether ketone
POMs	Polyoxometalates
PEG	Polyethylene Glycol
RFB	Redox Flow Battery
RE	Reference Electrode
RDE	Rotating Disk Electrode
R_{ct}	Charge Transfer Resistance
SEM	Scanning Electron Microscopy
SCV	Sampled Current Voltammetry
SHE	Standard Hydrogen Electrode
SOC	State of Charge
TEOA	Triethanolamine
TEMPO	2,2,6,6-Tetramethyl-1-piperidinyloxy
TKEN	Tetra-substituted Hydroxyl Alkyl Ammonium
TKMP	Tetra-substituted Hydroxyl Alkyl Phosphonium
UME	Ultramicroelectrode
Uv-Vis-Nir	Ultraviolet-Visible-near-Infrared
VE	Voltage Efficiency

VRFB	Vanadium Redox Flow Battery
WE	Working Electrode
Z_w	Warburg Element

Chapter 1

Introduction

1.1 Why Redox Flow Batteries?

1.1.1 Current Status of Intermittent Renewable Energy Storage

Electricity is an indispensable energy source that powers both worldwide economic growth and stability. The U.S. Energy Information Administration (EIA) projects that world energy consumption will increase by 50% between 2018 and 2050.^[1] The integration of renewable sources, such as hydroelectricity, solar, wind, and geothermal power are necessary to address increasing energy demands, as well as the concomitant reduction of carbon emissions.^[2] Due to geographical limitations and ecological impact from geothermal energy and hydroelectricity, wind and solar energy are promising alternatives, as they can be deployed just about anywhere on the globe, including remote locations.^[3] Electricity from both wind and solar energy are the least expensive sources of electricity on the planet and, as a result, are expected to account for over 70% of the total renewable energy production globally (as much as 6.7 trillion and 8.3 trillion kilowatt-hours in 2050, respectively) over the next decades.^[1] However, due to the intermittency and volatility of wind and solar energy, electrical-energy storage systems are needed to buffer deviations in energy production and consumption.

As shown in Figure 1.1, there are various energy storage technologies, such as pumped hydro, compressed air, flow batteries, Li-ion batteries, high-power flywheels, and supercapacitors.^[4] Compared with other energy storage technologies, flow batteries, pumped hydro, and compressed air store more energy and deliver with high power, which is good for large-scale energy storage systems. In spite of the low expense of pumped hydro and compressed air energy storage, they are restrained geographically.^[5, 6] Redox flow batteries (RFBs), based on rechargeable batteries technologies, have attracted a lot of attention in recent years.^[7]

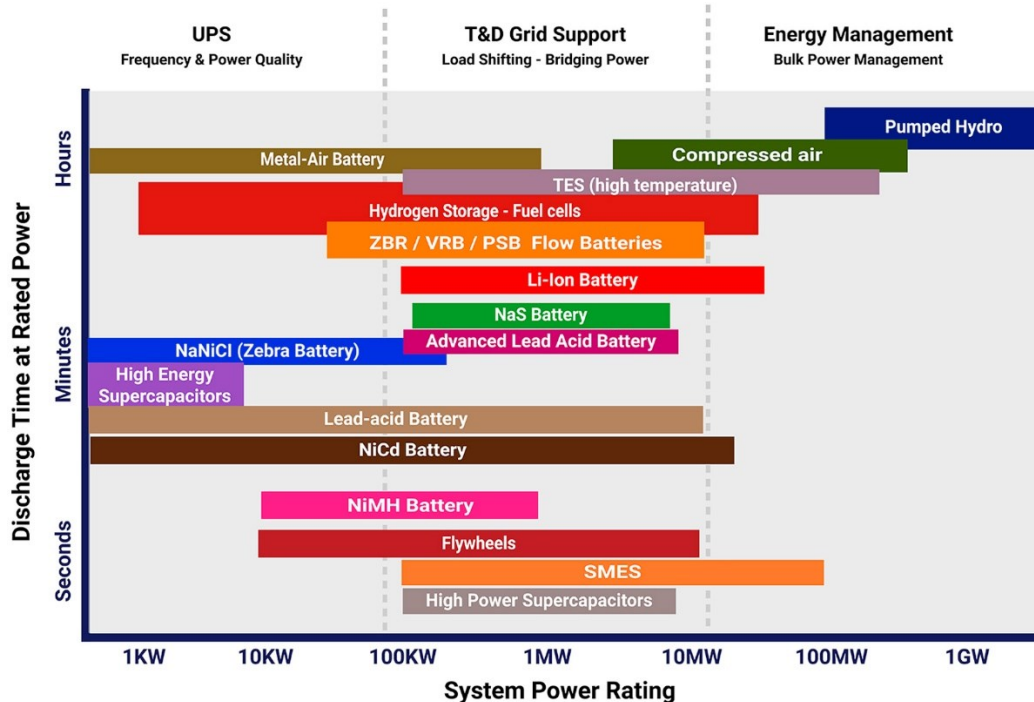


Figure 1.1 Comparison of system power and discharge time of different electrical energy storage systems. Reprinted with permission from reference 8, Copyright (2018), with permission from Elsevier.

1.1.2 Advantages of Redox Flow Batteries

In contrast to conventional rechargeable batteries, RFBs are an electrochemical energy storage device that stores energy using redox active molecules in electrolytes that are recirculated through the cell. In a flow cell, electrolytes are fed from external storage tanks to the cell compartments, where electrodes are separated by a membrane (Figure 1.2a), to generate power.

Similar to the setup of fuel cells, this setup enables the decoupling of power and energy density, where the power density is governed by the size of electrode and the energy density is regulated by the amount of redox active species stored in the tanks. The redox reaction in the RFB usually occurs on the electrode surface without damaging the internal structure, which makes it suitable for a long life cycle.^[6] Thanks to the technological merits of decoupling stored chemical energy and tunable power density, scalability, active thermal management, safety, and long lifetimes, RFBs have become good candidates for the next generation of energy storage systems.^[9]

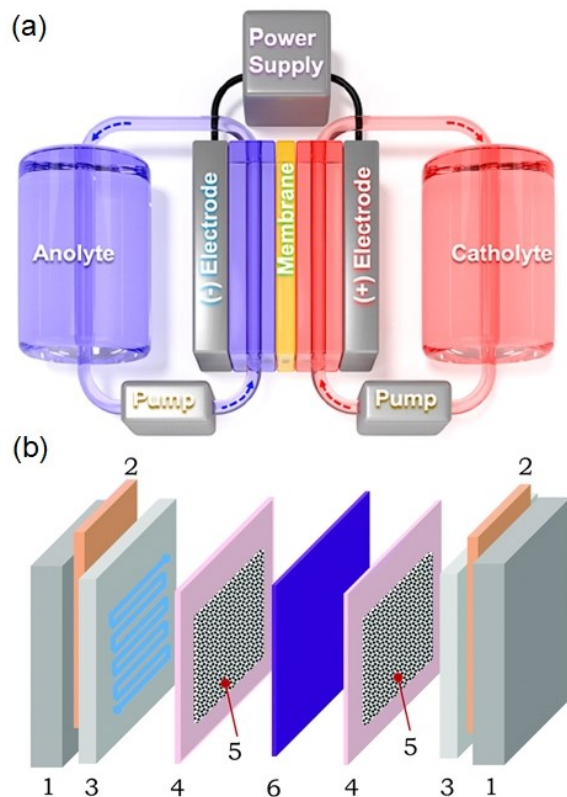


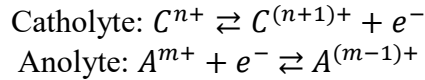
Figure 1.2. (a) Schematic diagram of a redox flow battery for electrochemical energy storage. Reprinted with permission from reference 10. Copyright (2020) American Chemical Society. (b) The flow cell compartments: 1-endplate, 2-electron collectors, 3-graphite plates with flow channels, 4-gaskets, 5-electrodes (usually carbon paper or carbon felt), 6-membrane. Reproduced from reference 11. Copyright 2018 Royal Society of Chemistry.

1.2 Basic Principles and Types of Redox Flow Batteries

1.2.1 Working Principles of Redox Flow Batteries

As shown in Figure 1.2a, a typical RFB contains two electrolyte reservoirs (tanks), two pumps, and an electrochemical cell. The membrane is permeable to the supporting salt but impermeable to the redox active molecules. The electrochemical cells consist of two electrolyte chambers that are separated by a membrane (Figure 1.2b). The membrane is permeable to the supporting salt but impermeable to the redox active molecules. In each electrolyte chamber, electrodes (carbon paper or carbon felt), connected with electron collector (bipolar graphite plate), are submerged in a redox-active contained electrolyte. The two electrically active solutions are called the catholyte (also called the catholyte) and the anolyte (also called the anolyte). During

the charging process, electrical energy is converted to chemical energy through reduction of the anolyte and oxidation of the catholyte in the electrochemical cell before they are circulated back to the tank. During the discharge process, the reduced anolyte and oxidized catholyte are pumped into the cell to be oxidized and reduced, respectively. A simple schematic outlining these one-electron reactions during charge and discharge is shown below:



1.2.2 Performance Parameters for Redox Flow Batteries

The performance of an RFB can be evaluated by several parameters. Voltage (V), as a basic but important parameter, stands for the driving force the battery can provide. The ideal voltage of an RFB is determined by the redox potential difference between the catholyte and anolyte. A higher voltage can be achieved by choosing a catholyte with a more positive potential and an anolyte with a more negative potential. In real applications, the output potential is affected by ohmic resistance (e.g., electrode resistance, solution resistance, contact resistance, membrane resistance), and electrochemical kinetic effects and mass-transfer effects (details about kinetics and mass transfer are described in detail in Chapter 2).

The theoretical volumetric capacity indicates the amount of charge stored in a given quantity of electrolyte in units of Ah/L (eq 1.1).

$$\text{Theoretical volumetric capacity: } C_{\text{ap}} = nCF \quad 1.1$$

where n is the number of electrons engaged in a redox reaction, C is the lower concentration of the redox-active species (nC stands for the electron concentration; the smaller one from either the catholyte or anolyte is used to decide the total capacity of an RFB) with units of mol/L, and F is the Faraday constant. Thus, the volumetric capacity is determined by the solubility and the number of electrons (or electron concentration) of the redox-active materials.

The energy density, including voltage, is another important parameter to evaluate the performance of an RFB. The theoretical energy density in units of Wh/L is calculated by eq 1.2.

$$\text{Energy density: } E(\text{Wh/L}) = C_{\text{ap}}V/\mu_v \quad 1.2$$

where C_{ap} is the smaller volumetric capacity either from the catholyte or anolyte, V is the cell voltage, and μ_v is the reduced volume factor, which is equal to the $1 + C_{ap}/C'_{ap}$, where C'_{ap} is the larger volumetric capacity of either the anolyte or catholyte. Then, the energy density is affected by cell voltage and volumetric capacity.

The current density (I), as an important parameter in RFBs, determines the total charging/discharging time and is related to the size of the membrane; the units are usually mA/cm². Thus, when incorporated with voltage, the power density, which provides information regarding the amount of power an RFB can supply per unit area, is obtained. The power density is calculated in units of mW/cm² using eq 1.3.

$$\text{Power density: } P = IV \quad 1.3$$

Thus, the power density is linked directly to the battery voltage. Factors such as the conductivities of the electrolytes, the membranes, and the electrodes, as well as the electrochemical kinetics of redox-active species that affect the cell voltage, can govern the change of power density. Other parameters, including the flow rate, the pattern of the flow channel, and the temperature also can influence the power density.^[11]

The Coulombic efficiency (CE) and voltage efficiency (VE) are two other critical indicators of electrical quality of an RFB. The CE is the ratio of the charge delivered in the discharging procedure to the charge applied in the charging procedure (eq 1.4). The VE is the ratio between the average discharging voltage and the average charging voltage (eq 1.5).

$$\text{Coulombic efficiency: } CE = \frac{Q_D}{Q_C} \quad 1.4$$

$$\text{Voltage efficiency: } VE = \frac{\frac{\int_0^{t_D} V_D(t) dt}{t_D}}{\frac{\int_0^{t_C} V_C dt}{t_C}} \quad 1.5$$

where Q , t , and V are the total charge, time and voltage, respectively. Subscripts C and D refer to the charging and discharging processes, respectively. CE stands for the charge efficiency and the reversibility of a battery, which can be affected by crossover of the redox-active materials and irreversible reactions that occur during the charge/discharge processes. VE implies the effect of overpotential of a battery system. The overpotential, including ohmic, activation, and mass-transfer overpotentials, are

related to VE in the RFB system. The energy efficiency (EE), calculated by multiplication of CE by VE , is the ratio of the energy released during the discharging process and the stored energy during the charging process.

The capacity retention also is taken into consideration when evaluating the performance of a battery system. The capacity utilization relates the practical capacity to the theoretical capacity. It indicates the capacity retention percentage per cycle or after a certain number of cycles. Recently, capacity retention based on a certain length of time has been chosen to show the stability of an RFB system.^[12, 13]

1.2.3 Aqueous and Non-aqueous Redox Flow Batteries

So far, various novel flow battery systems have been developed, including all-vanadium, all-iron, zinc-iron, zinc-bromine, and some organic or metal organic flow battery systems.^[14, 15] Based on the solvent used in the RFB, these systems can be divided into aqueous and non-aqueous systems, depending on whether the solvent is water or organic solvent.

The first concept of non-aqueous RFB was studied in 1984.^[16] Since then, different non-aqueous flow battery systems, based on diverse redox-active materials (e.g., ruthenium complexes,^[17] uranium β -diketonates,^[18] and vanadium acetylacetonate^[19]), have been proposed in different solvents, including propylene carbonate, acetonitrile, and dimethylformamide.^[20] Due to the large electrochemical window and wide working temperature range, a non-aqueous flow battery system potentially offers RFB a high energy density, even in a low-temperature environment.^[21] However, challenges such as flammable, high-viscosity, and low-conductive supporting salts, lack of good commercial membranes, and expensive and toxic electrolytes need to be overcome before it is of practical use.^[21, 22]

Compared to a non-aqueous flow battery system, the aqueous system has the advantages of (1) a well-developed aqueous based membrane (e.g. Nafion); (2) a non-flammable aqueous electrolyte, which provides a safety benefit; (3) inexpensive supporting salts, such as NaCl or NaOH that help to reduce the total cost and offer high conductivity for high-power RFBs.^[14, 23] The first RFB was patented by Kangro in 1949, and used a mixture of elements, including titanium, iron, chlorine and chromium.^[24]

National Aeronautics and Space Administration (NASA) then looked to RFBs to in the 1970s.^[25] They used a $\text{Cr}^{2+}/\text{Cr}^{3+}$ couple as the anolyte and a $\text{Fe}^{2+}/\text{Fe}^{3+}$ couple as the catholyte, which exhibited a voltage of 1.18 V in a aqueous halide solution. One shortcoming that has restricted the development of aqueous RFBs is the limited electrochemical window caused by the hydrogen and oxygen evolution reactions. The water splitting window can be extended somewhat higher than 2 V due to the high overpotential of oxygen and hydrogen evolution from the electrode surface.^[26] With respect to the operating range of temperature for an aqueous RFB, introducing cosolvents, antifreezing agents, or foreign solutes provides a possible way to decrease the freezing point,^[27-29] making aqueous RFBs a promising alternative to energy storage systems.

1.2.4 Materials for Redox-active Materials, Electrodes, and Membranes

RFBs are of great interest as electrochemical energy storage systems, particularly for stationary applications.^[30] As shown in Figure 1.2a, this type of battery architecture is based on redox-active pairs in separate solutions that are contained within external storage tanks, the anolyte (negolyte) and the catholyte (posolyte).^[2, 3, 31, 32] Power is generated upon flow of the anolyte and catholyte within a central electrochemical cell, comprising an ion exchange membrane with one electrode on each side. The main components for an RFB are redox-active material, electrode, and membrane.

The critical requirement for the development of flow batteries are summarized in Figure 1.3. The properties of the catholyte, anolyte, electrode, and membrane determine the performance of the flow batteries, including volumetric energy density, areal power density, energy efficiency, and cycling stability. For example, a new membrane with high selectivity can limit the crossover issue and help to increase the coulombic efficiency, energy efficiency, and long-term stability.^[33] Thus, new materials with suitable properties for redox-active molecules, electrodes, and membranes are important for the next-generation of RFBs.

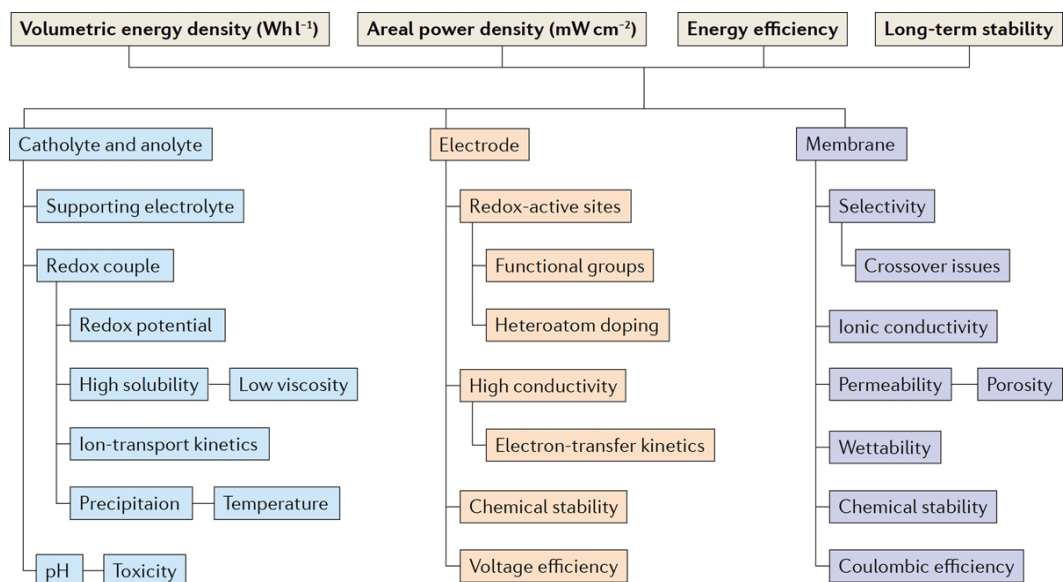
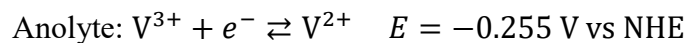


Figure 1.3. Considerations for the development of flow batteries. Reprinted with permission from reference 31. Copyright © 2016 Rights Managed by Springer Nature.

1.2.4.1 Materials for Redox-active Electrolytes, Electrodes, and Membranes in Aqueous RFBs

Redox-Active Materials. The redox-active molecule has a crucial effect on the performance of an RFB. Its redox potential, solubility, and electrochemical kinetics can affect the applicable power density of a flow battery. An electrolyte with low viscosity will decrease not only the diffusion overpotential but also limit the energy needed from the pumps. Since NASA invented the Fe–Cr RFB in the 1970s, various redox-active materials based on metals have been introduced to the flow batteries. For example, Zn/Br,^[34] Zn/Ce,^[35] Zn/Ni,^[36] all-Fe³⁺,^[37] Cd/Fe,^[38] Pb/PbO₂,^[39] Ti/Fe,^[40] all-Cu,^[41] Zn/MnO₂,^[42] and S/I^[43] have been studied. One of the most successful one is the vanadium RFB (VRFB), which was patented by Skyllas–Kazacos and Robins in 1986.^[44] The VRFB use a V²⁺/V³⁺ couple and a VO²⁺/VO²⁺ couple in sulfuric acid as the anolyte and catholyte, respectively. Their redox reaction is shown below.



Though the use of four oxidation states in VRFBs helps to limit the crossover issue and mitigate the capacity decay, this first generation of VRFBs is limited by a narrow working temperature range (10–40 °C) and a low energy density (15–25 Wh kg⁻¹).^[45] After the VRFB patent expired in 2006, more research institutes and companies started to study and make significant progresses in VRFBs, and they have been studied for the past three decades, making them the most successful RFBs to date. The Vanitec websites lists more than 26 companies that use VRFB technology, including projects such as the Minami Hayakita Substation built by Sumitomo Electric Ind. in Japan (15 MW and 60 MWh), the energy storage station at the Fraunhofer ICT in Pfinztal (2 MW and 20 MWh), the solar-powered vanadium flow battery (VFB) built by Invinity Energy in Yadlamalka (2 MW and 8 MWh), and the largest VRFB storage station designed by Rongke Power of China (200 MW and 800 MWh) that are already or are being installed.^[46]

However, strongly corrosive electrolytes, parasite reactions (e.g., hydrogen evolution in strongly acid solution), and cross-contamination limit their commercial success. Additionally, almost 43% of the total cost comes from the scarce raw material, the V₂O₅ precursor (Figure 1.4). Thus, these limitations of metal-based RFBs encourages researchers to pursue organic RFBs.^[47, 48]

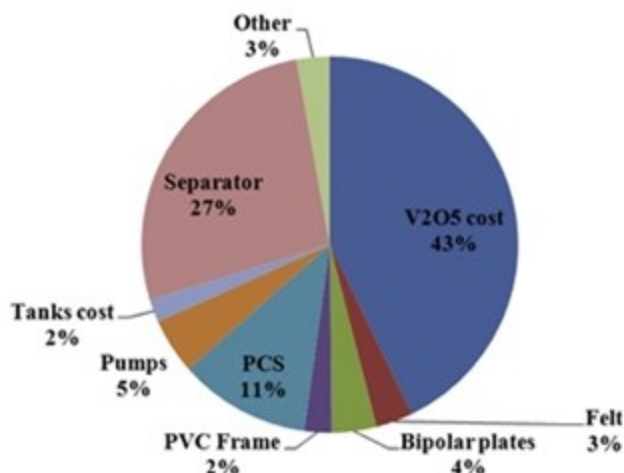


Figure 1.4. Distribution of costs for 4 MWh all vanadium RFB. Reprinted with permission from reference 49. Copyright (2014) Elsevier.

Organic and metal organic compounds with high molecular diversity and relatively large size are capable of mitigating the crossover issue in RFBs.^[5] The long study of organic chemistry provides a good platform for molecular engineering to optimize the redox potential, solubility, kinetics, electron number, and chemical and electrochemical stability through simple synthetic methods. Due to the tailorable properties of organic and metal organic molecules, the flow batteries parameters, including voltage, specific capacity, energy efficiency, and cycling stability, are designable. Besides, recent developments in computational simulations provide the researchers with a good way to forecast their properties before synthesis.^[50] Thus, organic RFB is a promising candidate for the next-generation of energy storage systems.

Metal organic compounds based on iron ions, such as Fe(II)-TEOA,^[51] ferrocyanide,^[52] Prussian blue,^[53] ferrocene,^[54, 55] ferriin,^[56] and Fe(III) azamacrocycles,^[57] have been introduced as electroactive materials in RFBs. For example, the Aziz group synthesized quaternary ammonium-functionalized, highly water-soluble ferrocene molecules (BTMAP-Fc, see Figure 1.5).^[58] The solubility of BTMAP-Fc is 1.9 M in water at 20 °C. The quaternary ammonium group also helps to retard the bimolecular decomposition of the ferrocene. When coupled with a viologen derivative anolyte, the RFB shows a cell voltage of 0.75 V, with a capacity retention of 98.58% over 250 cycles. Other metal organic compounds, such as cobalt, chromium, aluminum, and zinc complexes, also have been studied at the nascent stage.^[59-63]

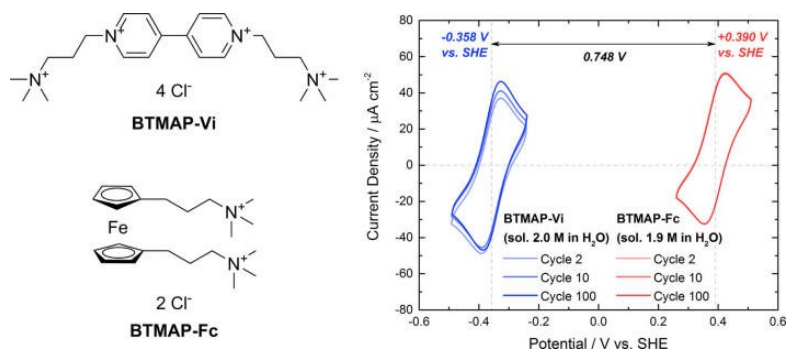


Figure 1.5 Chemical structure and cyclic voltammograms (CV) of BTMAP-Vi and BTMAP-Fc. Condition for CV: 1.0 mM in 0.5 M NaCl (aq) at a scan rate of 10 mV s⁻¹. Reprinted with permission from reference 58. Copyright (2017) American Chemical Society.

In aqueous organic RFBs, some organic redox-active derivatives from quinone,^[13, 64-66] viologen,^[67-71] 2,2,6,6-Tetramethyl-1-piperidinyloxy(TEMPO),^[72] indigo,^[73] alloxazine,^[74, 75] nitronyl nitroxide,^[76] phenothiazine,^[77] and phenazine^[78, 79] have been investigated, and their redox potential, electrochemical kinetics, solubility, and chemical and electrochemical stability also have been optimized through molecular engineering. For example, quinone derivatives have emerged as promising candidates for aqueous RFBs. As one member of the quinone family, 2,6-dihydroxyanthraquinone (2,6-DHAQ), is coupled with $K_4[Fe(CN)_6]$ as the catholyte in alkaline electrolyte to be applied in aqueous RFB.^[52] The 2,6-DHAQ has a high solubility >0.6 M in 1 M KOH. Besides, the redox potential shifts to more negative under alkaline condition. The cells delivered a voltage of 1.2 V with a 0.1% loss in capacity per cycle over 100 cycles. Based on rational screening and molecular engineering, various functional groups (e.g., carboxylic, phosphonate, sulfonate, polyethylene glycol) have been attached to the quinone backbone to pursue higher energy density in a less basic environment.^[13, 64, 66, 80] However, computational and experimental analyses indicated the quinone could undergo decomposition in aqueous systems through a Michael addition and/or *gem*-diol formation. Therefore, further modification or finding of new organic/metal organic redox-active materials, which can provide high potential with good stability in water, are essential for the development of aqueous RFBs.^[81]

A polymer has a high molar mass and large molecule size, allowing the use of inexpensive size-exclusion membrane. The polymerization of TEMPO and viologen have been prepared in the study of aqueous RFBs. A porous cellulose-based dialysis membrane was used and the RFBs show good cycling stability without any obvious crossover problem.^[26, 82-84] However, limited solubility and large viscosity restrict their capacity and applicable current density.^[23]

Electrodes. The electrodes in the RFBs do not participate in the redox reaction of either the catholyte or anolyte but provide a large active surface for the redox reaction. Electrodes need to have the feature of high electrical conductivity, large surface area, excellent stability in an operating potential window and an electrolyte environment, and a good affinity to the electrolyte. Carbon paper/felt frequently are

used as an electrode material in RFBs due to their good chemical and electrochemical stability as well as low electric resistance. To enable high redox kinetics of electroactive materials in aqueous RFBs, oxygen plasma, heat treatment, doping, electrochemical exfoliation, and nanomaterials have been applied to modify the carbon surface to increase the hydrophilicity of carbon based electrode.^[61, 85-89] However, most of the research in the optimization of electrodes focuses on VRFBs. Recently, the rapid development of study on aqueous organic RFBs also accompanies the need for optimized electrodes.

Membrane. The membrane helps to balance the charge in the RFBs by only allowing the supporting salt transfer but blocking the redox-active species. The crossover redox active molecule will lead to coulombic efficiency loss and capacity decay. Thus, the selectivity and permeability of the membrane are important parameters that affect the performance of an RFB. The selectivity of a membrane is caused by the effect of electrostatic exclusion, physical blocking, and Donnan exclusion. The trade-off between ionic conductivity and selectivity is a bottleneck in the development of a membrane. The perfluorinated sulfonated membranes, such as Dupont's Nafion series, provide good chemical stability and high proton conductivity and are used widely in VRFBs. However, their low ion selectivity and high cost hinder their application.^[45] Recently, numerous efforts have been spent on fabricating high-performance membranes based on various materials (e.g., graphene,^[90, 91] hexagonal boron nitride,^[92] polyimide,^[93]), pore size,^[94] selective layers,^[95, 96] fillers,^[97] and functional groups.^[33] New electroactive materials based polymers^[82] and nanomaterials^[98] have been introduced to minimize the crossover and provide a another way to choose cheap porous membranes. Besides the conductivity and selectivity, other parameters, such as water uptake, electrical resistance, chemical stability, cost, and mechanical firmness, also should be considered when choosing an ideal membrane. The concept of designing a biphasic system formed by an immiscible electrolyte (one acidic solution and one ionic liquid) for membrane-free RFB offers another promising way to simplify the system and reduce the total installation cost.^[99]

1.3 Evaluation Criteria for Redox-active Electrolytes in Aqueous Redox Flow Batteries

1.3.1 Physicochemical Properties of Redox-active Molecules

Solubility. The solubility indicates the maximum amount of the redox-active materials that can be dissolved in the solution. Increasing the solubility will help to increase the theoretical volumetric capacity and energy density. The solubility of a redox-active molecule is affected highly by the solution environment and its own structure in the solution. The dissolution is a competition between solvation of a solute molecule and solute–solute interaction.^[100] In the aqueous system, the hydrogen bond plays an important role in affecting the solubility of some molecules. Screening the intermolecular hydrogen bond within solute molecules or increasing the hydrogen bonding between the solute and solvent molecules could help to increase the solubility.^[62, 79] If the redox-active molecules contain some functional group, such as sulfonic, carboxylic acid, phosphonic acids, amino, ammonium, and hydroxyl, their solubility could be highly pH-dependent in an aqueous system. Thus, it is necessary to report the solubility at a specific pH if the materials are pH-sensitive.

Number of electrons. The number of electrons involved in the redox reaction in the RFBs also affects the theoretical volumetric capacity and energy density. Typically, the redox reaction in the RFBs is a one-electron transfer on the side of either the catholyte or anolyte. To achieve multielectron storage molecules can help to boost the energy density. Organic species, as a new promising candidate in RFBs, provide the possible multielectron transfer reaction for RFBs.

Stability. The chemical and electrochemical stability directly impact the cycling stability of a cell. In contrast to metal ions, organic materials tend to undergo side reactions, especially via the formation of radicals. For example, TEMPO suffers a disproportionation reaction when $\text{pH} < 2.5$.^[3] Thus, to design a stable redox-active electrolyte is of great importance for high-performance RFBs and, in particular, for organic RFBs.

Redox potential. The redox potential is a key parameter for determining the output cell voltage, which will affect the powder and energy density further. A high oxidation potential of catholyte and low reduction potential of anolyte favor high voltage in RFBs. For organic or metal-organic materials, the redox potential is determined by the energy level of the highest occupied molecular orbital (HOMO) and lowest unoccupied molecular orbital (LUMO), which is tunable through molecular engineering. In an aqueous system, the electroactive molecule also can be affected by the solution environment. Some molecules may have a different stable formation in a different pH, which can affect its HOMO or LUMO. Besides, some redox reactions involve proton-coupled electron-transfer reactions. Their redox potentials are affected by pH and can be identified from a Pourbaix diagram.

Electrochemical kinetics. The diffusion coefficient (D) and heterogeneous electron transfer rate constant (k^0) are the two important factors that determine the electrochemical kinetics of an RFB. The diffusion coefficient describes the redox-active species from the bulk solution to an electrode surface. It is affected by the size of the molecules, viscosity of the solution, and the temperature. A heterogeneous electron transfer rate describes the heterogeneous electron transfer between redox-active species and the electrode surface. It is affected by the nature of the molecules, the environment of the molecules (e.g., if they have interactions with the solvent molecules), the material and morphology of the electrode, as well as the temperature. The diffusion coefficient and rate constant affect the mass-transfer overpotential and activation overpotential, respectively. These will impact the applicable current, voltage efficiency, and energy efficiency further. A higher diffusion coefficient and rate constant result in lower mass-transfer overpotential and activation overpotential.

1.3.2 Electrochemical Characterization of Redox-active Molecules

Recently, issues such as sluggish electrocatalysis in water splitting, low reaction rates and poor selectivity in carbon dioxide reduction, uncertain insertion reaction mechanism in zinc ion battery, and low voltage efficiency, as well as limited applicable current density in redox flow battery, are in urgent need of being solved before achieving better performance.^[3, 101-103] Electrochemical characterization, as a key tool

to probe the electrochemical properties (e.g., thermodynamic, kinetics, and electrochemical stability) of redox reactions, is of great importance in understanding reaction mechanism, thereby providing essential insights in optimization of system or molecular design and engineering.^[104, 105]

Electrochemistry is a branch of chemistry that deals with the study of chemical changes caused by the passage of current or production of electrical energy from a chemical reaction. An electrochemical redox process, $O + e \rightleftharpoons R$, involves an electroactive species diffusing from the bulk solution to the electrode surface and a heterogeneous charge transfer from the electroactive species to the electrode or vice versa, depending on the applied electrode potential. The electrochemical characterization in RFB can be categorized as in-situ versus ex-situ. In the ex-situ electrochemical experiments, various electrochemical techniques have been applied in the RFBS, for example, cyclic voltammetry, rotating disk electrode, chronoamperometry, and sampled current voltammetry.

1.3.2.1 Ex-situ Electrochemical Characterization of Redox-active Molecules

Cyclic voltammetry (CV) is the most widely used voltammetric technique to study the charge-transfer kinetics of electroactive species. A classic three electrodes setup is shown in Figure 1.6. In CV experiments, current–potential curves are obtained by applying a potential at a scan rate (v), ranging from a few mV/s to a few V/s, and recording the corresponding current. CV is a reversal technique; the potential is scanned from a starting potential (E_1) to either an anodic or cathodic potential (E_2) and then reversed back to a final potential (E_3). Linear sweep voltammetry (LSV) is a unidirectional scan, i.e., from E_1 to E_2 . The features in the current–potential curves in cyclic voltammograms (CVs) are characteristic of the formal potential, reaction mechanisms, kinetics, and diffusional mass transport.

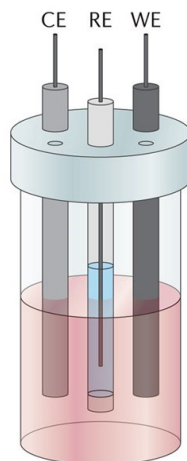


Figure 1.6. Schematic representation of a typical cyclic voltammetry setup with a counter electrode (CE) a working electrode (WE), and a reference electrode (RE). Reprinted with permission from reference 106. Copyright © 2017 Rights Managed by Springer Nature.

A rotating disk electrode (RDE) is one of the hydrodynamic electrochemical techniques that has been used frequently in redox flow batteries to study the electrochemical kinetics of the encountered redox species. An RDE cell setup is shown in Figure 1.7. The RDE shaft is made of a rod (e.g., Pt, Au, or glassy carbon) embedded into an insulating material (e.g., PTFE and PEEK). The rotation of the rod is driven by a motor at constant angular velocity (ω , where $\omega = 2\pi f$ and f is the rotation speed in rpm). As a result of the rotation, the hydrodynamic flow moves the solution horizontally away from the center of the electrode and, consequently, replenishes the solution by a flow normal to the electrode surface. Such forced convection in RDE allows for (1) a high rate of steady-state mass transfer and (2) controlling the diffusion layer thickness (δ , where $\delta = 1.61D^{1/3}\nu^{1/6}\omega^{-1/2}$, and ν is the kinematic viscosity of the solution) as a function of the rotation speed. Due to the steady-state mass transfer in RDE systems, current–potential curves of S-shape are observed, compared to a duck-shape for stationary (unstirred) cyclic voltammograms relying on the growth of the diffusion layer throughout the scan. The RDE study helps to ex-situ investigate the reaction mechanisms, mass transport, and electrochemical kinetics of the redox-active molecules.

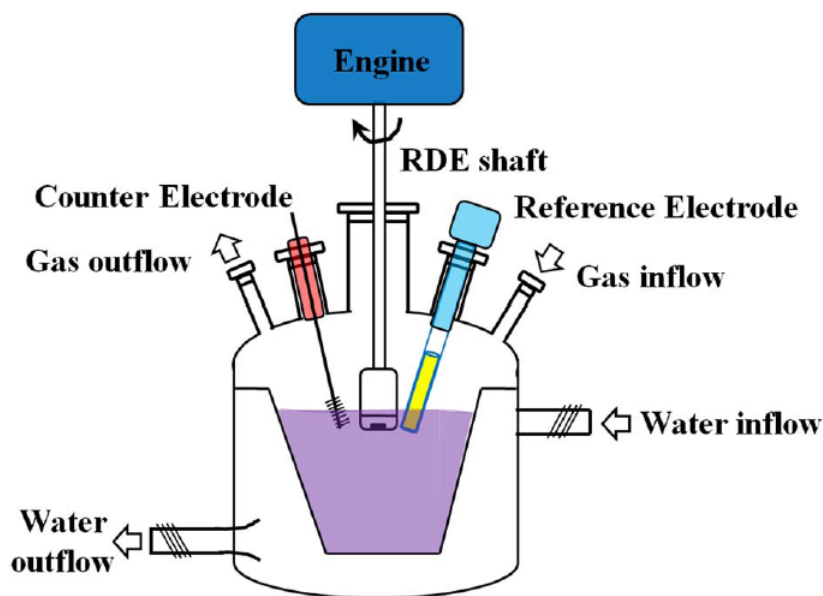


Figure 1.7. Schematic representation of a typical rotating disk electrode cell setup. Reprinted with permission from reference 107 with permission from IOP Publishing.

Sampled current voltammetry and chronoamperometry are electrochemical methods based on applying a potential step or a series of potential steps (usually from a rest potential to a set potential). For sampled current voltammetry, the current at a fixed time ($t = \tau$) is sampled after each potential step to obtain a sigmoidal current versus a potential curve that is similar to the steady state voltammogram under convection, whereas in chronoamperometry, the change of current as the function of time is recorded.^[108] Even though sampled current voltammetry is not as popular as CV and RDE in RFBs, its advantage in studying electrochemical reversible reactions make it a good supplementary method for the electrochemical study of RFBs.^[109]

1.3.2.2 In-situ Electrochemical Characterization of Redox-active Molecules

In-situ experiments provide a good chance to characterize the material under a realistic reaction environment. In the RFBs, methods such as charge and discharge curve, cycling, polarization curves, and electrochemical impedance spectroscopy are used to investigate the electrochemical properties of redox-active molecules in a real RFB.

Charge and discharge curves are used widely to characterize the performance of a battery. In the constant-current charge/discharge curves, the voltage keeps in a stable range until the discharge/charge is almost complete, where the mass-transfer

overpotential substantially contributes to the total voltage. From the charge/discharge curve, the efficiency, including voltage efficiency, coulombic efficiency, and energy efficiency, can be obtained; these help to investigate the reaction kinetics and mass transfer and ohmic properties of a cell. If the charge/discharge curves are sensitive to the current, it could be caused by high ohmic loss, sluggish kinetics, or poor mass transfer. Generally, the voltage efficiency decreases with current, while the coulombic efficiency increases with current (caused by, e.g., a side reaction and a cross over issue). An applicable current range can be achieved while maintaining acceptable efficiency, which helps to optimize the performance of the RFBs.

A cycling test studies the capacity retention with the cycle number or time. A cycling experiment offers an accessible way to study the degradation of electroactive materials in an RFB. The capacity retention is affected mainly by the stability of the redox-active materials, which provides the proof of improvement resulting from molecular design and engineering.

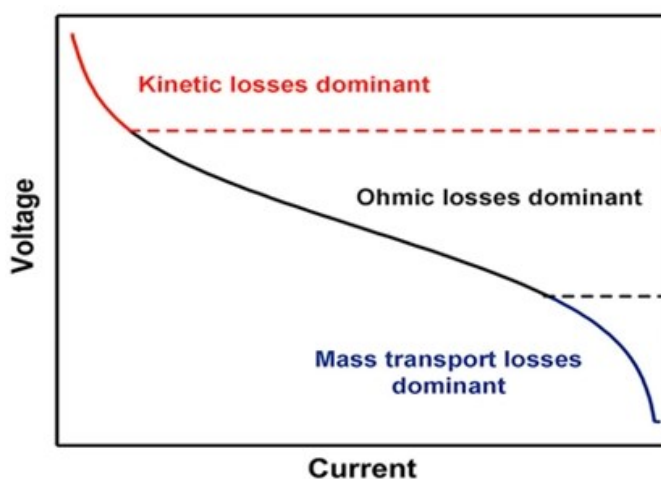


Figure 1.8. Polarization curve for a redox flow battery device. Reprinted with permission from reference 10. Copyright (2020) American Chemical Society.

A polarization curve usually describes the relationship between the output voltage and current. As shown in the Figure 1.8, it is a composite of kinetic losses, ohmic losses, and mass transport losses. In a low current region, the voltage losses are controlled by the electrochemical kinetics of the redox-active species, which can be

illustrated by the Butler–Volmer model. This region indicates the overpotential required to overcome the electrochemical activation energy for the redox reaction. Sluggish kinetics leads to a steep drop in this region, and vice versa. In a moderate current region, a linear relationship between voltage and current is depicted. The voltage losses are controlled mainly by ohmic resistance contributed by the electron collector, electrodes, membrane, electrolyte, external wire, and all contacts. The domination of ohmic resistance usually comes from the membrane. Thus, a low-resistance membrane with high selectivity is indispensable for a high-performance RFB. In a high current region, the voltage losses are contributed mainly by concentration polarization, where the limited redox-active species diffuse to and from the electrode surface, preventing the increase of the current. Even though the three dominants affect the voltage at all currents, the contribution from these dominated regions still can provide insight on how to optimize the RFBs. Besides, the maximum power, which is the result of voltage multiplied by current, can be calculated when the voltage decreases with current in the polarization curve.

Compared with other methods (e.g., CV, chronoamperometry), which induce large perturbations on the electrode–solution interface by driving the conditions far from equilibrium, electrochemical impedance spectroscopy (EIS) offers a way to measure small amplitude perturbations under steady state through applying a small alternating signal. Due to usually working near the equilibrium and small perturbations, the relationship between current and potential can be regarded as linear to simplify the process. When a system contains both O and R and reaches equilibrium (e.g., 50% of O and 50% of R), the impedance is measured as a function of the frequency of the AC signal, and an equivalent electrical circuit is constructed to describe the interfacial phenomena. For an RFB based on a heterogeneous charge-transfer reaction, the total current, comprised of the faradic current (i_f) and double layer charging current (i_c), will run between electrodes where ohmic resistance exists. At the electrode surface, the double layer capacitance can be regarded as an electrical capacitance, represented by C_d in the equivalent circuit, which contributes to the charging current in the total current. In parallel, the faradic current is produced by electron transfer with the electrode, which

is affected by the electron-transfer rate (charge-transfer kinetics) and the mass-transfer rate. Therefore, the charge-transfer resistance (R_{ct}) and Warburg element (Z_w) are applied to represent the kinetic effect and mass-transfer effect, respectively. Figure 1.9 shows a classic equivalent circuit under this situation, which is also known as the Randles circuit.

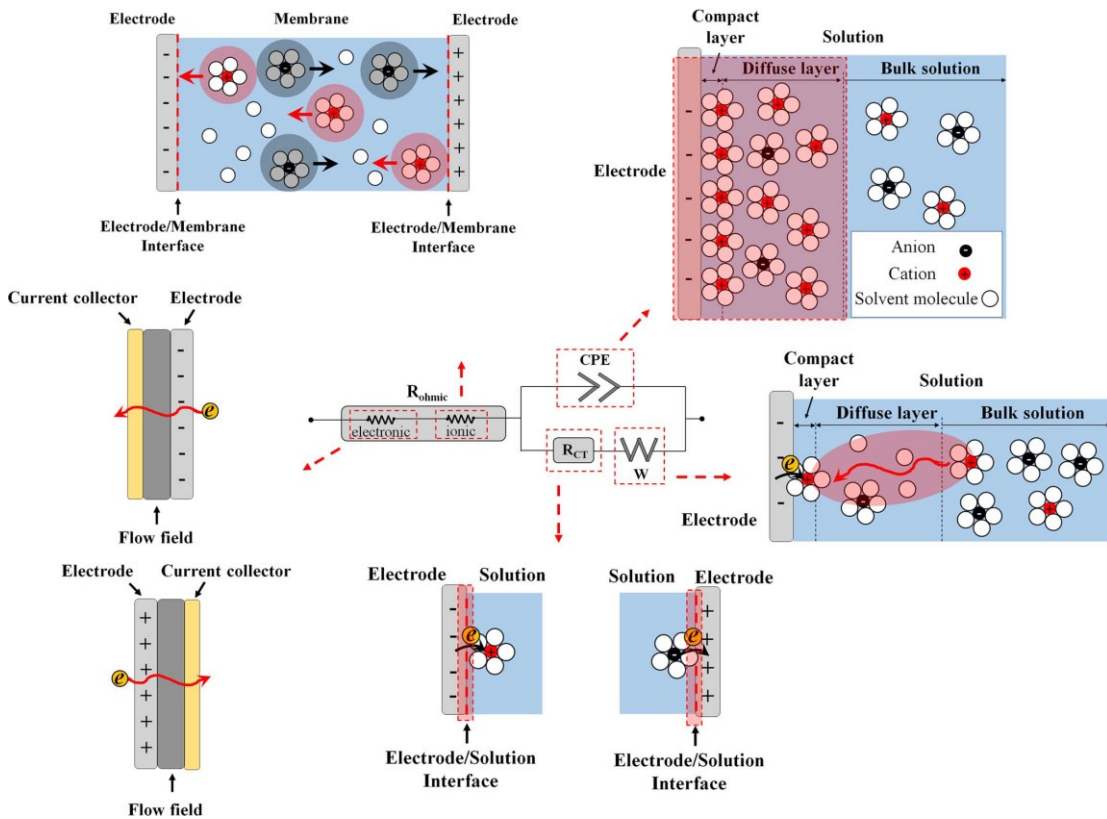


Figure 1.9. Equivalent circuit for typical redox flow battery. Reprinted with permission from reference 107 with permission from IOP Publishing.

To account for the behavior of the double layer capacitance departure from the ideal capacitive behavior, which may be contributed by surface heterogeneity or a specific time-constant distribution for a charge-transfer reaction,^[110] a constant-phase-element (CPE) could be used to replace the capacitance C_d for a better fit to the impedance data. However, it is inaccurate to use the CPE directly as the interfacial capacitance (C_{eff}); some methods have been proposed to determine the interfacial capacitance from CPE.^[110-112] The total impedance for an electrochemical cell contains real and imaginary parts. By plotting the $-Z_{im}$ vs Z_{Re} with the change of the frequency

(ω), a Nyquist plot is created. Although some commercial software now can help to fit the impedance data, it is not suggested to add or change a component to fit the data. Impedance is not unique to an equivalent circuit; it is used to guarantee the equivalent circuit describing the physics of the system better before using the model.^[113] Besides, factors such as electrode surface roughness or heterogeneity can have a large influence on the AC response.^[114] Thus, it is better to use EIS as a complementary method to some of the large perturbations techniques in order to back up the data obtained from it.^[115]

1.4 Principle of Molecular Engineering of Redox-active Molecules

Vanadium RFBs, which represent the state-of-the-art of aqueous redox flow batteries (ARFBs), have been studied for over 3 decades and successfully commercialized.^[2] The overall cost of a VRFB system is between \$400 to \$500 per kWh,^[116] which is substantially higher than the cost target of \$100 per kWh set by the U.S. Department of Energy (DOE).^[117] In VRFBs, the two major costs come from the active materials themselves and the ion-exchange membrane (Figure 1.4). Huskinson et al. found that the cost of a redox-active electrolyte can be as low as \$27 kWh, for anthraquinone disulfonate/bromide system, which is significantly lower than the cost of \$81 kWh for VRFB systems.^[80] In addition, considering the cost and safety issue, compared with using sulfuric acid as supporting salts, neutral salts such as sodium chloride are the recommended electrolyte for RFBs.^[3] Furthermore, due to the low solubility of VO_2SO_4 , VSO_4 , and $\text{V}_2(\text{SO}_4)_3$ at low temperatures and precipitation of V_2O_5 at elevated temperatures, the VRFB has a limited 2 M concentration window for electrolyte with a narrow working temperature from 10 °C to 40 °C. Therefore, extra costs for active temperature management is needed for VRFB systems, which will also lower the overall efficiency.^[116]

RFBs based upon organic and coordination compounds were proposed as the next-generation of RFBs for energy storage systems.^[14] Compared with traditional VRFBs, organic or coordination compounds-based RFBs have some advantages. For

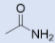

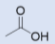
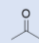
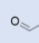
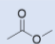
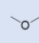
example, organic compounds comprise earth-abundant elements that can be low cost and can be scaled to large production volumes.^[14] Many organic and coordination compounds can support multi-electron redox reactions, which can help to increase the energy density of the RFBs.^[118] As well, RFBs based on using inexpensive neutral supporting electrolytes such as aqueous sodium chloride or potassium chloride lower the cost of the RFBs, and improve their safety profiles. Furthermore, organic and coordination compounds with large molecular sizes can reduce the crossover problem across the membrane.^[119] As described recently, the challenges for organic and coordination compounds based on ARFBs include chemical/electrochemical stability, solubility, and redox potential.^[14] Due to the tunability of their chemical and physical properties,^[31] molecular design and engineering provide an important path for boosting and optimizing the physicochemical and electrochemical properties of redox-active materials to meet the requirement of high-performance RFBs. In this section, we overview the molecular engineering strategies applied in the RFBs, especially in aqueous systems.

Solubility. The theoretical volumetric capacity and energy density are affected largely by the solubility in the solvent used to prepare the electrolyte. Increasing the solubility is an obvious route to building a high energy density into an RFB. Dissolution is based upon competition between solvation of a molecule in solution and solute–solute interactions in the solid state.^[100] The intermolecular forces include hydrogen bonding, ionic bonding, ion-induced dipole forces, ion–dipole forces, and Van der Waals dispersion forces that bind the solute molecules together. To dissolve the solute in a solution, the solute–solution interactions need to be larger than the intermolecular forces between the solutes. For example, in the case of the dissolution of a salt containing positive and negative ions, held together by ionic bonding, the solvation energy of the ions needs to be higher than the lattice energy.^[120] Thus, the dielectric constant of the solution, which helps to decrease the interaction between ions and the lattice energy of the solute, can impact the dissolution of a solute in a certain solution.

Another parameter that affects solubility is the polarity of the solute. Generally, polar solutes tend to be more easily dissolved in a polar solvent, while non-polar solutes

show better dissolution in a non-polar solvent.^[121] This simple trend or ‘rule of thumb’ can help to predict the solubility of an organic compound in a solvent. Non-polar organic molecules usually are not soluble in water but, instead, are highly soluble in a non-polar organic solvent. Table 1.1 shows a ranking of some classic functional groups by polarity.^[122] Functionalizing the non-polar organic molecules with polar functional groups can help to increase their solubility in the polar solutions, and vice versa.

Table 1.1. Rank of Functional Groups by Polarity

Functional group name	Functional group structure	Polarity
Amide		
Acid		
Alcohol	HO—	
Ketone		
Aldehyde		
Amine	H ₂ N—	
Ester		
Ether		
Alkane	H ₃ C—	

Apart from the general principles, other possible rules also have been proposed to enhance either the interaction between solution and solute or depress the interaction between solute and solute for higher solubility.^[123] For example, Hollas et al found that increasing the asymmetry and charge of the phenazine backbone by introducing functional groups via rational molecular engineering can facilitate the competition between counterions and solvent molecules to solvate specific regions of the solute preferentially.^[124] Kwabi et al functionalized 2,6-dihydroxyanthraquinone (2,6-DHAQ) with highly alkali-soluble carboxylate terminal groups. They found that the introduction of a short flexible chain could help to frustrate the crystallization, lowering the energy of solid state binding interactions and thus facilitating solvation.^[66] Sevov et al prepared a series metal-coordination complexes based on the tridentate

bipyridylimino isoindoline ligand. They found that charge shielding by the ligands can affect solubility. Early transition metals were expected to be more polar, and showed higher solubility in polar solvent like acetonitrile. [125, 126] In addition, for charged complexes, the impact of counterions on the solubility also must be considered. Counterions with hygroscopic properties could favor higher solubility in an aqueous solution.[73, 127]

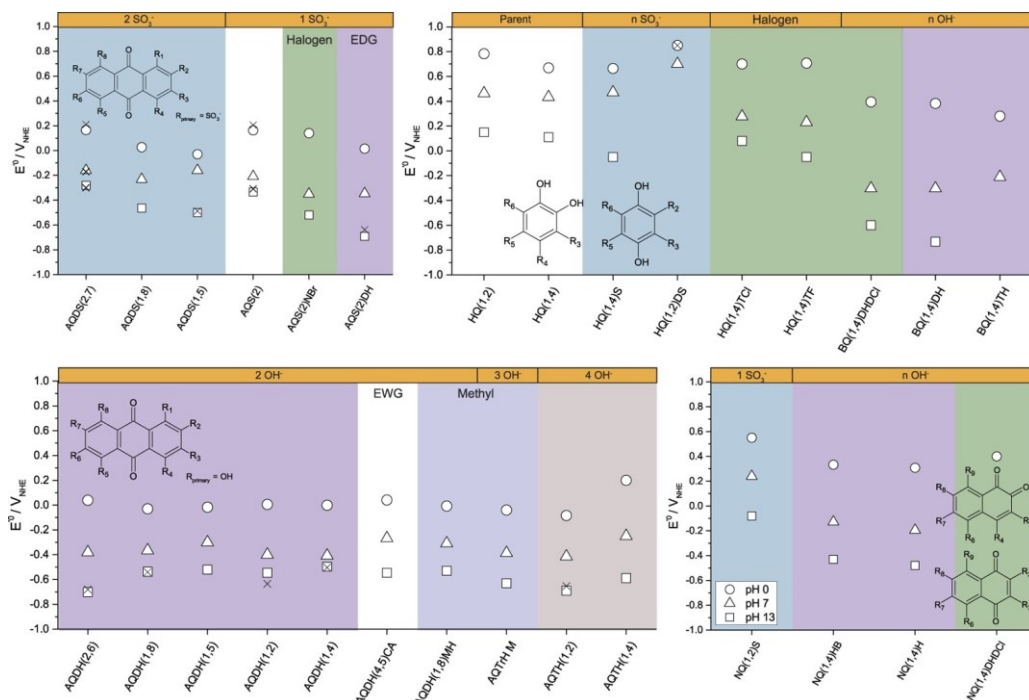


Figure 1.10. Experimental redox potential of various quinones at three different pH values. Reprinted with permission from reference 128 with permission from Springer Nature.

Redox potential. The tunable structure of organic and metal organic molecule provides the flexibility to tune the redox potential. The redox potential can be tuned, based on molecular engineering, through introducing electron-donating or electron-withdrawing functional groups. The electron-donating groups, such as amino ($-\text{NH}_2$), hydroxyl ($-\text{OH}$), and methyl ($-\text{Me}$), donate the electron density to the redox center, leading to the decrease of the redox potential. Conversely, the electron-withdrawing groups, such as fluoro ($-\text{F}$), carboxylic acid ($-\text{Cl}$), and sulfonic acid ($-\text{SO}_3\text{H}$), increase the electrophilicity of the redox center, resulting in the increase of the redox potential. In addition to tailoring the redox potential through substituting with various functional

groups, tuning the relative position of functional groups also affect the redox potential. As shown in the Figure 1.10, when functionalizing quinone with sulfonate groups, there is a higher electron-donating effect in position 1, 5, and 8 than in edge position 2 and 7. It also is noticed that a larger redox potential change can be achieved by increasing the number of functional groups.^[129]

Additionally, the redox potential of an electroactive molecule is affected not only by the structure but also by the physical and chemical environment of the supporting electrolyte. If a redox reaction is a proton-coupled electron-transfer reaction, the redox potential has a linear relationship with pH that can be described by the Pourbaix diagram based on Nernst equation.^[64] Therefore, by changing the pH, the redox potential of an electrolyte can also be altered.

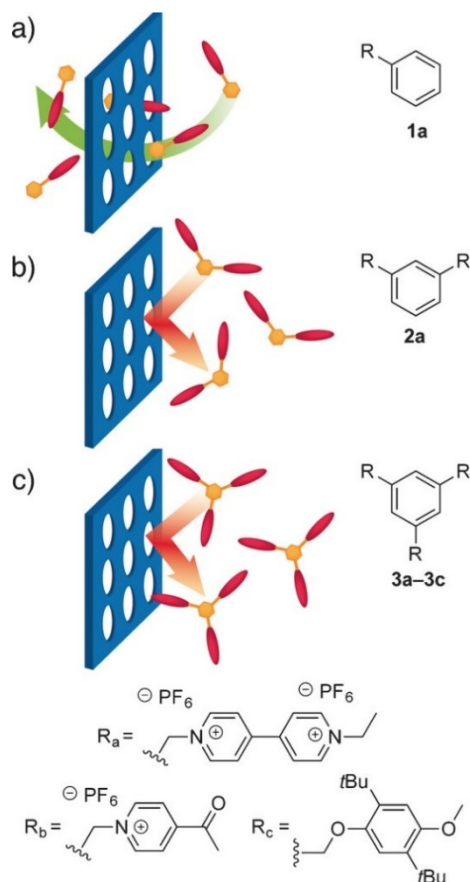


Figure 1.11. Macromolecular design strategies for size exclusion effect: (a) small size of electroactive organic molecules crossover the membrane; (b) and (c) larger size of oligomers are blocked from the microporous membrane. Reprinted with permission from reference 119. Copyright (2017) John Wiley and Sons.

Size. The crossover of redox-active molecules is an inevitable issue in RFBs. It affects not only the efficiency, but also causes the irreversible capacity loss during the charging and discharging, unless using a symmetric design. Compared with metal ions, organic molecules with a tunable structure can achieve an efficient size-exclusion effect. Electroactive monomers, oligomers, and polymers can work as soluble nanoscopic energy storing units to pursue inexpensive porous membrane for RFBs (Figure 1.11).^[130] For instance, redox-active molecules can be anchored to the backbone chain of the polymer or functionalized on a cross-linked polymer to form redox-active colloids as discrete energy storage carriers in RFBs.^[82, 131] However, with an increase in the size of the organic molecules, the electrochemical activity, solubility, and viscosity of the electrolyte could decrease. Rational molecular engineering is needed in designing various sizes of redox-active molecules for size-exclusion membranes.

Number of electrons. Various electroactive molecules, such as ferrocene,^[58] metal sulfide clusters,^[60] viologen,^[132] TEMPO,^[133] alloxazine,^[74] phenothiazine,^[134] tris(dialkyl)amino-cyclopropenium,^[135] N-hydroxyphthalimide,^[136] and dithiolene complexes,^[137] have been introduced to the RFBs. However, few good candidates are capable of storing multielectron, mainly due to their intrinsic redox properties, low stability, or solubility in their multi-charging state. For example, due to the intrinsic properties of ferrocene, it only undergoes a one-electron reversible redox reaction. Even though the Co₆S₈ metal sulfide cluster shows two redox couples at 0.09 V and 0.54 V vs Ag/AgCl, the second redox couple is not chemically stable on the time scale of the RFB testing.^[60] Methyl viologen (MV²⁺) is a widely used anolyte for aqueous RFBs. However, due to its neutral charged state (MV⁰), it is not water soluble, and only its stable MV^{2+/+} redox couple has been successfully applied in ARFBs.^[72] Therefore, researchers have tried to use molecular engineering strategies to overcome these challenges. For example, by introducing additional charge or π -conjugated extension to the viologen, the stable two-electron reduced viologen compounds were achieved.^[54, 71] Similarly, by investigating the instability of organic molecules, Sanford and Hansmann successfully designed and synthesized stable multi-redox acylpyridinium radical and pyridinium-carbene, respectively.^[138, 139]

In addition to the general rules mentioned above, the development of theoretical models in chemistry computational calculation provides a valuable way to predict these properties and virtually screen molecules before conducting laborious experiments (Figure 1.12). Based on high-throughput computations, the electrochemical and physiochemical properties of the redox-active molecules can be analyzed and a pool of candidates can be generated and down-selected.^[50]

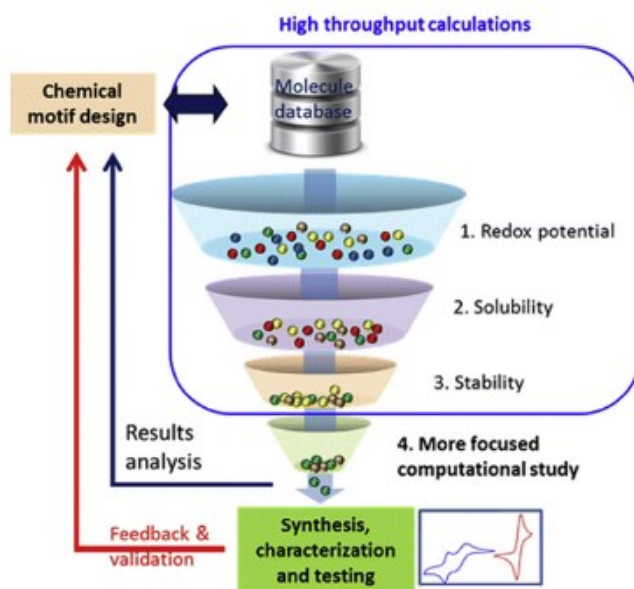


Figure 1.12. Down-selection of candidates for energy storage molecules based on quantum chemical calculations. Reprinted with permission from reference 50. Copyright (2015) American Chemical Society.

By using DFT calculations, solubility, redox potential, and stability can be calculated to help accelerate discovery of new electrolyte candidates.^[50, 78, 81, 140-142] Besides, machine learning (that predicts the properties of materials and establishes a function that maps a molecule to the property of choice) and deep learning (e.g., deep generative models that try to model the probability distribution of structure and properties in a nonlinear way) also can be applied in the rational design of molecules to achieve high performance RFBs.^[143] In future, with a more accurate theoretical model and insightful understanding of the chemical and physical properties of RFBs, a breakthrough in the development of high-performance organic RFBs is expected.

1.5 Scope of the Thesis

The purpose of the thesis is to design and characterize electrochemically the electroactive organic and metal organic molecules for high-performance aqueous redox flow batteries. It consists of five chapters, with the scope of each chapter provided below. Chapter 1 overviews the current status, advantages, and basic principles of the redox flow batteries. The physicochemical properties of electroactive molecules and electrochemical characterization methods used in RFBs have been discussed to provide a possible pathway for further optimization. General molecular engineering principles and guidelines for organic materials are highlighted to build high-performance aqueous RFBs.

Various new redox-active materials have been introduced to develop cost-effective and high-power-density next-generation RFBs. Electrochemical kinetics play critical roles in influencing RFB performance, notably, the overpotential and cell power density. Thus, determining the kinetic parameters for the redox-active species to be used is essential. In Chapter 2, we reviewed the limitations for recent electrochemical methods used in RFB and proposed a new electrochemical protocol to determine the kinetics of redox-active species in RFBs.

Aqueous symmetric redox flow batteries (RFBs) are of great interest due to the non-flammability and high conductivity of the solvent and the avoidance of irreversible anolyte crossover seen in asymmetric cells. In Chapter 3, we introduced a simple octahedral Co(II) complex, termed BCPIP-Co(II), that has four appended carboxylic groups on the ligand periphery that render it both water-soluble and pH-sensitive in the range of pH 1.5 – 5.5. The complex has BCPIP-Co(II-III) and BCPIP-Co(II-I) reversible redox couples within the water splitting window, as well as fast kinetics. The overall charge of the complex varies from +3 to -3, resulting from the level of deprotonation of the carboxylic acid moieties and the oxidation state of the cobalt metal center, both of which affect the resulting redox properties. Then, BCPIP-Co(II) was incorporated into a symmetric aqueous RFB as both the catholyte and anolyte. A high capacity retention of 99.9% per cycle over 100 cycles was demonstrated.

In order to achieve organic aqueous redox flow batteries, we introduced a series of phenazine derivatives as potential redox-active organic molecules for aqueous redox

flow batteries in Chapter 4. The phenazine backbone was functionalized with short flexible carbon chains that have been terminated with hydrophilic sulfonated groups to achieve high solubility in neutral aqueous solution. The sodium 3-(phenazin-2-yloxy)propane-1-sulfonate (PPSNa) showed a high solubility and a large range of pH-independent redox potentials. When coupled with $K_4Fe(CN)_6$ as catholyte, the cell showed a stable coulombic efficiencies (CE) near 100% with a capacity fade rate of 0.011% per cycle, which indicate a good candidate for true neutral organic aqueous redox flow batteries.

Recent advances and challenges to develop high-performance aqueous redox flow batteries are proposed and summarized in Chapter 5, and the summaries of the thesis and future research direction for practical applications of advanced organic redox flow batteries also are discussed.

Chapter 2

Determining Electrochemical Kinetic Parameters in Redox Flow Batteries[†]

2.1 Introduction

The main factors controlling RFB performance are the same as for most other electrochemical cells: (1) thermodynamics, reflected in the redox potential; (2) mass transport of redox components to the electrode; and (3) the electron transfer rate, embodied in k^0 , the heterogeneous electron-transfer rate constant. Substantial progress has been made toward the synthesis and development of redox species that have high solubilities, a large difference in redox potentials, the necessary stability to withstand repeated cycling, and facile electrochemical kinetics.^[55, 58, 74, 75, 144] The electrochemical kinetics of an RFB significantly impact the performance of the battery but also are critical to understand for elucidating reaction mechanisms. Developing a better understanding of the relevant reaction mechanisms is often necessary to enable further improvements of a given flow battery.

A good RFB requires favorable kinetic characteristics to enable usability over hundreds or thousands of cycles and to deliver a desirable potential window and current density. One should determine the reversibility of the redox reaction, kinetics, and charge-transfer mechanisms of a redox couple before integrating it within an RFB; this important information will enable rational improvements to the design of the battery. “Chemical reversibility” of redox reactions is essential for good cycle life in RFBs, whereas “electron transfer reversibility” indicates the rate of electron transfer between the electrodes and the redox components. Here, and in most electrochemical literature, the term “reversible” indicates a fast electron-transfer reaction that maintains thermodynamic equilibrium at the electrode/solution interface, whereas “irreversible” indicates a slow reaction that can limit the power output in RFBs seriously. “Quasireversible” refers to intermediate rates between these two extremes. Here, we will walk through the steps to determine the diffusion coefficient, the standard rate constant (kinetic facility of a given redox reaction), and the type of reversibility of the

electron transfer (ET) mechanism when considering possible redox couples for a redox flow battery application. Then, we will review the limitations for some electrochemical techniques used in RFBs and provide a new way to determine the kinetic parameters. For an excellent introduction to electrochemistry, we strongly encourage reading the recently published guide by Dempsey and co-workers.^[145]

The first sets of experiments one should start with are based upon cyclic voltammetry (CV), which will be used to determine if a given redox couple is reversible, quasireversible, or irreversible, and to realize a rough estimate of the rate constants and diffusion coefficients of reversible and irreversible systems. For the diffusion coefficient of a quasireversible system, rotating disk electrode (RDE) measurements are suggested. Second, more detailed RDE measurements can be deployed for further confirmation of the determined rate constants and diffusion coefficients of quasireversible and irreversible redox systems. Throughout, we will help to avoid missteps and pitfalls and walk through all of the steps to elucidate the important kinetic information on a candidate redox couple for RFB applications.

2.2 Determination of Reversibility and Basic Kinetic Information of a New Redox System

2.2.1 Determination of Reversibility

To begin analyzing your new redox system for an RFB, the first two points that need to be addressed are (1) the determination of the solubility/stability in different solvents and at different pH values of interest to RFB applications, followed by (2) the running of CV at different scan rates to determine the reversibility of the reaction and other important electrochemical parameters, such as the diffusion coefficient. Because the determination of electrochemical kinetic parameters varies from reversible to quasireversible or irreversible systems, experimentally defining the nature of the redox couple is the first step to be taken. As noted above, redox reactions are classified into three categories (1) electrochemically reversible; (2) electrochemically irreversible; (3) quasireversible, depending on the kinetics of the charge-transfer reaction between the electrodes and redox components.

For reversible systems, the processes are characterized by high rates of charge transfer (high standard rate constants, e.g., $k^0 > 10^{-1} \text{ cm s}^{-1}$).^[146] The measured current is dictated by the slowest process, the diffusional mass transport of redox species. The charge transfer for a reversible redox reaction ($\text{Ox} + e^- \rightleftharpoons \text{Red}$) occurs instantly at the electrode surface, and a dynamic equilibrium is established that corresponds to the Nernst relationship: electrode potential $E = E^{0'} + (RT/nF)\ln(\text{O}_{\text{surf}}/\text{R}_{\text{surf}})$.^[114] Thus, the surface concentrations are only a function of the electrode potential and are not influenced by the rate of charge transfer. Furthermore, the shape of the characteristic voltammograms is correlated to the potential-dependent changes in the surface concentrations as well as the accompanied diffusional mass transport. In a typical reductive CV scan for a reversible redox reaction (Figure 2.1), the scan starts at an electrode potential more positive than that for $E^{0'}$ and only a non-faradaic (capacitive) current, i_c , passes. As the potential scan approaches $E^{0'}$, reduction begins and a faradaic current starts to pass. This step should result in a decrease in the concentration of the oxidized species at the vicinity of the electrode surface, creating a diffusion layer. The increase in current with the continuous scan toward more negative potentials is attributed to the increasing flux to the surface across the diffusion layer.^[147] At potentials more negative than $E^{0'}$, the surface concentration of the oxidized species decreases and nearly approaches zero, resulting in maximum flux (current). At more negative potentials, the current then decays with a complete depletion of the oxidized species on the electrode surface.^[114, 147] These processes result in a peaked current–potential curve, Figure 2.1. Similar current–potential features typically are observed for a reverse scan. The peak current is related to the scan rate according to the Randles–Sevcik equation,

$$i_p = 2.69 \times 10^5 n^{3/2} A C^* D^{1/2} \nu^{1/2} \quad 2.1$$

at 25°C where C^* the bulk concentration. The diffusion coefficient, D , can be extracted from the slope of a linear plot of the peak current versus the square root of the scan rate.

Other criteria that describe reversible voltammograms are listed below:

- (1) $k^0 \gg \gg$ mass transfer coefficient;
- (2) peak potential (E_p) is independent of the scan rate;

(3) peak separation $\Delta E_p = 57/n$ mV;

(4) anodic peak current (i_{pa}) and cathodic peak (i_{pc}) current meet: $i_{pa}/i_{pc} = 1$.

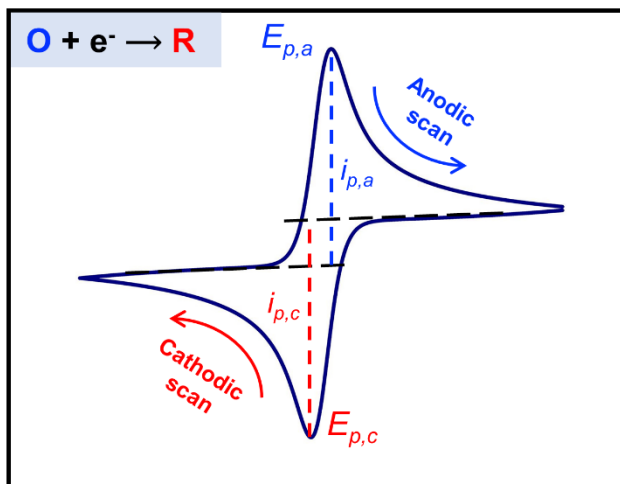


Figure 2.1. A simulated cyclic voltammogram for a reversible system showing the exact determination of peak current from the base line. This plot is expected with low background current (without redox species present), or after subtraction of the background current. Reprinted with permission from reference 10. Copyright (2020) American Chemical Society.

For irreversible systems, the processes typically are limited by sluggish charge-transfer kinetics (e.g., $k^0 < 10^{-5}$ cm s⁻¹).^[146] High overpotentials are required to drive charge transfer between the electrode surface and electroactive species, thus, large peak separations usually are observed, compared to those for reversible and quasireversible systems. No equilibrium is established, thus, the Nernst equation does not apply. The measured current is limited by the rate of the charge transfer, where the peak current is related to the rate constant according to

$$i_p = 0.227FAC^*k^0 \exp\left(\frac{-\alpha F(E_p - E^{0'})}{RT}\right) \quad 2.1$$

$$\Rightarrow \ln(i_p) = \ln(0.227FAk^0C^*) - \left(\frac{\alpha F}{RT}\right)(E_p - E^{0'})$$

Provided that $E^{0'}$ is known, a linear plot of $\ln(i_p)$ versus $(E_p - E^{0'})$ at different scan rates should give a slope of $-\alpha F/RT$ and an intercept that is a function of the rate constant k^0 . Other characteristics of irreversible redox systems are listed below:

(1) $k^0 \ll \ll$ mass transfer coefficient;

(2) $i_p = 2.99 \times 10^5 n^{3/2} \alpha^{1/2} AC^* D^{1/2} \nu^{1/2}$;

(3) E_p shifts to higher potential as the scan rate increases;

(4) $|E_p - E_p/2|$ mV at 25 °C.

For quasireversible systems, the processes fall into an intermediate regime between reversible and irreversible systems; in this regime, k^0 falls between 10^{-1} and 10^{-5} .^[146] The current is limited by both the charge-transfer kinetics and mass transport. Whichever of the two is the smallest (the rate-determining step) controls the reversibility of the redox reaction. The scan rate contributes significantly to the shape of cyclic voltammograms for quasireversible systems by altering the mass transfer coefficient $m_t = DFv/RT)^{1/2}m_t^{1/2}$.^[148] Matsuda and Ayabe^[149] proposed a dimensionless parameter (Λ), $\Lambda = k^0/DFv/RT)^{1/2}$, to determine the apparent reversibility of redox species according to the following kinetic zones:

Reversibility: $\Lambda > 15$

Quasireversible: $15 \geq \Lambda \geq 10^{-2(1+\alpha)}$

Irreversible: $\Lambda < 10^{-2(1+\alpha)}$

At a low scan rate, the shape of the CV approaches the reversible case as the ratio of k^0/m_t increases. At high scan rates, however, the k^0/m_t ratio decreases and the CV resembles that of the voltammogram of an irreversible redox reaction. We have noted a misunderstanding in the literature regarding the relationship between peak current and the square root of the scan rate for quasireversible systems. Please note that, in contrast to reversible and irreversible systems, i_p for quasireversible systems is not proportional to $v^{1/2}$ due to the transition from reversible to irreversible voltammograms with scan rate.^[150] Other criteria that describe quasireversible systems include:

(1) E_p depends on the scan rate;

(2) ΔE_p increases with the scan rate.^[114]

Therefore, for reversible systems, the current is limited only by diffusional mass transport and, in contrast, the current for irreversible systems is dominated by slow charge-transfer kinetics. The CV curves of quasireversible systems have intermediate shapes that are dependent on both charge-transfer rate and mass-transport conditions. Although the commonly used terms imply that redox reactions fall into three distinct groups, the range of observed rates is one continuum between “reversible” and “irreversible”, depending on the time scale of the technique used to monitor charge-

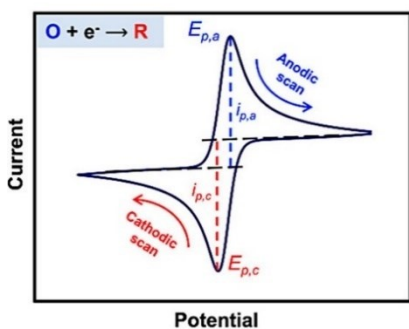
transfer kinetics. Figure 2.2 outlines the first set of experiments that should be performed to determine whether a redox reaction is reversible, quasireversible, or irreversible, and how to calculate the associated diffusion coefficient of the redox-active species in solution. We will first go through the details of reversible, quasireversible, and irreversible redox reactions and then determine the diffusion coefficients of the reactions.

As shown in Figure 2.2, steps 1 and 2, one begins with a CV characterization of the redox couple. For reversible systems, the current is limited only by diffusional mass transport, where the peak potentials, E_p , and peak separation, ΔE_p are independent of the scan rate. For irreversible systems, however, ΔE_p increases and E_p shifts to more extreme potentials with increasing scan rate (more positive for oxidation, negative for reduction). Quasireversible systems are influenced by both the charge-transfer kinetics and diffusional mass transport. As shown in Figure 2.2, step 2, the shapes of the CV curves and ΔE_p are used to discern reversibility. The next step, step 3a, is to run CVs at different scan rates to determine whether E_p shifts with the scan rate. If E_p does not shift with the scan rate, then the redox couple is defined as a reversible system, meaning that the rate of electron transfer is fast relative to the range of scan rates employed.

When conducting the CV experiments, there are a few key experimental points need to be considered.

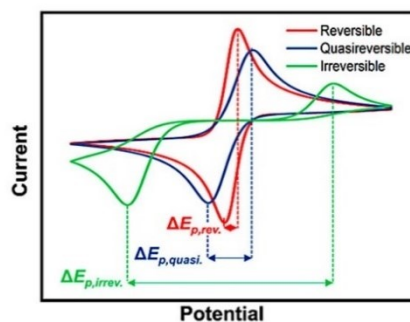
(1) First, precleaning of the working electrodes is highly essential to remove any contaminants on the surface that might mislead the measurements of the kinetic parameters; we refer to a useful tutorial by Dempsey and co-workers.^[145] A precleaning protocol usually starts with mechanical polishing of the electrode surface in a water–alumina slurry, followed by rinsing and sonicating in ultrapure water.^[145, 151, 152] Electrochemical cycling, until a steady-state is reached, also can be used subsequently to remove different kinds of surface contaminants further.^[151, 153]

Step 1 Carry out CV of redox couple



Run the CV at a reasonable scan rate, e.g., 50 mV/s.

Step 2 Define type of electron transfer mechanism



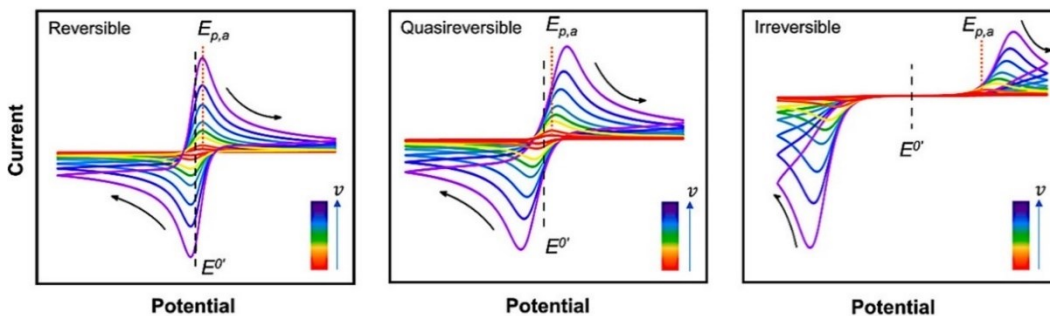
Determine the peak separation, ΔE_p . ΔE_p = anodic peak potential ($E_{p,a}$) - cathodic peak potential ($E_{p,c}$).

Reversible if $\Delta E_{p,rev.} = (57/n)$ mV where n = number of e⁻

Quasireversible if $\Delta E_{p,rev.} < \Delta E_{p,quasi.} \lesssim (200/n)$ mV *

Irreversible if $\Delta E_{p,irrev.} > (200/n)$ mV *

Step 3a Run CVs at different scan rates

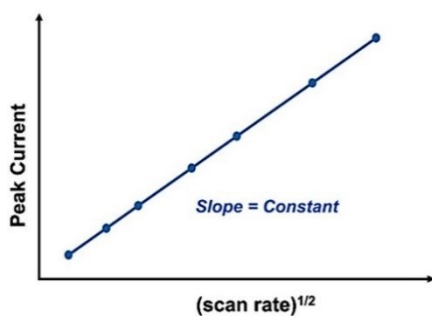


Correct for uncompensated resistance.^{14,15} (Detailed directions in Supplementary Information.)
If $E_{p,a}$ does not shift with scan rate (v), system is reversible.

Step 3b Determination of diffusion constant, D: plot peak current vs (scan rate)^{1/2}

Plot the change of peak current with square root of scan rate.

Reversible and irreversible systems are linear; quasireversible is not, and cannot be determined in this manner.



With a *reversible* system, use Randles-Sevcik equation to solve for D , the diffusion coefficient:

$$\text{Slope} = 2.69 \times 10^5 n^{3/2} A C' D^{1/2}$$

With an *irreversible* system, use

$$\text{Slope} = 2.99 \times 10^5 n^{3/2} \alpha^{1/2} A C' D^{1/2}$$

where α can be estimated from $|E_p - E_{p/2}| = (48/\alpha n)$ mV, where E_p and $E_{p/2}$ correspond to the potentials at peak current and half the peak current, respectively.

Figure 2.2. First set of cyclic voltammetry (CV) experiments to define the kinetic regimes (reversible, quasireversible, and irreversible) for an electron transfer (ET) mechanism (steps 1 – 3a). CVs for reversible, quasireversible, and irreversible systems were simulated using Bio-Logic EC-Lab software. Parameters: $k^0 = 0.5 \text{ cm s}^{-1}$ (reversible, red), 0.001 cm s^{-1} (quasireversible, blue), and $1 \times 10^{-6} \text{ cm s}^{-1}$ (irreversible, green); $v = 50 \text{ mV s}^{-1}$; diffusion coefficient ($D_0 = D_R$) = 1×10^{-5} . *The final potential range for the quasireversible system in step 2 [(200/n) mV] was chosen based on values obtained from the Nicholson equation, Table 2.2. Step 3b illustrates the representative linear relationship between the peak currents and the square root of scan rates $v^{1/2}$ for reversible and irreversible systems. Refer to Table 2.1 for a more detailed description of the symbols used in this figure. Reprinted with permission from reference 10. Copyright (2020) American Chemical Society.

(2) Second, the peak current can be used to determine various kinetic parameters for redox species of concern. For an accurate determination of the faradaic peak current, a correction has to be performed to cancel out the background current, resulting from (i) charging the electrode double layer (capacitive current) and (ii) redox reactions of adventitious species in the solvent or on the electrode surface (residual current). The capacitive current varies linearly with the scan rate ($i_c = AC_d v$, where i_c , A , C_d , and v are the capacitive current, electrode area, double-layer capacitance, and scan rate, respectively).^[114] Hence, a significant contribution from the capacitive current can be encountered at high scan rates.^[147, 152] To rule out the capacitive current, the actual value of the peak current should be measured from the baseline current at the initial stages of the voltammogram, Figure 2.1. Alternatively, at the same peak potential, the peak current can be determined by subtracting the background current of a separate cyclic voltammogram run at the same scan rate in the absence of the redox species.

(3) Third, while running cyclic voltammograms, the potentiostat controls the potential on the working electrode with respect to the reference electrode. However, the controlled potential ($E_{\text{Controlled}}$) is the sum of the actual potential (E_{Actual}) on the electrode surface and the ohmic potential (iR_u); $E_{\text{Controlled}} = E_{\text{Actual}} + iR_u$. The ohmic resistance, or uncompensated resistance (R_u), results from the resistance of the electrolyte as well as contact resistances. R_u can be determined by electrochemical impedance spectroscopy (EIS).^[152] The iR_u drop is a function of the measured faradaic current, which increases with $v^{1/2}$. Thus, increasing the scan rate results in increasing the ohmic drop and shifting the peak potential to higher values, inducing false peak separation (ΔE_p) between anodic and cathodic peaks. For an accurate determination of ΔE_p , it is recommended highly to correct the cyclic voltammograms for the potential drop resulting from the ohmic resistance.^[152, 154, 155]

2.2.2 Determination of the Diffusion Coefficient

The kinetics of the diffusion of a redox species are important for the performance of a redox flow battery because slow diffusion will restrict the current density and lead to larger overpotentials.^[156] The relationship between the peak current (corrected for the background current, Figure 2.1) and the square root of the scan rate, step 3b in Figure

2.2, is linear for reversible and irreversible systems, and the slope can be used to calculate the diffusion coefficient, D ; the relevant equations are shown in step 3b.^[114, 115] For quasireversible systems, however, the peak current is not proportional to the square root of the scan rate, and the diffusion coefficient needs to be determined through an alternate route (e.g., rotating disk electrode, RDE). A representative example for the deviation of i_p with $v^{1/2}$ for quasireversible systems is illustrated by Ohsaka and co-workers for oxygen reduction and oxidation reactions on a sub-self-assembled monolayer/Au electrode.^[157] Table 2.1 lists all of the symbols used here, as well as their units for clarity. At this point, you will have determined whether your redox couple is reversible, quasireversible, or irreversible, and the approximate diffusion coefficient, D , of the electroactive species in solutions for reversible and irreversible systems.

As mentioned above, for a quasireversible system, i_p with $v^{1/2}$ is nonlinear, thus, CV cannot be used, i.e., step 3b in Figure 2.2 is not applicable. To determine the diffusion coefficient of a quasireversible redox couple, it is suggested that an RDE be employed. Using an RDE also will enable the determination of the diffusion coefficient of reversible and irreversible systems because the mass-transport-limited diffusion current does not depend on either the electrode potential or the rate of the reaction but only on the diffusion and rotation rate.^[158] An RDE encounters a steady-state flux of analyte to the electrode surface, thus leading to the case where the current at a given potential is no longer dependent upon time.^[159] Due to the steady-state mass transport in RDEs, current–potential curves are S-shaped, as opposed to the typical duck-shape of stationary (unstirred) CVs that rely on the growth of the diffusion layer thickness and diffusion of the reactive analytes to and the redox products from the electrode throughout the scan. At high overpotentials, in a reductive RDE scan, the surface concentration of the oxidized species reaches zero, and the flux of mass transport of species to be oxidized, O , to the electrode surface approaches its maximum value. Thus, a limiting current is observed and is proportional to the square root of the angular velocity, as described by the Levich equation (Figure 2.3). A plot of i_{lc} versus ω should be linear with a slope that is a function of the number of electrons and diffusion

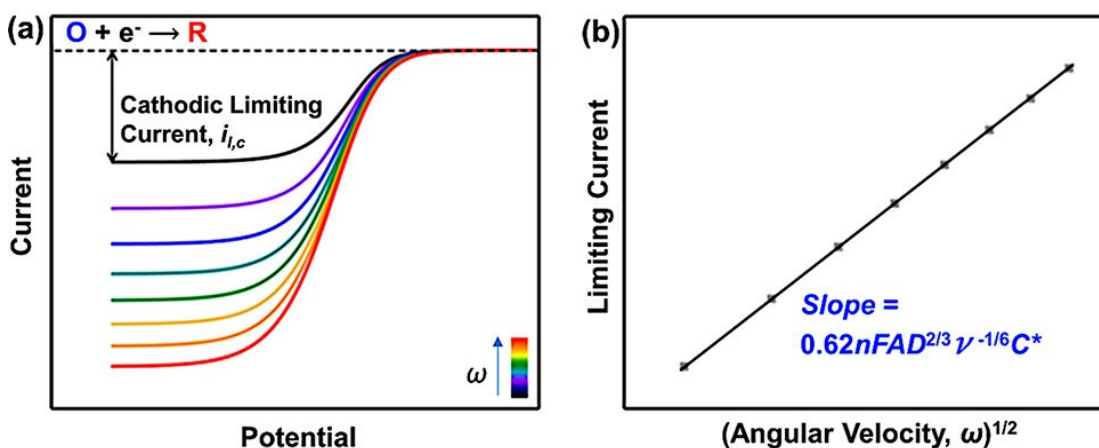
coefficient; a representative example of i_{lc} versus ω correlation can be seen in the work of Tong et al.^[12]

Table 2.1. List of Commonly Used Symbols^a

symbol	name	units	symbol	name	units
D	Diffusion coefficient	$\text{cm}^2 \text{s}^{-1}$	A	Electrode geometric area	cm^2
C^*	Bulk concentration	mol cm^{-3}	n	Number of electrons	none
ν	Scan rate	V/s	α	Charge-transfer coefficient	none
E	Measured cell potential	V	$E_{1/2}$	Half-wave potential	V
E_p	Peak potential	V	$E^{0'}$	Formal electrode potential	V
i	Electric current	A	i_p	Peak current	A
i_l	Limiting current	A	i_p	Kinetic current	A
ν	Kinematic viscosity	$\text{cm}^2 \text{s}^{-1}$	ω	Rotation rate or angular	rad s^{-1}
F	Faraday constant	C mol^{-1}	k^0	Standard rate constant	cm s^{-1}
R	Real gas constant	J K^{-1}	T	Temperature	K
E_{eq}	Equilibrium electrode	V	I_d	Diffusion limited current	A
ψ	Dimensionless Nicholson	none	r^0	Radius of an electrode	cm

^aNote the unusual units for C^* of mol cm^{-3} , which are employed for compatibility with electrode areas in cm^2 and k^0 in cm s^{-1} .

Rotating disk electrode (RDE) to determine the diffusion coefficient, D , for reversible, quasireversible, and irreversible redox systems



Levich-equation: Cathodic limiting current, $i_{l,c} = 0.62nFAD^{2/3}\nu^{-1/6}\omega^{1/2}C^*$, where ν is the kinematic viscosity of the fluid (measured in cm^2/s).

Figure 2.3. (a) Linear sweep voltammograms at different angular velocity. (b) Levich plot. Solving for D provides the diffusion coefficient for a quasireversible system (as well as reversible and irreversible systems). Reprinted with permission from reference 10. Copyright (2020) American Chemical Society.

2.2.3 Determination of Standard Rate Constant (k^0) Using Cyclic Voltammetry

The kinetics of redox reactions can be estimated from the standard rate constants. Low values of k^0 indicate sluggish kinetics that would require more energy (a larger overpotential to overcome), which is not ideal for high performance RFBs. Reversible electrochemical reactions are characterized by high rates of charge transfer (high standard rate constants, *e.g.*, $k^0 > 10^{-1} \text{ cm s}^{-1}$);^[146] k^0 values are lower for quasireversible systems, between 10^{-1} and $10^{-5} \text{ cm s}^{-1}$ and less than $10^{-5} \text{ cm s}^{-1}$ for irreversible systems.^[146]

The determination of the standard rate constants for reversible systems is challenging due to the high values of k^0 and the “kinetics are, in effect, transparent”, to quote Alan J. Bard.^[114] To determine the kinetic parameters for reversible systems, increasing the scan rate principally can render a reversible system quasireversible or irreversible; we have come across some examples in the literature applying and recommending this approach.^[115, 160-162] In principle, conventional voltammetry with electrodes having diameters of a few millimeters is limited in scan rate to $\sim 100 \text{ V/s}$ due to ohmic potential errors and a large capacitive current contribution, both of k^0 which increase with the scan rate. As a result, it has been difficult to measure values accurately above about 0.1 cm s^{-1} , and such fast-redox reactions have been considered “reversible”. However, the development of ultra-microelectrodes with diameters of 1–50 μm has reduced greatly the uncompensated resistance errors due to the much smaller currents, resulting small iR error.^[163-166] Thus, the useful range of voltammetric scan rates was increased to 1 MV/s, compared to the few hundred V/s limit with larger electrodes.^[164] With careful attention to cell design and sufficiently fast electronics, k^0 values of $\sim 3 \text{ cm s}^{-1}$ were determined for ferrocene on a 5 μm diameter Au electrode.^[167] A good test of the reliability of such high k^0 values is their constancy over a range of scan rates, which has been demonstrated for scan rates from 200 to 100,000 V/s.^[167] Microfabrication of very narrow band electrodes permits scan rates of $>1 \text{ MV/s}$,^[168] and electrochemical measurements on microdisk electrodes in the sub-microsecond time scale have become possible.^[167, 169, 170] Although microelectrodes are highly reliable with respect to the fast scan rate approach for reversible systems, further

validation is, nevertheless, recommended via simulation of the cyclic voltammograms. Thanks to the software available with modern potentiostats, most researchers can simulate their own cyclic voltammograms, similar to the ones shown in here.

For irreversible redox reactions, the standard rate constant can be determined by using the relationship between the peak current (i_p) and the overpotentials, represented in the difference between the peak potential (E_p) and the formal electrode potential ($E^{0'}$) different scan rates, as shown in the following equation:

$$\ln(i_p) = \ln(0.227FAk^0C^*) - \left(\frac{\alpha F}{RT}\right)(E_p - E^{0'}) \quad 2.3$$

provided that $E^{0'}$ is known. A linear plot of $\ln(i_p)$ versus $(E_p - E^{0'})$ at different scan rates should give a slope of $-\alpha F/nF$ and an intercept that is a function of the rate constant k^0 . A simulated example of an irreversible system is shown in Figure 2.4. An actual example of the determination of the rate constant for an irreversible system can be seen in the detailed work of Zeng and co-workers.^[171]

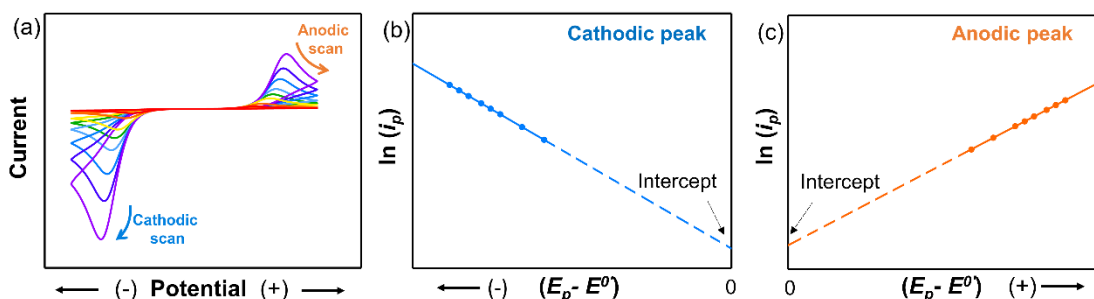


Figure 2.4. (a) Cyclic voltammetry for an irreversible system at different scan rates. (b,c) Plots for $\ln(i_p)$ versus $(E_p - E^{0'})$ for both cathodic and anodic peaks, provided that $E^{0'}$ is known for the studied system. Reprinted with permission from reference 10. Copyright (2020) American Chemical Society.

For more than five decades, the simplicity of Nicholson's method^[172] has rendered it the method of choice for the determination of standard rate constants for quasireversible systems. Nicholson showed that ΔE_p is a function of a dimensionless kinetic parameter (ψ) and is insensitive to the value of the charge-transfer coefficient, α , in the range of $0.3 < \alpha < 0.7$. The only requirements for using Nicholson's method are the measurement of ΔE_p at different scan rates, followed by determination of the corresponding values of ψ using Table 2.2. Thus, according to eq 2.4, k^0 can be extracted from the slope of a plot of ψ versus $v^{1/2}$. (Figure 2.5, and an example of this

method can be found in ref^[173]). Due to the discrete points in Table 2.2, for practical usage, eq 2.5 can be used to estimate the values of ψ at different peak separations.^[174]

$$\psi = \frac{(D_O/D_R)^{\alpha/2} k^0}{(\pi D_O n F v / RT)^{1/2}} \quad 2.4$$

$$\psi = \frac{(-0.6288 + 0.0021 \Delta E_p)}{1 - 0.017 \Delta E_p} \quad 2.5$$

A common source of errors when using the Nicholson equation is the uncompensated ohmic drop, which results in an increased peak separation with the scan rate and the determination of a lower rate constant than the true value. Hence, correction for the uncompensated ohmic drop is absolutely important for an accurate determination of the rate constant using the Nicholson equation. A good indicator of ohmic potential error is the variation of k^0 with scan rate, that is, the curvature of the plot in Figure 2.5. It is also recommended to validate the observed kinetic parameters by simulating the corresponding cyclic voltammograms at different scan rates and comparing them to the experimental voltammograms.

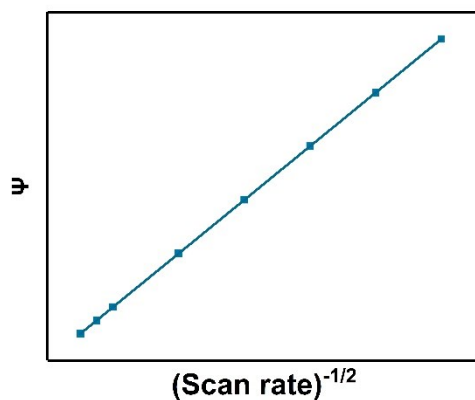


Figure 2.5. Example of the plot of ψ , determined by the peak separations (Table 2.2 or eq 2.5) of cyclic voltammograms observed at different scan rates versus the square root of the scan rates for quasireversible systems. Reprinted with permission from reference 10. Copyright (2020) American Chemical Society.

Table 2.2. Variation of ΔE_p with ψ at 25 °C for a One-Step and One-Electron Reaction, $\alpha = 0.5$, and Reverse Potential Greater than the Peak Potential by $112.5/n^a$

ψ	ΔE_p (mV)
20	61
7	63
6	64
5	65
4	66
3	68
2	72
1	84
0.75	92
0.50	105
0.35	121
0.25	141
0.10	212

^aData in the table are reproduced from ref 172.

2.3 Determining the Standard Rate Constant (k) Using a Rotating Disk Electrode

As described above, CV enables an estimate of the rate constant of your new redox couple. If it is promising and merits further investigation, RDE measurements will enable a “double check” of the rate constant and diffusion coefficient you determined above. The reader is directed to a useful recent tutorial describing the details and potential pitfalls of RDE.^[159] In redox reactions that are limited kinetically, the rate of charge transfer limits the measured current, thus, these are classified as irreversible reactions.^[146] In this case, the reciprocal of the measured current i^{-1} in the RDE steady-state voltammograms is the sum of the reciprocals of the kinetic i_k^{-1} and mass-transfer-limited i_l^{-1} current, according to the Koutecký–Levich equation below (eq 2.7). To minimize errors in the Koutecký–Levich analysis, the mass transfer correction for current data should be below 80% of the diffusion limited current.^[152, 155] As the RDE rotation speed is increased, the electrochemical response is less limited by mass transfer, and the measured current approaches the value of the kinetic current. Eq 2.6 is used for simulating RDE plots in Figure 2.6. In order to solve for i_k experimentally, the RDE must be run at different rotation rates, as shown in Figure 2.6a. Once these i – E plots are in hand, select different potentials on these i – E plots and determine the

measured current at different rotation velocities, ω . An example illustrated in Tables 2.3, and 2.4 lists the recommended range of potentials. A graph of $1/i$ versus $1/\omega^{1/2}$ should include several plots for the different chosen potentials, as shown in Figure 2.6b; each plot represents a set of data points for the measured current at different ω for a selected potential. In Figure 2.6b, the y -intercept of each plot (where $1/\omega^{1/2} = 0$) is the i_k^{-1} for this particular potential. At this point, you will have determined the i_k^{-1} values at different potentials. Next, using eq 2.8, the rate constant can be determined by simply plotting $\log(i_k)$ versus $(E - E^0)$ as shown in Figure 2.6c, analogous to Tafel plots. Specifically, the value of the y intercept of this linear plot is equal to $nFAk^0C^*$, which can be used to determine the rate constant. Furthermore, the slope is equal to $-anF/RT$, which can be used to determine the charge-transfer coefficient.

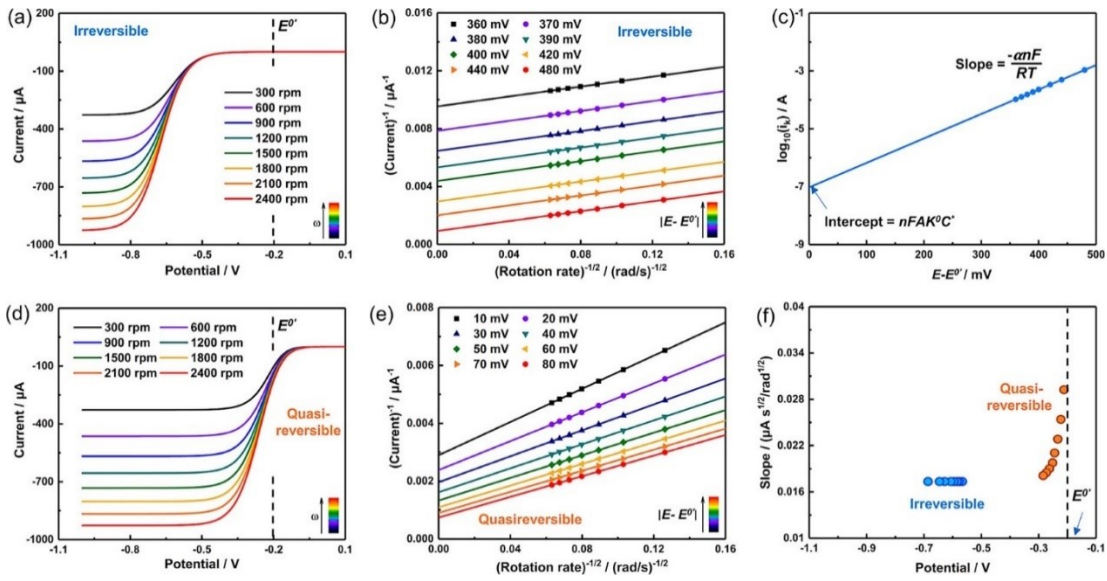


Figure 2.6. Simulated rotating disk electrode (RDE) scans at different rotation rates for irreversible (a) and quasireversible (d) systems. Koutecký–Levich plots for irreversible (b) and quasireversible (e) systems. (c) Plot of $\log(i_k)$ vs $E - E^0$ for the irreversible system. (f) Change of the slopes with overpotentials for the $i^{-1} - \omega^{-1/2}$ plots in (b, e). Simulated parameters for irreversible and quasireversible systems are listed in Table 2.3. Reprinted with permission from reference 10. Copyright (2020) American Chemical Society.

$$i = \left(1 - \frac{i}{i_{l,c}}\right) i_0 \exp\left(\frac{-\alpha F(E - E_{eq})}{RT}\right) - \left(1 - \frac{i}{i_{l,a}}\right) i_0 \exp\left(\frac{(1-\alpha)F(E - E_{eq})}{RT}\right) \quad 2.6$$

$$i_{l,c} = 0.62nFAD_0^{2/3} \nu^{-1/6} C_0^* \omega^{1/2}$$

$$i_{l,a} = 0.62nFAD_R^{2/3} \nu^{-1/6} C_R^* \omega^{1/2}$$

$$\frac{1}{i} = \frac{1}{i_k} + \frac{1}{i_{l,c}} = \frac{1}{i_k} + \frac{1}{0.62nFAD_0^{2/3} \omega^{1/2} \nu^{-1/6} C_0^*} \quad 2.7$$

$$i_k = nFAk_f C_O^* = nFAk^0 C_O^* \exp\left(\frac{-\alpha nF(E-E^{0'})}{RT}\right) \quad 2.8$$

Table 2.3. Simulated Parameters for Irreversible and Quasireversible Systems in Figure 2.6a and 2.6b

Parameter	Value
$\alpha\alpha\alpha$	0.5
C_0^* (mol cm ⁻³)	5×10^{-6}
C_R^* (mol cm ⁻³)	10^{-13}
D_0 & D_R (cm ² /s)	10^{-5}
Electrode area A (cm ²)	0.19625
Kinematic viscosity (cm ² /s)	0.01024
$E^{0'}$ (V)	-0.2
Irreversible rate constant k^0 (cm s ⁻¹)	1×10^{-6}
Quasireversible rate constant k^0 (cm s ⁻¹)	0.003

We noticed some examples in the literature that extracted kinetic information using a single voltammogram collected at one rotation speed to construct the log(current)–overpotential plot (similar to what is shown in Figure 2.6c). Ignoring corrections for the mass-transfer-limited current is justified in only a few specific examples in which there are high abundances of the reacting species, such as the hydrogen and oxygen evolution reactions (HER and OER).^[152, 175] For other systems, this approach will yield incorrect results. For more details, we refer the reader to the review article by Wei et al.^[152] For quasireversible systems, the same experimental procedures for irreversible systems can be applied, starting by collecting RDE plots at different rotation rates (Figure 2.6d) to construct the $i^{-1}-\omega^{-1/2}$ plots (Figure 2.6e). For quasireversible systems, the slopes for the $i^{-1}-\omega^{-1/2}$ plots vary with the overpotential (Figure 2.6e), which is not the case for irreversible systems (Figure 2.6b), which have identical slopes. For quasireversible systems, extracting information from the slope of the $i^{-1}-\omega^{-1/2}$ plots, the use of the Koutecký–Levich equation for irreversible systems is erroneous because of the dependence upon voltage.

Figure 2.6f shows the change of the slope of the $i^{-1}-\omega^{-1/2}$ plots versus the selected potentials for both irreversible and quasireversible systems. For irreversible systems, a plateau is observed, which shows the independence with regard to voltage, as substantiated by the Koutecký–Levich equation itself (eq 2.7); the slope is not a function of the overpotential. For quasireversible systems, however, a nonlinear curved plot is observed, indicating an exponential relationship. For experimental examples that show such changes of slope in the $i^{-1}-\omega^{-1/2}$ plots, we refer the reader to the detailed work by the research groups of Schubert, Aziz, Yu, McKone, and their co-workers.^[58, 67, 151, 176]

Table 2.4. Inverse Currents $1/i$ for Angular Velocities, ω (rpm) and Potentials (V) as Indicated Used to Construct the Koutecký–Levich Plot for an Irreversible System in Figure 2.6b

Potential (V)	300 rpm	600 rpm	900 rpm	1200 rpm	1500 rpm	1800 rpm	2100 rpm	2400 rpm
-0.56	-0.0125	-0.0116	-0.0112	-0.0110	-0.0110	-0.0107	-0.0106	-0.0106
-0.57	-0.0109	-0.0100	-0.0096	-0.0093	-0.0092	-0.0090	-0.0090	-0.0089
-0.58	-0.0095	-0.0086	-0.0082	-0.0079	-0.0078	-0.0077	-0.0076	-0.0075
-0.59	-0.0083	-0.0074	-0.0071	-0.0068	-0.0066	-0.0065	-0.0064	-0.0063
-0.6	-0.0074	-0.0065	-0.0061	-0.0059	-0.0057	-0.0057	-0.0055	-0.0054
-0.62	-0.0060	-0.0051	-0.0047	-0.0044	-0.0043	-0.0042	-0.0041	-0.0040
-0.64	-0.0050	-0.0041	-0.0038	-0.0035	-0.0033	-0.0032	-0.0031	-0.0030
-0.68	-0.0039	-0.0030	-0.0027	-0.0024	-0.0022	-0.0021	-0.0020	-0.0020

To solve this conundrum with regard to quasireversible systems, we provide the following solution. Instead of using the Koutecký–Levich equation (eq 2.7), which should only be used in the case of an irreversible system, we propose the use of eq 2.9 for mixed species of quasireversible-type systems as a starting point, and we modify it for a single species (only one species is dissolved in the solution, as is typically the case in RFBs). Equation 2.9 is the general equation for one-step and one-electron transfer quasireversible systems. This equation differs from the Koutecký–Levich equation (eq 2.7), as it is a function of the concentrations of both the oxidized and

reduced species overpotential ($E - E_{\text{eq}}$, where E_{eq} is the equilibrium potential) and the exchange current density (i_0). According to this general equation, a plot of (i^{-1}) versus $\omega^{-1/2}$ should be linear, with an intercept at ($\omega^{-1/2} = 0$) that is a function of i_0 and the term “ b ”; the plot will be similar to that shown in Figure 2.6e. In contrast to irreversible systems and the Koutecký–Levich equation (eq 2.7), the slope for quasireversible systems is a function of the overpotentials included in the term b (eq 2.11). Because this equation applies only to a solution of mixed species, and your solution most likely contains only one redox-active species in the catholyte or anolyte, it must be modified. In the term b in eq 2.11, substituting E_{eq} by the Nernst equation (eq 2.12) results in eq 2.13.

The general equation for a one-step and one-electron transfer quasireversible system is given by

$$\frac{1}{i} = \frac{b^\alpha}{1-b} \frac{1}{i_0} + \frac{1}{0.62FA\nu^{-1/6}} \frac{b^\alpha}{(1-b)} \left(\frac{b^{-\alpha}}{D_O^{2/3} C_O^*} + \frac{b^{1-\alpha}}{D_R^{2/3} C_R^*} \right) \frac{1}{\omega^{1/2}} \quad 2.1$$

which can be written as

$$\frac{1}{i} = B + \Delta \left(\frac{1}{\omega^{1/2}} \right) \quad 2.10$$

where F is the Faraday constant; A is the electrode area; ν is the kinematic viscosity; D_O and D_R are the bulk diffusion coefficients of the oxidized and reduced species, respectively; C_O^* and C_R^* are the bulk concentrations of the oxidized and reduced species, respectively; ω is the angular velocity of the electrode, and b is given by

$$b = \exp\left(\frac{F(E-E_{\text{eq}})}{RT}\right) \quad 2.11$$

where E is the measured cell potential and E_{eq} is given by

$$E_{\text{eq}} = E^{0'} + \frac{RT}{F} \ln\left(\frac{C_O^*}{C_R^*}\right) \quad 2.12$$

If we substitute eq 2.12 into eq 2.11, the following expression is obtained:

$$b = \frac{C_R^*}{C_O^*} \exp\left(\frac{F(E-E^{0'})}{RT}\right) \quad 2.13$$

Now, if we substitute eq 2.13 into the expression for Δ in eq 2.9, we arrive at the following expression

$$\Delta = \frac{1}{0.62FA\nu^{-1/6}} \left(\frac{1}{D_O^{2/3} C_O^* (1-b)} - \frac{1}{D_R^{2/3} C_R^* (1-b^{-1})} \right)$$

$$\Delta = \frac{1}{0.62FA\nu^{-1/6}} \left(\frac{1}{D_O^{2/3} \left(C_O^* - C_R^* \exp\left(\frac{F(E-E^{0'})}{RT}\right) \right)} - \frac{1}{D_R^{2/3} \left(C_R^* - C_O^* \exp\left(-\frac{F(E-E^{0'})}{RT}\right) \right)} \right) \quad 2.14$$

In the limiting case of a single species solution where $C_0^* \gg C_R^*$, we obtain the following expression:

$$\lim_{C_R^* \rightarrow 0} \Delta = \frac{1}{0.62FA\nu^{-1/6}C_0^*} \left(D_0^{-2/3} + D_R^{-2/3} \exp\left(\frac{F(E-E^{0'})}{RT}\right) \right) \quad 2.15$$

Conversely, if we have the opposite case where $C_R^* \gg C_0^*$,

$$\lim_{C_0^* \rightarrow 0} \Delta = -\frac{1}{0.62FA\nu^{-1/6}C_R^*} \left(D_0^{-2/3} \exp\left(\frac{-F(E-E^{0'})}{RT}\right) + D_R^{-2/3} \right) \quad 2.16$$

At this point, we have a full picture. Assuming that the concentration of R is 0, $C_R^* \rightarrow 0$, only the oxidized species O exists in the solution. In this case, the slope of a plot of $(i)^{-1}$ versus $\omega^{-1/2}$ (Figure 2.6e), represented by eq 2.9, can be simplified to eq 2.15, which shows an exponential dependence of the slope on the overpotentials, as seen in

Figure 2.6f for quasireversible systems. Interestingly, a plot of the slope versus $e^{(F/RT)(E-E^{0'})}$ should be linear, as shown in Figure 2.7. The intercept is a function of the diffusion coefficient of the oxidized species, D_0 , and a slope that is a function of diffusion coefficient of D_R of the newly formed reduced species, R .

By convention, the intercept of the plot of $(i)^{-1}$ versus $\omega^{-1/2}$ (Figure 2.6e) for a quasireversible system and eq 2.9 will be denoted as (eq 2.17):

$$i_{quasi} = \frac{(1-b)i_0}{b\alpha} \quad 2.17$$

$$i_0 = FAK^0 C_0^* \exp\left(\frac{-\alpha F(E_{eq} - E^{0'})}{RT}\right) \quad 2.18$$

Substituting eq 2.18 to eq 2.17 results in

$$\begin{aligned} i_{quasi} &= (1-b) \frac{FAK^0 C_0^* \exp\left(\frac{-\alpha F(E_{eq} - E^{0'})}{RT}\right)}{\exp\left(\frac{\alpha F(E - E_{eq})}{RT}\right)} \\ \Rightarrow i_{quasi} &= (1-b)FAK^0 C_0^* \exp\left(\frac{-\alpha F(E - E^{0'})}{RT}\right) \end{aligned} \quad 2.19$$

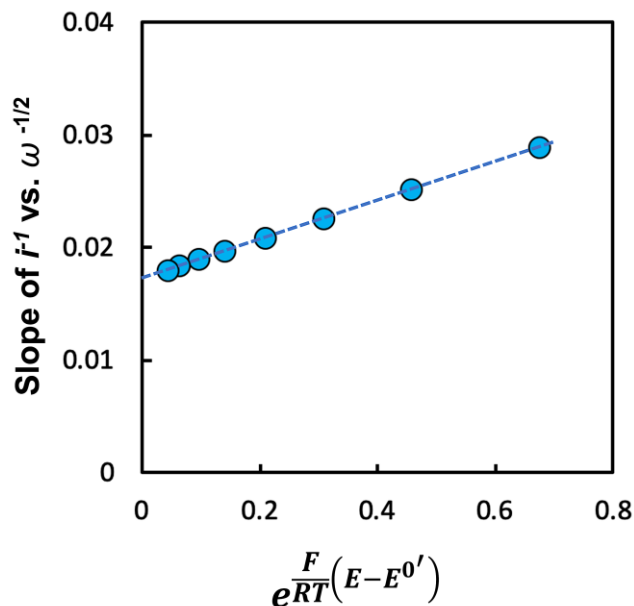


Figure 2.7. Plot the slope of the i^{-1} vs. $\omega^{-1/2}$ plots for quasireversible system (Figure 2.6e) vs. $e^{-\frac{F}{RT}(E-E^{0'})}$. Reprinted with permission from reference 10. Copyright (2020) American Chemical Society.

Considering the Nernst equation for a solution of only the oxidized species, O , $C_R^* \rightarrow 0$, we can assume that E_{eq} is very large so that the term “ b ” approaches 0, thus, eq 2.19 can be simplified to eq 2.20. Therefore, the intercept for quasireversible systems of a single species is similar to the kinetic current for irreversible systems (eq 2.8). At this point, solving for the standard rate constant for quasireversible systems should follow the same procedures shown earlier for irreversible systems (Figure 2.6c and eq 2.20). Furthermore, sampled current voltammetry (SCV) would act as double-check technique for solutions of single quasireversible species.

$$i_{\text{quasi}} = F A k^0 C_O^* \exp\left(\frac{-\alpha F (E - E^{0'})}{RT}\right) = i_k \quad 2.20$$

SCV is a potential–relaxation technique that results in sigmoidal current–voltage plots for the three kinetic regimes, reversible, quasireversible, and irreversible. Examples of accessible parameters from the wave height (i_d) are the number of electrons (n), diffusion coefficient (D) bulk concentration, and electrode area (A). For quasireversible and irreversible systems, SCV also can provide information on kinetic parameters, such as k^0 and α , *vide infra*. In SCV, a series of step potentials, from the rest potential ($E_{\text{appl.}} < E^{0'}$) to the desired potential ($E_{\text{appl.}} > E^{0'}$) should be applied. For

each of the selected step potentials, the current should decay with time and recorded at a fixed decay time ($t = \tau$), Figure 2.8. A sigmoidal current–potential plot is thus obtained. At high potentials ($E_{\text{appl.}} > E^{0'}$), rapid depletion of the analyte at the electrode surface occurs, and the process would be controlled by only the diffusion of the analyte to the electrode, thus, the solution has to be unstirred. In this case, the measured current is the diffusion-limited current (i_d), and the Cottrel Equation 2.21 applies.

$$i_d = \frac{nFAD^{1/2}C^*}{\pi^{1/2}t^{1/2}} \quad 2.21$$

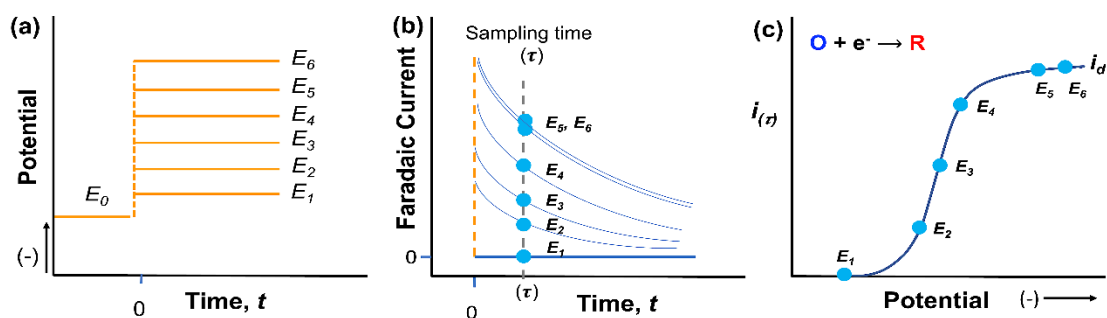


Figure 2.8. Sampled current voltammetry procedures. (a) Potential step experiments at different increasing reducing potentials. (b) Current–time decay for each of the applied potential steps and illustrates the sampling time (same for all potential steps). (c) Sampled current voltammogram. Reprinted with permission from reference 10. Copyright (2020) American Chemical Society.

For solutions in which only one single species exists (either oxidized or reduced species, O or R, respectively), Equation 2.9 represents the dependence of the current, in SCV, on the applied potential and time for reversible, quasireversible, and irreversible systems, Figure 2.9. Please note that the function $F_1(\lambda)$ approaches unity for reversible systems, resulting in Equation 2.23. For irreversible systems, however, $K_b/K_f = \Theta = 0$, thus Equation 2.22 is simplified to Equation 2.24.

$$i = \frac{i_d}{(1+\xi\theta)} F_1(\lambda)$$

Where $\xi = \left(\frac{D_O}{D_R}\right)^{1/2}$; $\theta = \exp\left(\frac{nF(E-E^{0'})}{RT}\right)$;

$$F_1(\lambda) = \pi^{1/2}\lambda \exp(\lambda^2) \operatorname{erfc}(\lambda); \quad 2.22$$

$$\lambda = Ht^{1/2} = \frac{k_f t^{1/2}}{D_O^{1/2}} (1 + \xi\theta);$$

$$k_f = k_0 \exp\left(\frac{-\alpha F(E-E^{0'})}{RT}\right)$$

For a reversible system:

$$i = \frac{i_d}{(1+\xi\theta)} \quad 2.23$$

For an irreversible system:

$$\frac{i}{i_d} = F_1(\lambda) = \pi^{\frac{1}{2}}\lambda \exp(\lambda^2) \operatorname{erfc}(\lambda) \quad 2.24$$

where λ for irreversible systems equals $k_f t_{1/2} / D^{1/2}$.

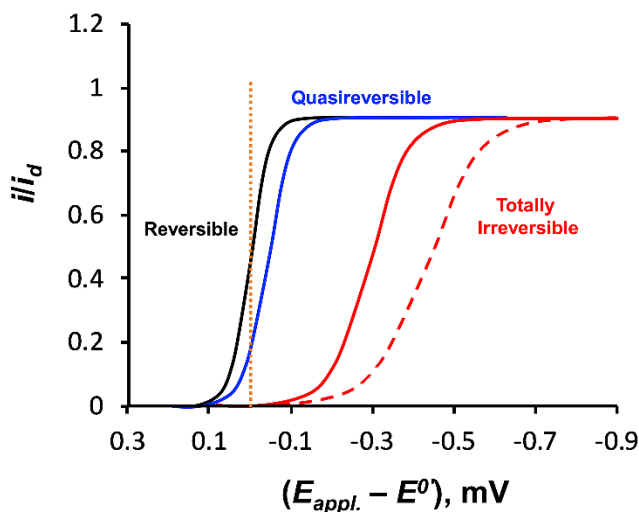


Figure 2.9. Examples of sampled current voltammetry for the three different kinetics regimes. Reprinted with permission from reference 10. Copyright (2020) American Chemical Society.

For quasireversible systems, the kinetics parameters (k^0 and α) can be determined by fitting the experimental plot of i/i_d versus $(E_{\text{appl.}} - E^0)$ to the theoretical function in Equation 2.22. The fitting can be done by employing a nonlinear least-squares fitting algorithm, such as the Levenberg–Marquardt. An example of curve fitting for SCV can be found in the published work by Friedl et al.^[109]

In potential step experiments, the charging (non-faradaic) current contributes to the faradaic current during a period of about five times the cell time constant ($R_u C_d$), where R_u is the uncompensated resistance and C_d is the double layer capacitance.^[114] Thus, the sampling time has to be larger than $R_u C_d$. Using ultramicroelectrodes (UME), one can minimize the cell time constant ($R_u C_d$). Fitting and analysis of the steady-state voltammograms observed using UME for quasireversible systems can be done with

Equation 2.25. The second method for extracting the kinetic parameters for quasireversible systems involves comparing the differences $(E_{1/4} - E_{1/2})$ and $(E_{3/4} - E_{1/4})$ from the steady-state voltammograms observed using UME to the tables published by Mirkin and Bard for these differences and the corresponding sets of k^0 and α , where $E_{1/4}$, $E_{1/2}$, and $E_{3/4}$ are the potentials at $i = 1/4$, $1/2$, and $3/4 i_d$, respectively.^[177]

$$i = \frac{FAD_0C_0^*}{r_0} \left[\frac{\kappa}{1 + \kappa(1 + \xi^2\theta)} \right] \quad 2.25$$

where r_0 is the radius of the UME and $\kappa = r_0k_f/D$.

For irreversible systems, similar to quasireversible systems, fitting SCV or the steady-state voltammograms using Equation 2.24 and Equation 2.26, respectively, can allow for the determination of k^0 and α . There are two other alternative methods for determining k^0 and α for irreversible systems. The first method involves calculating α from the slope of E versus $\log(i_d - i)/i$ for the steady-state voltammograms according to Equation 2.27. The intercept at $E^{0'}$ can provide the k^0 value, provided that (r_0/D) is known. The second method is based on Tomes' criterion, as shown in Table 2.5, the difference $(E_{3/4} - E_{1/4})$ for totally irreversible systems can provide α directly, where $(E_{3/4} - E_{1/4}) = 45.0/\alpha$ and $59.1/\alpha$ for linear diffusion at planar electrodes and steady-state voltammograms at UME, respectively. Once α is determined, k^0 can be calculated from Equation 2.28 from the half-wave potential ($E_{1/2}$) provided that $E^{0'}$ is known. For reversible systems, the number of electrons can be extracted either from the slope of the sigmoidal wave or from the Tomes' criterion as shown in Table 2.5.

$$\frac{i}{i_d} = \frac{\kappa}{1 + \kappa} \quad 2.26$$

by substituting for κ and $k_f = k^0 \exp(-\alpha F/RT)(E - E^{0'})$, one obtains the potential-current Equation 2.27

$$E = E^{0'} + \frac{RT}{\alpha F} \ln \left(\frac{r_0 k^0}{D} \right) + \frac{RT}{\alpha F} \ln \left(\frac{i_d - i}{i} \right) \quad 2.27$$

where half-wave potential,

$$E_{1/2} = E^{0'} + \frac{RT}{\alpha F} \ln \left(\frac{r_0 k^0}{D} \right) \quad 2.28$$

Table 2.5. Characteristics for the Current–potential Wave Observed in Sampled Current Voltammetry Plots of E Versus $\text{Log}(i_d - i)/i$ at 25 °C. *Using Ultramicroelectrodes (UME), Electrodes of Radii Less Than 25 μm . This Table was Adapted from the Textbook of A. J. Bard.^[114]

Kinetic Regime	Linear diffusion at planar electrodes		Steady-state*	
	Slope (mV)	$E_{3/4} - E_{1/4}$ (mV)	Slope (mV)	$E_{3/4} - E_{1/4}$ (mV)
Reversible ($n \geq 1$)	Linear, $59.1/n$	$56.4/n$	Linear, $59.1/n$	$56.4/n$
Quasireversible ($n = 1$)	Slightly nonlinear	Between 56.4 and $45.0/\alpha$	Nonlinear	Between 56.4 and $56.4/\alpha$
Irreversible ($n = 1$)	Slightly nonlinear	$45.0/\alpha$	Linear, $59.1/\alpha$	$56.4/\alpha$

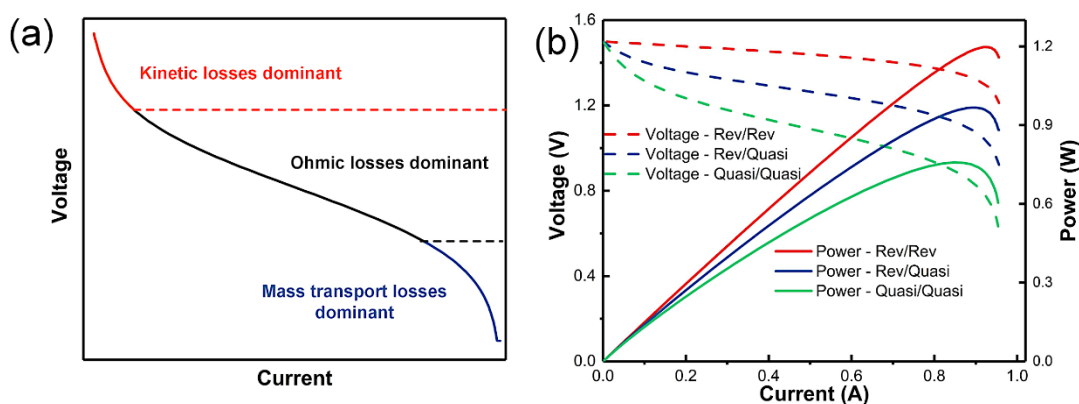


Figure 2.10. (a) A discharging polarization curve for a redox flow battery (RFB) device, illustrating three voltage regions that are associated with kinetics, ohmic, and mass-transfer losses. (b) Simulated discharge polarization and corresponding power curves at 50% state of charge (equal concentrations for the O and R species) for three RFBs of different combinations of reversible and quasireversible redox systems with k^0 of $3 \times 10^{-1} \text{ cm s}^{-1}$ and $2 \times 10^{-4} \text{ cm s}^{-1}$, respectively. Reprinted with permission from reference 10. Copyright (2020) American Chemical Society.

As a final point to note, the cell voltage is a crucial parameter inherent in the power and energy density values for RFBs, both of which contribute to the overall cell cost.^[22] Polarization curves typically are performed to determine the sources of voltage loss in RFBs,^[178] and power density curves, derived from polarization curves, commonly are used to give an idea about the maximum delivered power at different current densities and rates. As shown in Figure 2.10a, the polarization curve can be divided into three voltage regions, which are controlled by the kinetics of the redox systems, ohmic cell resistance associated with contact and ionic resistances, and mass transport of bulk species to the electrode surface.^[179] For the effect of the mass transport and ohmic resistance on the polarization curves, we refer to the detailed work by Aaron et al. and Milshtein et al.^[179, 180] In order to demonstrate the effect of kinetics on the polarization and power curves, we used the current–overpotential (equation 2.6)^[114]

to simulate the polarization curves for RFBs, including reversible (k^0 of $3 \times 10^{-1} \text{ cm s}^{-1}$) and quasireversible (k^0 of $2 \times 10^{-4} \text{ cm}$) redox species. Figure 2.10b shows the discharging polarization and corresponding power curves at 50% state of charge for three RFBs with different combinations of reversible and quasireversible redox couples. The incorporation of quasireversible redox couples in a symmetric RFB configuration (green plots in Figure 2.10b) shows the lowest power at high current values, which has the highest voltage drop in the kinetic region of the polarization curve compared to a symmetric RFB composed of facile redox couples (red plots), and an asymmetric RFB incorporating reversible and quasireversible redox couples (blue plots). Thus, there is clear evidence for the impact of sluggish kinetics and low-rate-constant redox systems on the delivered maximum power and overall energy densities represented by the cell voltage.

2.4 Conclusions

Redox flow batteries are, at least on paper, experimentally simple electrochemical energy storage devices. Compartmentalized anolyte and catholytes, each containing the respective redox species, are separated only by an ion-exchange membrane. The performance of the RFB, however, depends exquisitely upon the nature and kinetic parameters of the electrochemically active species that must be determined accurately in order to understand the fundamental mechanisms of the redox chemistry. We have provided this step-by-step description of how to categorize the redox species within an RFB as reversible, quasireversible, or irreversible, and offered a new way to obtain the electrochemical kinetics parameters easily. Then, we simulated the performance of RFBs from polarization curves based on different kinetic systems, which path a way to determine the critical kinetic information needed to understand the basics of your RFB system.

Chapter 3

Water-soluble pH-switchable Cobalt Complexes for Aqueous Symmetric Redox Flow Batteries[†]

3.1 Introduction

Metal ion-only aqueous RFBs have been known for 70 years,^[3] but metal ion systems usually are challenged by high crossover due to the small ionic radii of the redox-active species^[31, 181] and, if they rely upon a M(0) oxidation state, are susceptible to metal dendrite formation.^[51] Redox-active species comprising coordination complexes or organic compounds offer the ability to tailor their properties, such as redox potentials, solubility, and kinetics, while affording chemical and electrochemical stability through chemical modification and functionalization.^[3, 70, 182] The solvent in which the redox active species are dissolved is also an important consideration, and aqueous RFBs are of particular interest due to the high conductivity, non-flammability, low toxicity, and low cost of water-based electrolytes.^[31]

Typically, RFBs are asymmetrical; the anolyte and catholyte comprise two different chemical species, physically separated by a membrane. A symmetric RFB would require only a single redox-active material that has at least three stable oxidation states;^[32] such an architecture would eliminate cross-contamination due to crossover of the redox-active species in asymmetric configurations, thus, facilitating long-term cyclability and potentially simplifying deployment.^[76, 183]

Most symmetric RFBs have been developed for non-aqueous systems for reasons of solubility of organic components and a wider potential window in which to operate.^[109, 184-188] For aqueous symmetric RFBs, the three stable oxidation states need to be accessible within the potential window for the hydrogen and oxygen evolution reactions. A number of interesting approaches to the development of aqueous symmetric RFBs have been pursued, including the investigation of heteropolyacids (polyoxometalates, POMs), metal coordination complexes, and combi-molecules comprising tethered anolyte–catholyte combinations.^[189-191] The current champion is a tungsten–cobalt POM, $H_6[CoW_{12}O_{40}]$, which in water has two two-electron waves at –

0.191 V and -0.074 vs NHE, a one-electron wave at 1.103 vs NHE, and is stable for 30 cycles.^[108] An elegant study of a triazametallocycle iron complex with pH-dependent oxidation states has demonstrated applicability as a catholyte at low pH and anolyte at high pH; thus, it could serve as a symmetrical aqueous RFB, albeit with different pH values on opposite sides of the membrane.^[192] Combi-molecules, by covalently binding to ‘catholyte’ and ‘anolyte’ together, also are introduced in aqueous RFBs to achieve a symmetric design.^[190, 191] However, similar to mixing redox species together, this design will scarify half of the redox-active species, decrease solubility, increase viscosity, and pose a high stability requirement if no degradation happens in the voltage window.^[32]

Bis(imino)pyridine ligand binding cobalt has proved to have excellent catalytic performance in non-aqueous systems^[193-195] (@Schmidt2015, @Friedfeld2016, @Krautwald2017). Their low toxicity, low cost, and chelating nature help to stabilize metal complexes and renders them promising members for redox flow battery chemistry. In this work we explore the properties and utility of a water-soluble version of a bis(pyridine-2,6-diimine) cobalt(II) complex for aqueous symmetric RFB applications (Figure 3.1). Four carboxylic acid groups were installed around the periphery of a 2,6-bis[1-(phenylimino)ethyl]pyridine framework to render it water soluble, particularly when these groups are deprotonated and, therefore, negatively charged. The electrochemistry of cobalt complexes with neutral meridionally coordinated pyridine-2,6-diimine ligands is rich and has been studied since 1977.^[196, 197] The well-established electrochemical profiles of cobalt complexes were harnessed for RFB applications,^[59, 60, 135, 176, 198-201] including three symmetric non-aqueous RFB systems.^[137, 202, 203] Here, we examine the aqueous electrochemistry of the water-soluble version and determine the influence of pH on the two Co(I,II,III) redox couples as the basis of a symmetric, aqueous RFB.

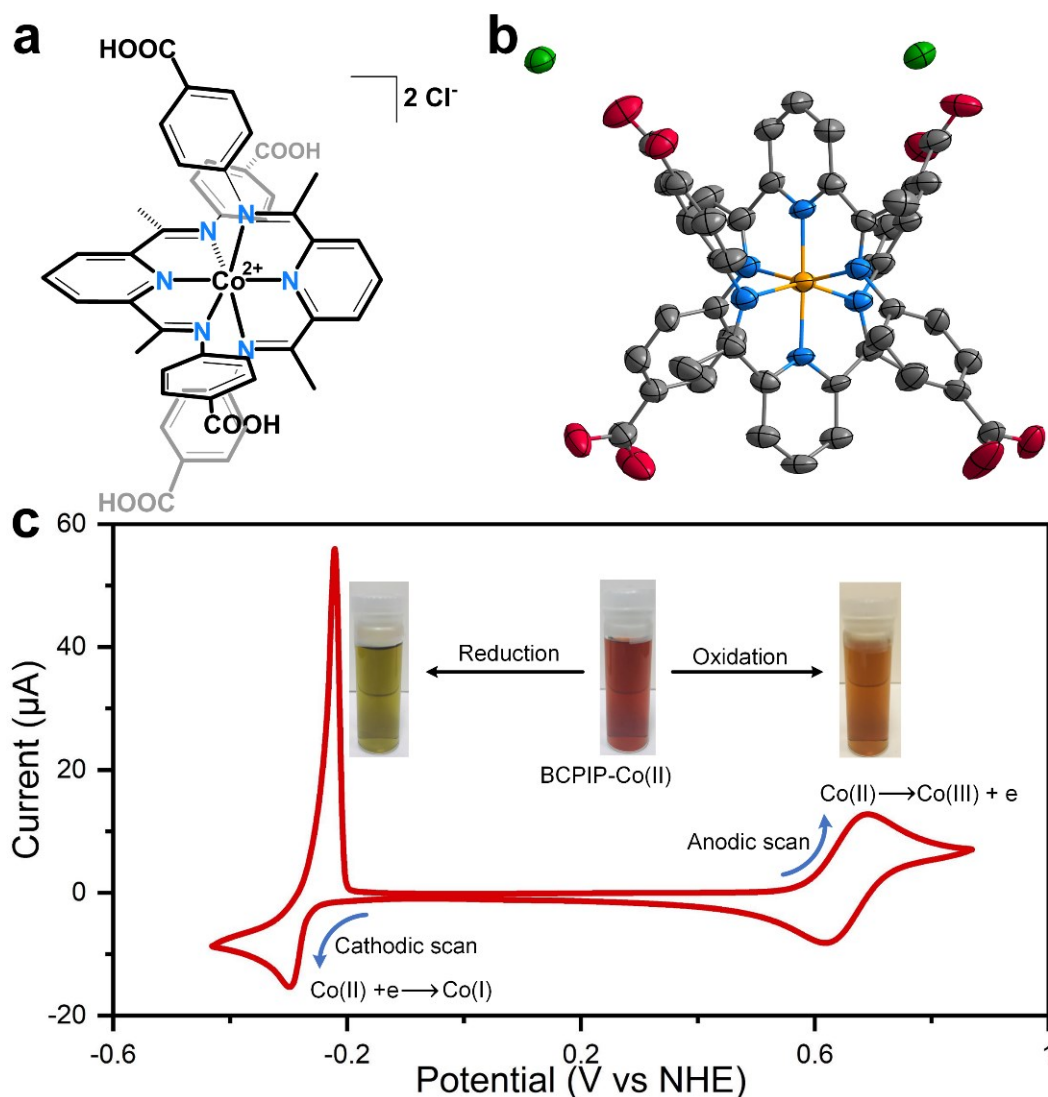


Figure 3.1. (a) Fully protonated BCPIP-Co(II) complex. (b) Thermal ellipsoid plot of BCPIP-Co(II) chloride, obtained from single-crystal X-ray diffraction. Cobalt is shown in yellow, carbon in gray, nitrogen in blue, oxygen in red, and chloride in green. Atoms are represented by ellipsoids at the 50% probability level, and hydrogen atoms and solvent have been omitted for clarity. (c) CV curves of 2 mM BCPIP-Co in 0.5 M NaCl at pH 3.0 acquired at a scan rate of 50 mV/s. Reproduced from reference 61. Copyright (2020) Royal Society of Chemistry.

3.2 Results and Discussion

The newly synthesized 4-carboxy-substituted tridentate ligand, 2,6-bis[1-(4-carboxyphenylimino)ethyl]pyridine, termed BCPIP, was coordinated with cobalt(II) chloride to yield BCPIP-Co(II) chloride, which was characterized structurally (Figure 3.1a and Figure 3.2). As shown in the figure below, the synthesis of bis(imino)pyridine pincer ligand is a Schiff condensation reaction of diacetylpyridine with aniline, with a

yield of 93% (See details in Experimental section.). Through the incorporation of the four carboxylic acid groups in the complex, the overall charge of the complex can be tuned from cationic to neutral to anionic through control of pH. As will be demonstrated, this complex has stable and electrochemically accessible Co(I), Co(II), and Co(III) oxidation states that fall within the window of oxygen and hydrogen evolution reactions, enabling assembly and testing of symmetric aqueous RFBs.

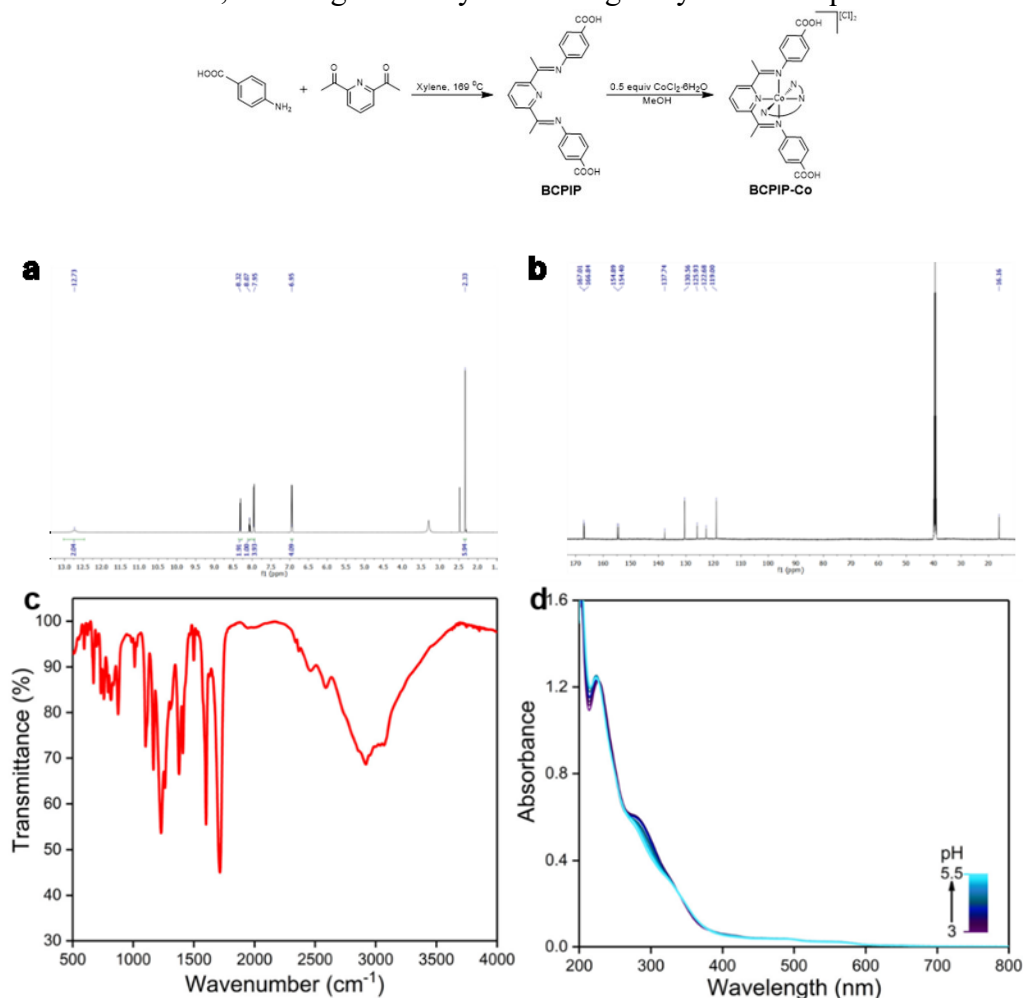


Figure 3.2. (a) ^1H NMR spectrum of the ligand, BCPIP (DMSO- d_6 , 27 °C). (b) ^{13}C NMR spectrum of the ligand, BCPIP (DMSO- d_6 , 27 °C). (c) Transmission mode FTIR spectra of BCPIP-Co(II) on a native oxide-capped silicon wafer. Features at 1600 and 1575 cm^{-1} correspond to pyridyl and aryl-ring breathing mode deformations. (d) UV spectra of BCPIP-Co(II) at different pH values (0.02 mM) using NaOH (aq) to adjust pH. Reproduced from reference 61. Copyright (2020) Royal Society of Chemistry.

The solid-state structure of BCPIP-Co(II) was examined by single-crystal X-ray diffraction and, as expected, revealed a central octahedral cobalt ion with mean Co–N distances in the range of 1.9 to 2.1 Å (Figure 3.1b). The BCPIP-Co(II) has a solution

magnetic moment of $2.44 \mu_B$ at 27°C , which is consistent with a low spin d^7 complex with $S=1/2$, as determined by the Evans method.^[204] Figure 3.1c shows the cyclic voltammograms for the anodic and cathodic events, E^0 values of 0.65 V and -0.28 V vs NHE, respectively, of the BCPIP-Co(II) complex in 0.5 M NaCl (aq) . Based on previous studies of similar bis(imino)pyridine cobalt compounds, the anodic and cathodic events are assigned as metal-centered redox reactions, Co(II)/Co(III) and Co(I)/Co(II), respectively.^[197,205] To investigate the effect of pH on the electrochemical behaviour of BCPIP-Co(II), cyclic voltammetry (CV) was carried out in the range of pH 1.5 to 5.5 for both the Co(II)/Co(III) and Co(I)/Co(II) couples (Figure 3.3). As shown in Figure 3.3a, increasing the pH results in a shift to increasingly negative potentials for both the Co(II)/Co(III) anodic and cathodic peak potentials. When $E_{1/2}$ is plotted versus pH, Figure 3.3c, the $E_{1/2}$ of the BCPIP-Co(II-III) drops to lower potentials, following a sigmoidal trend that corresponds to a potentiometric titration of the four carboxylic acid groups of the complex.

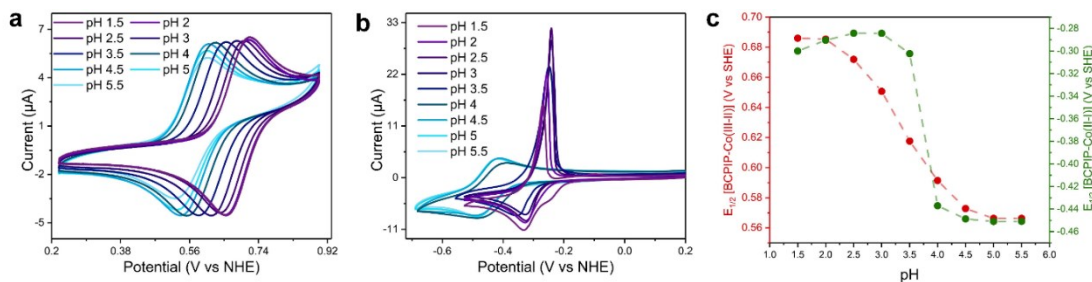


Figure 3.3. CV for the Co(II)/Co(III) (a) and Co(I)/Co(II) (b) redox reactions as a function of pH in 2 mM of BCPIP-Co(II) and 0.5 M NaCl (aq) at 50 mV/s. (c) Average redox peak potentials, $E_{1/2}$, of BCPIP-Co redox pairs vs pH. $E_{1/2} = (\text{anodic peak potential} + \text{cathodic peak potential})/2$. Reproduced from reference 61. Copyright (2020) Royal Society of Chemistry.

A different CV profile is observed for the Co(II)/Co(I) couple in the range of pH 1.5 to 5.5 (Figure 3.3b). The sharp anodic feature at -0.25 V vs NHE is indicative of a weak interaction between the BCPIP-Co(I) complex and the surface of the glassy carbon electrode. As the pH is raised from 3.5 to 4.0, a change of the CV profile is observed that is reversible with pH (Figure 3.4), accompanied by the collapse of the sharp feature at -0.25 V and the appearance of a ‘duck-shaped’ curve with an anodic peak at a more negative potential, -0.39 V . The plot of $E_{1/2}$ versus pH for the BCPIP-Co(II-I) couple (Figure 3.3c) reflects the abrupt change in the range of pH 3.5 to 4.0

and the levelling off at pH 4.5, which corresponds to the $E_{1/2}$ of the fully deprotonated BCPIP-Co(I) complex (all 4 carboxylic acid groups ionized to carboxylates).

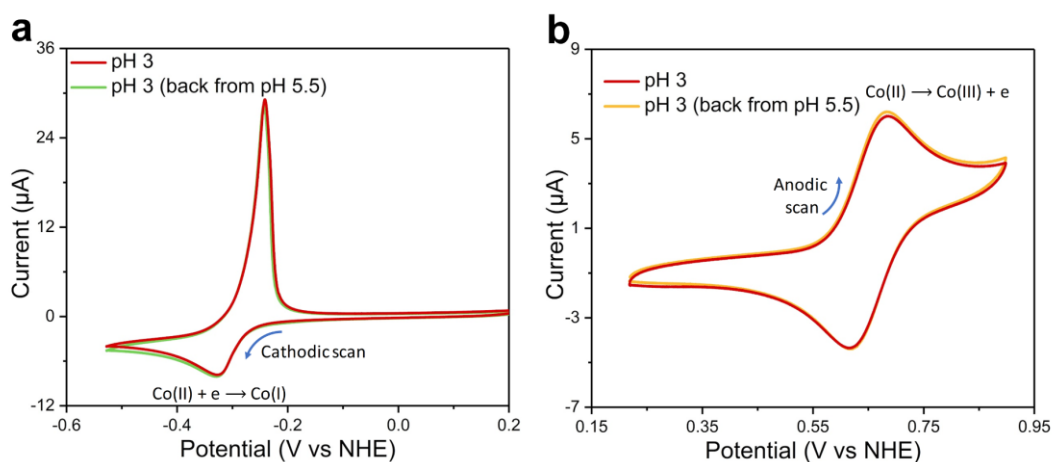


Figure 3.4. CV of 1 mM of BCPIP-Co(II) on a glassy carbon electrode in 0.5 M NaCl (aq) at pH 3.0, after increasing the pH to 5.5, and then lowering it back to pH 3.0. (a) Cathodic event [Co(II/I)] for the BCPIP-Co(II) redox reactions. (b) Anodic event [Co(II/III)] for the BCPIP-Co(II) redox reactions. Reproduced from reference 61. Copyright (2020) Royal Society of Chemistry. (See experimental details in the Experimental Section, Reversibility.)

A full representation of the species present in solution over a pH a range of 1.5 to 5.5 for the Co(I), Co(II), and Co(III) species is shown in Figure 3.5. Due to the four carboxylic acid groups, the complexes are highly sensitive to pH within this range. Thus, depending upon the oxidation state of the cobalt center, the overall charges of complexes vary from +3 to -3. The ligand basicity also would be expected to change, depending upon the protonation/deprotonation of these groups, with the deprotonated ligand being more electron-donating. Using this scheme, a clearer understanding of the CV curves for the BCPIP-Co(II-III) and BCPIP-Co(I-II) couples can be elucidated. For the BCPIP-Co(II-III) couple (Figure 3.3a, c) the shift to a more negative potential results from the deprotonation of the carboxylic groups and the accompanying change of the overall charge of the population of BCPIP-Co(II) species from +2 to -2 (Figure 3.5, middle row). The energy barrier required to overcome oxidation is lowered at pH > 4 due to the higher Lewis basicity of the deprotonated ligands towards the cobalt metal center and overall negative charge of the complex.

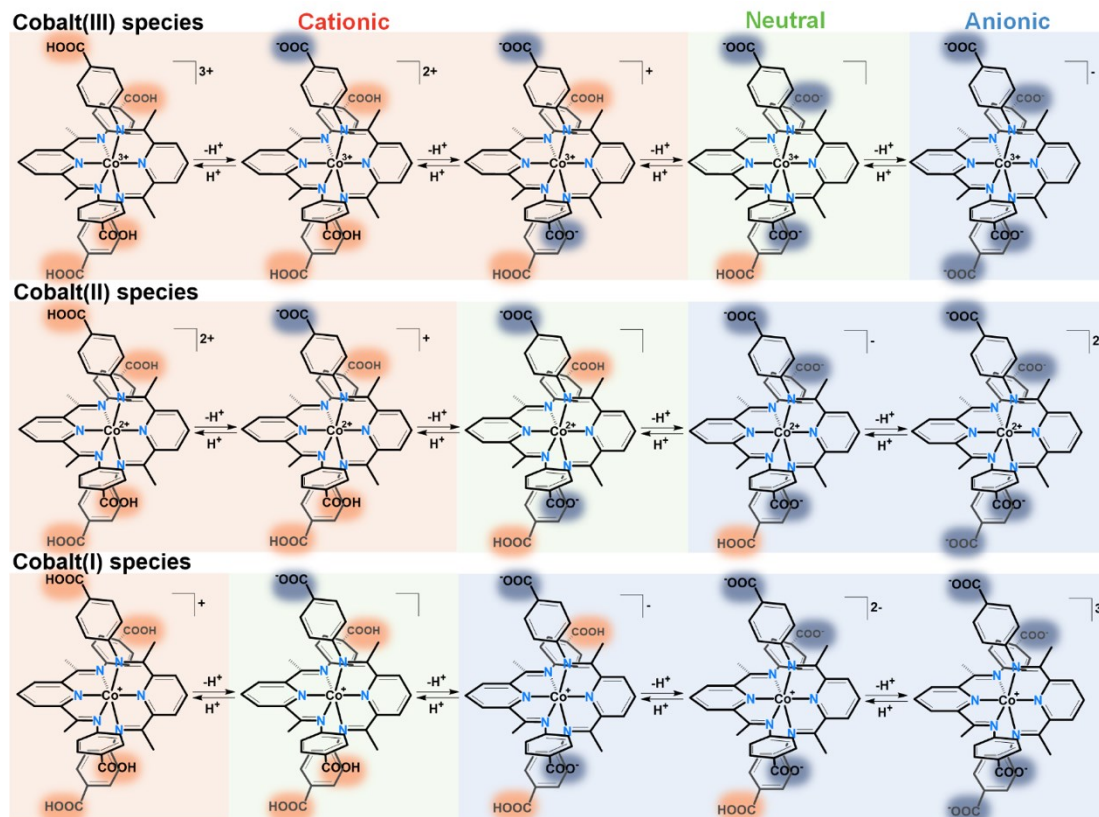


Figure 3.5. Speciation of different BCPIP-Co(*n*) species in their sequential deprotonated forms, where *n* = I, II, or III, spanning the pH range of 1.5 to 5.5 (Highlights of -COOH groups: orange = protonated; blue = deprotonated). Reproduced from reference 61. Copyright (2020) Royal Society of Chemistry.

The Co(II)/Co(I) redox couple (Figure 3.3b, c) is similar to that of Co(II)/Co(III), as it also demonstrates a shift to more negative potentials upon increasing the pH. The sharp peak at -0.25 V vs NHE corresponds to the plateau on the left-hand side of the sigmoidal plot in Figure 3.3c at pH levels less than 3.5. The sharp anodic current signal indicates a weak interaction between the electrode surface and Co(I).^[114] In this lower pH range, the population of BCPIP-Co(I) species present in solution would be expected to have net overall charges of +1 and 0, as anionic species would only appear at $\text{pH} > 3.5$, assuming that the dramatic drop of $E_{1/2}$ in Figure 3.3c results from deprotonation of the four carboxylic acid groups (Figure 3.5, bottom row). The neutral BCPIP-Co(I) complex would be expected to be less soluble than the more charged species (see Table 3.1), enabling weak binding to the glassy carbon electrode through hydrogen bonding interactions, thanks to the three -COOH groups on the BCPIP-Co(I) complex and the oxygen-based hydrogen bond donors and acceptors on

the glassy carbon electrode; the surface of glassy carbon electrodes typically comprises 8–15% oxygen (relative to carbon), representing a variety of oxygen-containing functional groups that could participate in such weak bonding scenarios.^[206, 207] Upon further increase of the pH of the solution, the carboxylic acid groups on the BCPIP-Co(I) complex become deprotonated, rendering the complex negatively charged (Figure 3.5, bottom row). The weak hydrogen-bonding interaction between the BCPIP-Co(I) and the electrode is rendered disfavorable, liberating the complex to solution.

Table 3.1. Solubility of BCPIP-Co(II) Complex at Different pH Values, Corresponding to the Subsequent Neutralization of the Four Carboxylic Groups

pH	Solubility
1.9 (no addition of NaOH)	0.28 M
2.8 [one equivalent of NaOH/ BCPIP-Co(II)]	0.08 M
4.0 [two equivalents of NaOH/ BCPIP-Co(II)]	0.04 M
5.0 [3 equivalents of NaOH/ BCPIP-Co(II)]	0.18 M
6.3 [4 equivalents of NaOH/ BCPIP-Co(II)]	> 0.5 M (solution becomes very viscous and thus an upper limit could not be determined)

To investigate the electrochemical kinetics of the BCPIP-Co(II) complex, both stationary and hydrodynamic voltammogramic analyses were performed. The electrochemical reversibility can be determined from cyclic voltammetry of the BCPIP-Co(II) complex at different scan rates. For the BCPIP-Co(II-III) redox reactions (Figure 3.6a), increasing the scan rate results in an increase of both the peak currents and peak separations. For instance, the peak separations increased from 65 to 78 mV at scan rates of 25 mV/s and 1.0 V/s, respectively, indicating the quasi-reversible nature of the redox processes (Figure 3.7a).^[114] Thus, the standard rate constant, k^0 , was determined to be 9.22×10^{-3} cm/s using Nicholson's analysis,^[172] based upon the peak separations at different scan rates (Figure 3.7b). For the BCPIP-Co(II-I) redox reactions (Figure 3.6b), it is observed that the anodic peak position does not increase with scan rate, while the cathodic peak shifts to lower potentials. This behaviour is attributed to adsorption of the BCPIP-Co(I) on the glassy carbon electrode (vide supra and infra). As such,

Nicholson's method cannot be applied to determine the rate constant for the BCPIP-Co(II-I) redox reaction.

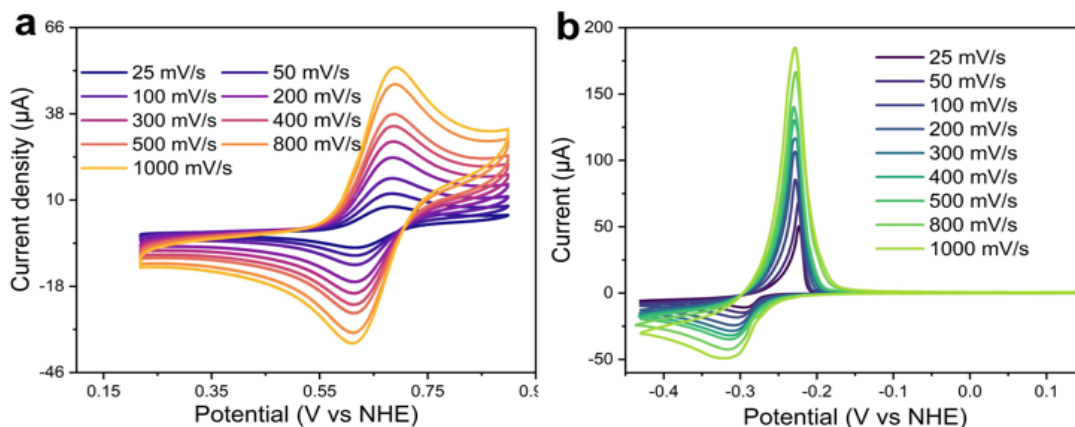


Figure 3.6. (a) CV curves of 2 mM BCPIP-Co(II-III) at pH 3.0 at various scan rates from 0.025 V/s to 1.0 V/s in 0.5 M NaCl (aq). (b) CV curves of 2 mM BCPIP-Co(II-I) at pH 3.0 at various scan rates from 0.025 V/s to 1.0 V/s in 0.5 M NaCl (aq). The potential axes were corrected for the uncompensated ohmic resistance. Reproduced from reference 61. Copyright (2020) Royal Society of Chemistry.

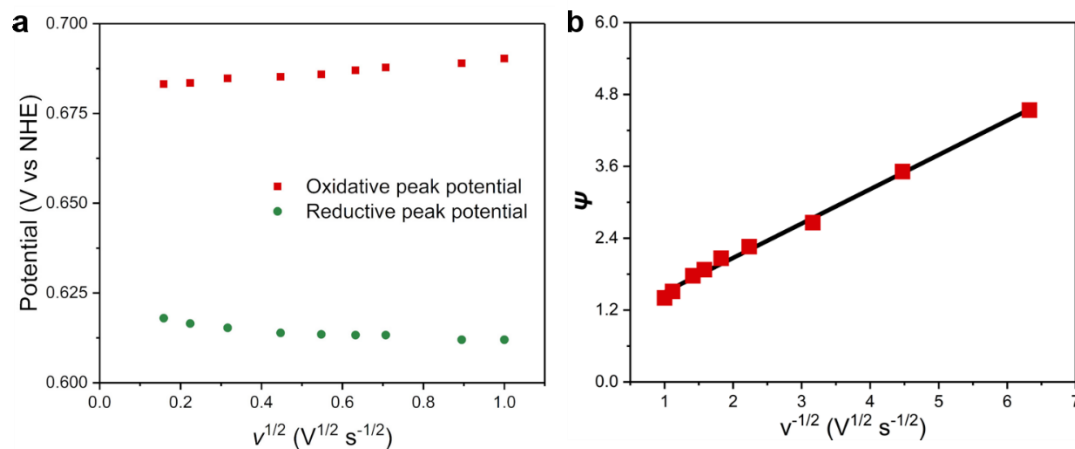


Figure 3.7. (a) Reductive and oxidative peak potential change with the square root of scan rate $v^{1/2}$ for the corresponding CV curves of BCPIP-Co(II), Co(II/III) redox couple, at pH 3.0. (b) Nicholson's analysis for examination of heterogeneous electron-transfer rate constant k^0 : plot of the dimensionless kinetic parameter (ψ) vs square root of scan rate (v). Reproduced from reference 61. Copyright (2020) Royal Society of Chemistry.

Rotating disk electrode (RDE) analysis allows for the determination of the diffusion coefficient for quasi-reversible, reversible and irreversible reactions. Figure 3.8a shows linear sweep voltammograms (LSV) for the anodic reaction of the BCPIP-Co(II) complex, at a scan rate of 5 mV/s and different rotation speeds, ranging from

300 to 2400 rpm. The diffusion coefficient (D_0) was calculated to be $2.11 \times 10^{-6} \text{ cm}^2/\text{s}$ by fitting the data in Figure 3.8b. Extrapolating the Koutecký–Levich plots (Figure 3.8c) at different overpotentials to infinite rotation speeds yields the kinetic current, i_k , which is only dependent on the reaction kinetics in the absence of any mass-transfer effects. Thus, the heterogeneous electron transfer rate constant (k^0) can be calculated by fitting i_k versus overpotential, as seen in Figure 3.8d. In agreement with the Nicholson analysis for the standard rate constant (vide supra), k^0 is calculated from RDE analysis to be $9.4 \times 10^{-3} \text{ cm/s}$. This value is comparable to the rate constants reported for other high performance aqueous based RFB materials, such as TEMPO and viologen derivatives in the range of $(2.8 \text{ to } 4.2) \times 10^{-3} \text{ cm/s}$.^[67]

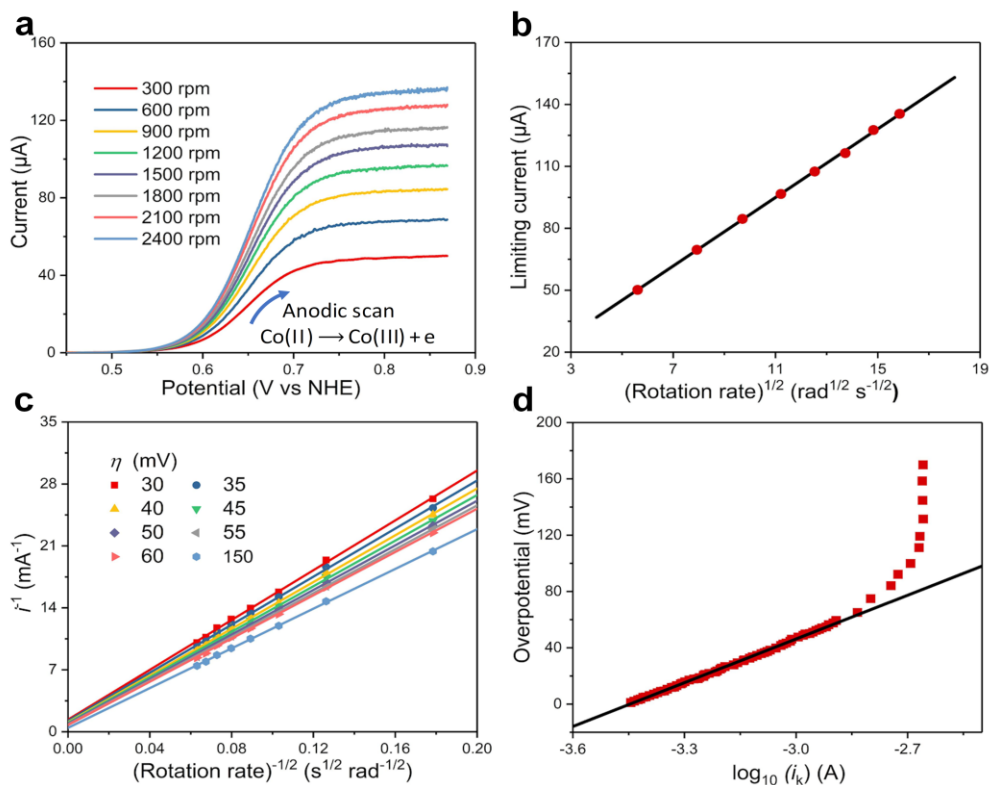


Figure 3.8. (a) Linear sweep voltammograms for the Co(II)/Co(III) redox reactions of the 2.0 mM BCPIP-Co(II) at different rotation speeds of the RDE in 0.5 M NaCl at a nominal pH of 3.0. (b) Limiting currents vs the square root of rotation rate (Levich plots) for BCPIP-Co(II); (c) Koutecký–Levich plot (i^{-1} vs $\omega^{-1/2}$) of BCPIP-Co(II). (d) Plot of the overpotential vs $\log_{10}(i_k)$. The overpotential is defined as $E_{\text{meas}} - E^0$. Reproduced from reference 61. Copyright (2020) Royal Society of Chemistry.

Due to the apparent adsorption of the BCPIP-Co(I) complex on the electrode surface at $\text{pH} < 3.5$, the standard rate constant for Co(II)/Co(I) redox reactions at $\text{pH} < 3.5$ could not be acquired from either the Nicholson method or the RDE analysis (Figure 3.9a). At pH values greater than or equal to 4, however, the adsorption signature disappears (*vide supra*). As shown in Figure 3.9b, Co(II)/Co(I) at pH 5 shows electrochemically quasi-reversible kinetics, with a peak-to-peak separation of 63 mV at 1.0 V/s, which is close to the of 59 mV expected for systems that are termed reversible.

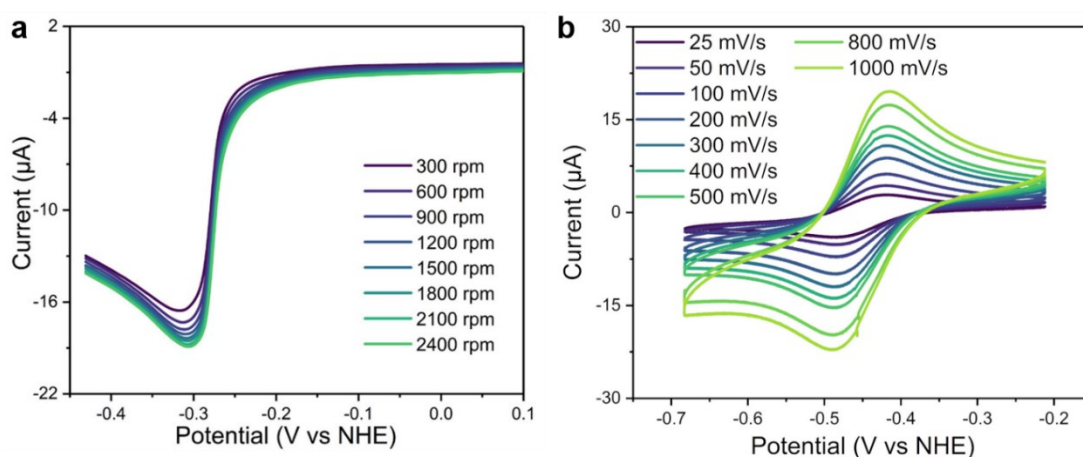


Figure 3.9. (a) Linear sweep voltammograms of 2.0 mM BCPIP-Co(II), Co(II/I) redox couple, in 0.5 M NaCl (aq) at pH 3.0 under various rotation speeds. Due to the weak interaction between the BCPIP-Co(I) complex with the electrode surface, a peak at ca. -0.3 V vs NHE and seemingly coincident plots are observed in the current–potential region typically used for the mass transfer correction and extraction of kinetic information, thus, impeding further kinetic analysis for the redox reaction [Co(II)/Co(I)] using RDE. (b) Cyclic Voltammograms of 1 mM BCPIP-Co(II), Co(II/I) redox couple, at various scan rates from 0.025 V/s to 1.0 V/s in 0.5 M NaCl (aq) at pH 5.0. Reproduced from reference 61. Copyright (2020) Royal Society of Chemistry.

As a proof-of-concept for an aqueous RFB, a symmetric system was assembled with the BCPIP-Co(II) complex acting as both catholyte and anolyte (Figure 3.10). As the received carbon paper (Sigracet SGL 39AA) is hydrophobic, oxygen-plasma was applied to provide a fast way (6 min, compared with 24 h heat treatment) to create a hydrophilic surface (Figure 3.11). The BCPIP-Co(II) theoretically could produce a cell voltage of 0.93 V for a symmetric RFB configuration based upon the two redox pairs, BCPIP-Co(II-III), with an E^0 of 0.65 V vs NHE, and BCPIP-Co(I-II), with an E^0 of -0.28 V vs NHE. Because of the subtle differences of the two couples at different pH

values, the stability was investigated by performing 100 CV sweeps at pH 3.0, 3.5, 4.5, and 5.0, Figure 3.12 and Figure 3.13. The degree of degradation with cycling was estimated by measuring the changes in peak heights and area of the CV curves, as shown in Figure 3.14. Together, they indicate that the BCPIP-Co(II-III) couple is most stable to electrochemical cycling at pH 3.5.

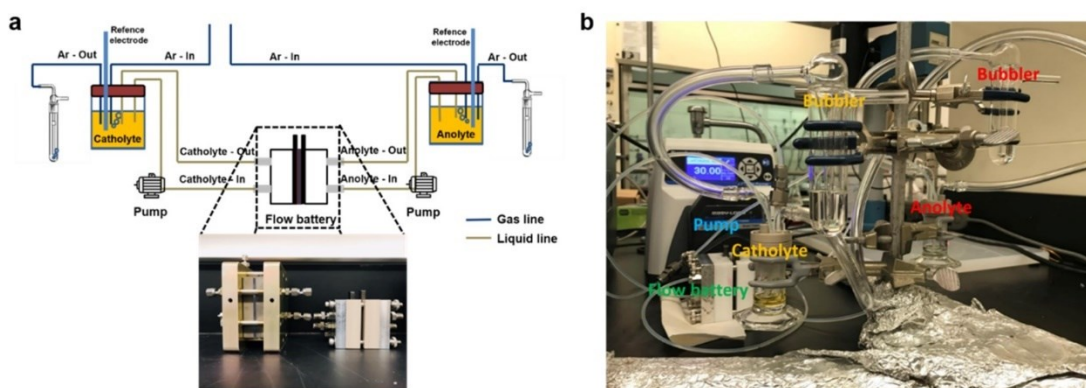


Figure 3.10. (a) Schematic and (b) optical image of the lab-designed flow battery system.

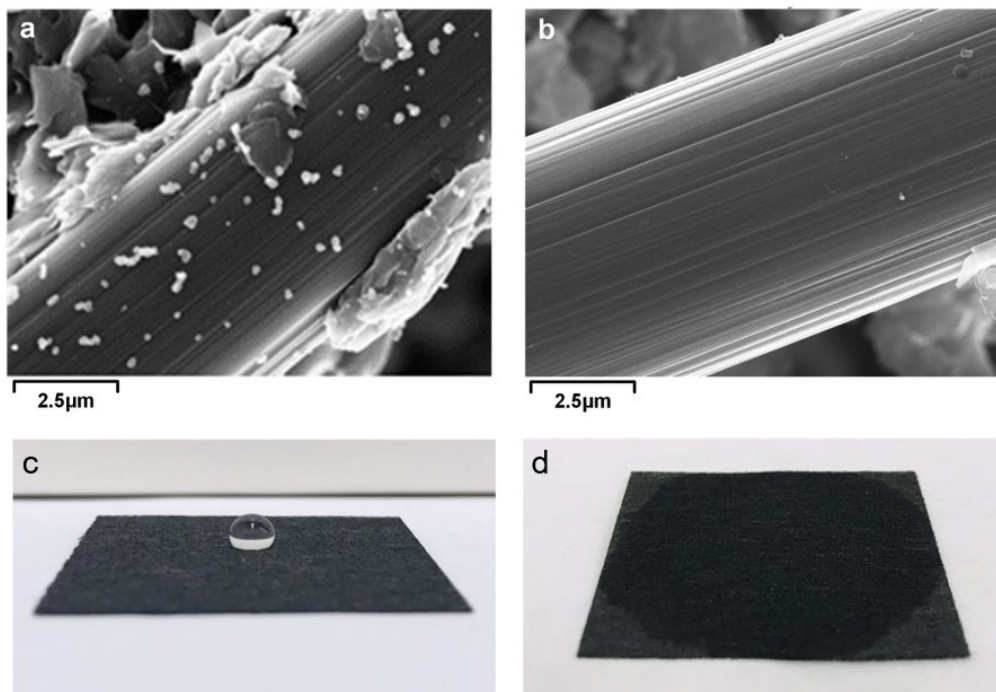


Figure 3.11. (a) SEM of pristine carbon paper as received from Sigracet 29 AA. (b) SEM of O₂-plasma-pretreated carbon paper. After O₂ plasma, the carbon fibers have fewer scattered particles and show negligible morphological changes of the carbon fibers themselves. Water wetting properties of carbon paper (c) before oxygen plasma (d) after oxygen plasma treatment. Reproduced from reference 61. Copyright (2020) Royal Society of Chemistry.

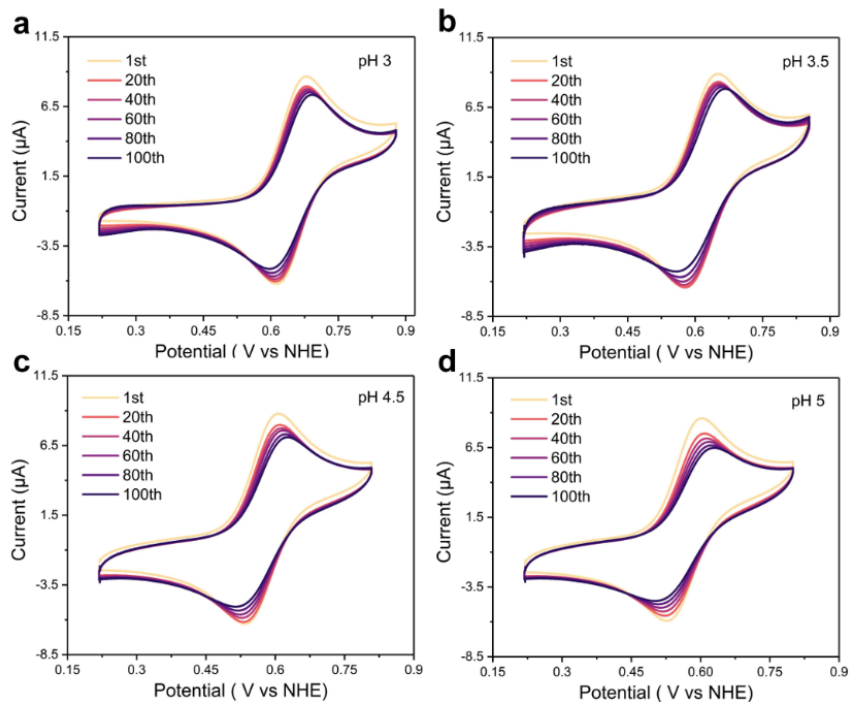


Figure 3.12. CV curves as a function of cycle number for 1 mM BCPIP(II), Co(II/III) redox couple, in 0.5 M NaCl (aq) at a rate of 100 mV/s for different pH levels. (a) pH 3.0, (b) pH 3.5, (c) pH 4.5, and (d) pH 5.0. The number of cycles is shown as an inset in each panel. Reproduced from reference 61. Copyright (2020) Royal Society of Chemistry.

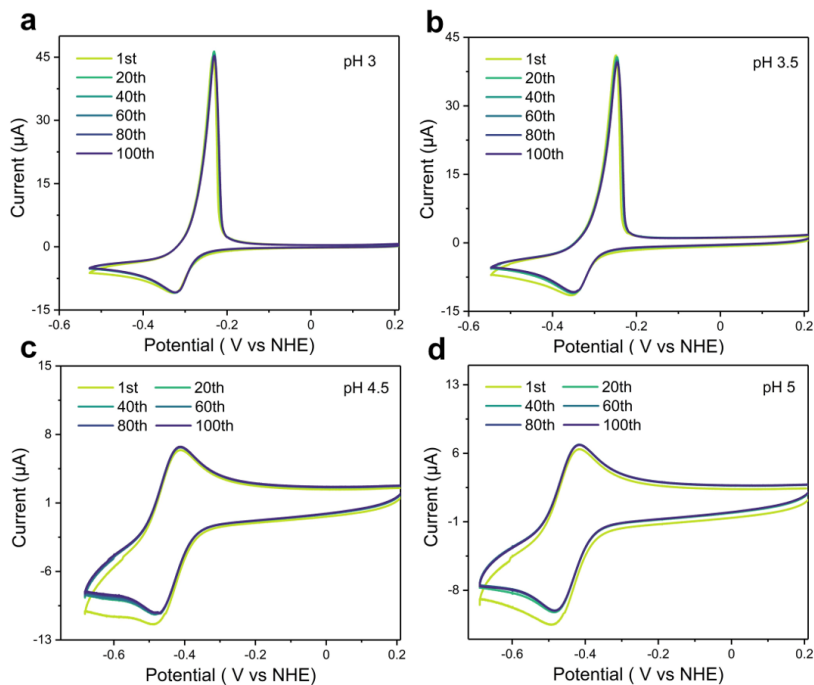


Figure 3.13. CV curves as a function of cycle number for 1 mM BCPIP(II), [Co(II/I)] redox couple, in 0.5 M NaCl (aq) at a rate of 100 mV/s for different pH levels. (a) pH 3.0, (b) pH 3.5, (c) pH 4.5, and (d) pH 5.0. The number of cycles is shown in the inset in each panel. Reproduced from reference 61. Copyright (2020) Royal Society of Chemistry.

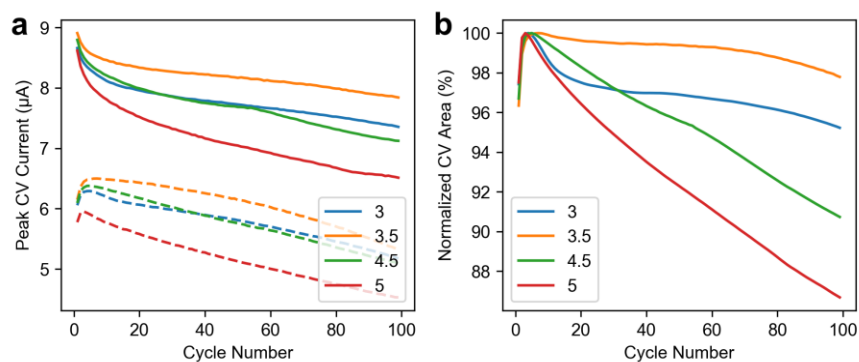


Figure 3.14. Analyses of peak currents and areas from Figure 3.12. (a) The absolute values of the peak currents for the anodic (solid lines) and cathodic (dashed lines) sweeps of the 1 mM catholyte CV per cycle. (b) The normalized area is given as a percentage of the area between the anodic and cathodic sweeps of the 1 mM catholyte CV per cycle. Reproduced from reference 61. Copyright (2020) Royal Society of Chemistry.

The first symmetric cell tested used 10 mM BCPIP-Co(II) and 0.5 M NaCl (aq), at pH 3.5, as both catholyte and anolyte (Figure 3.15). After the first 5–10 cycles, the coulombic efficiencies stabilized to ~98%, but this value resulted in a decay of capacity to about half after only 25 cycles, *vide infra* (Figure 3.16b). After 100 cycles, a post-mortem analysis revealed that the membrane had changed from colourless to brown. Energy-dispersive X-ray spectroscopy (EDX) analysis of the anion exchange membrane (fumasep FAS-30) showed the existence of cobalt on the membrane surface (Figure 3.17b), pointing to possible adsorption of the cobalt complex. As was expected, due to possible adsorption from the anion exchange membrane, changing to a new membrane could help reduce this effect. However, changing the membrane from an anion to a cation exchange membrane (Nafion 212) also resulted in a change of membrane color to brown, which was shown by EDX analysis to contain cobalt (Figure 3.17b and Figure 3.18c). Adsorption of the charged BCPIP-Co(II) complex on both membranes might occur during the (dis)charge processes; we cannot, however, exclude the possible existence of Co-based degradation byproducts. Moreover, in addition to the adsorption on the membrane surface, we found evidence for surface adsorption on the carbon paper electrode, Figure 3.19. After 100 cycles for a symmetric cell of 10 mM BCPIP-Co(II), immersion of the carbon paper electrodes that were used in the anolyte and catholyte compartments in pure water resulted in dark brown and light brown solutions, respectively, pointing to adsorption of the BCPIP-Co complex on the

carbon papers, particularly within the anolyte half-cell (the Co(II-I) redox reaction). Adsorption of the cobalt complex on the membrane and electrodes could explain the high capacity decay when higher concentrations (in this case, 10 mM) of BCPIP-Co(II) are used.

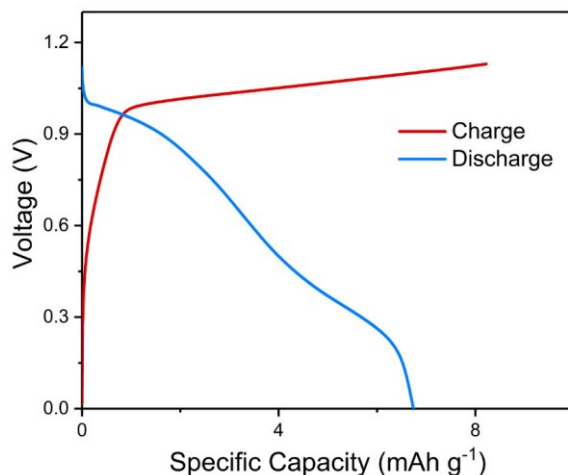


Figure 3.15. (a) Charge–discharge profile of the 10 mM BCPIP-Co(II) symmetric flow battery at pH 3.5. Reproduced from reference 61. Copyright (2020) Royal Society of Chemistry.

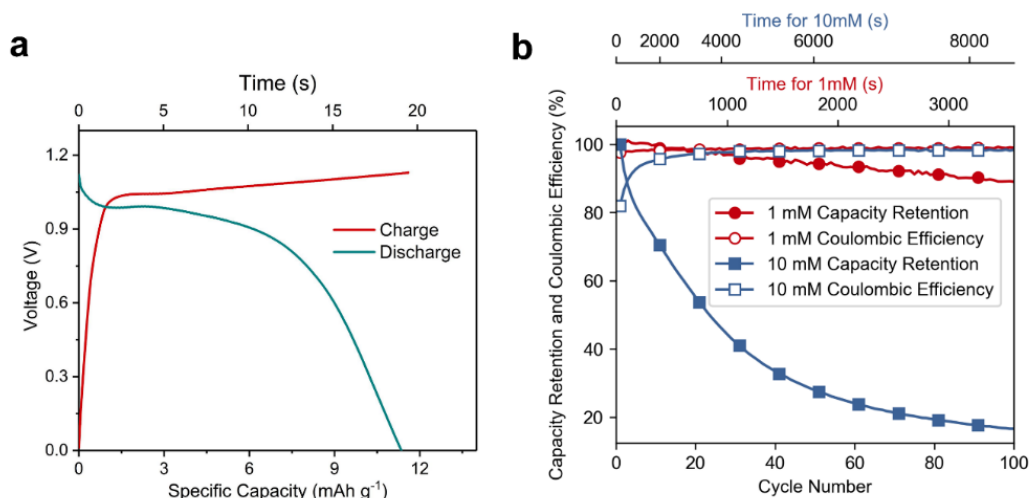


Figure 3.16. (a) Charge–discharge profile of the symmetric BCPIP-Co(II) RFB at 2 mA/cm² with 1 mM of BCPIP-Co(II) as catholyte and anolyte at a pH of 3.5. The specific capacity was calculated based on the mass of BCPIP-Co(II). (b) Cycling stability and coulombic efficiency of the symmetric BCPIP-Co(II) flow battery at 2 mA/cm² with 1 mM and 10 mM of BCPIP-Co(II) as catholyte and anolyte. Reproduced from reference 61. Copyright (2020) Royal Society of Chemistry.

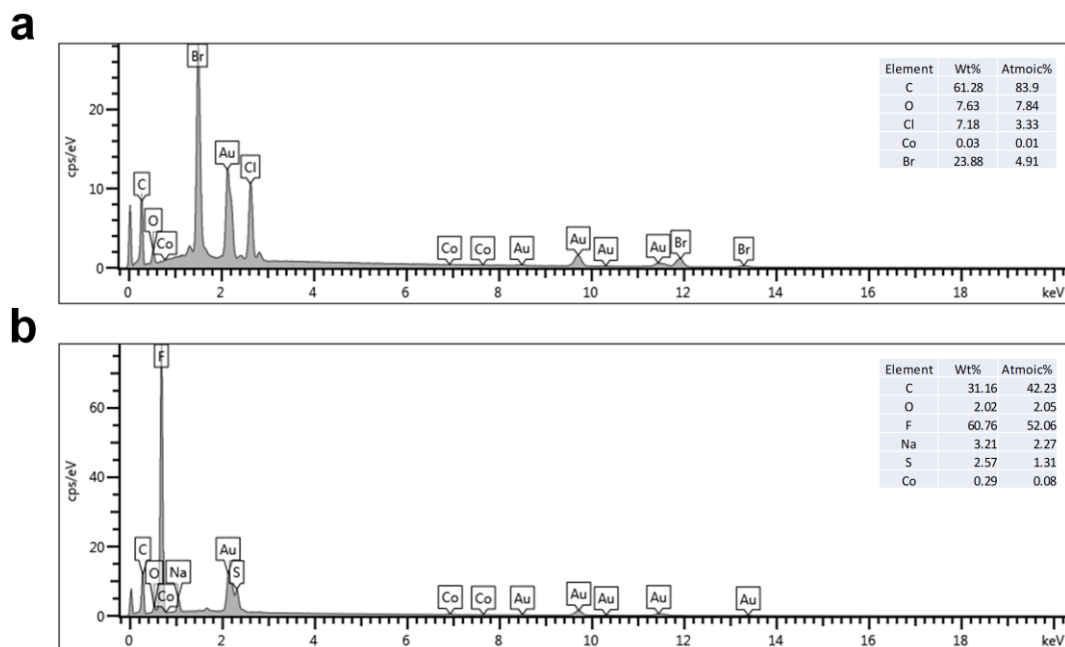


Figure 3.17. (a) EDX of gold-coated fumasep FAS-30 membrane from the 10 mM BCPIP-Co(II) symmetric cell at pH 3.5 after 100 cycles. (b) EDX of gold-coated Nafion 212 membrane from the 10 mM BCPIP-Co(II) symmetric cell at pH 3.5 after 100 cycles. Reproduced from reference 61. Copyright (2020) Royal Society of Chemistry.

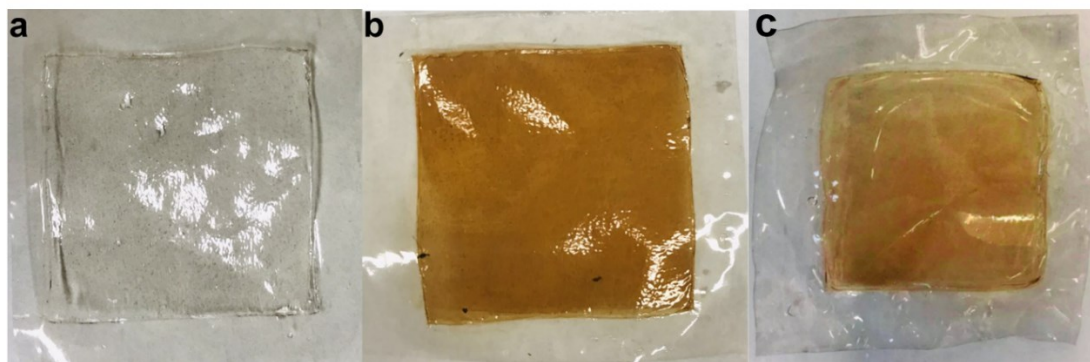


Figure 3.18. Photographs: (a) Membrane from the 1 mM BCPIP-Co(II) symmetric cell at pH 3.5 after 100 cycles; (b) fumasep FAS-30 membrane from the 10 mM BCPIP-Co(II) symmetric cell at pH 3.5 after 100 cycles. (c) Nafion 212 membrane from the 10 mM BCPIP-Co(II) symmetric cell at pH 3.5 after 100 cycles. (In the case of 10 mM BCPIP-Co(II) symmetric cell, upon pumping water into the cell, one would expect to observe colourless solutions at the outlets of both the catholyte and anolyte compartments. However, upon rinsing the cell, a colorless solution emerged from the catholyte side, but a red solution was observed to come out of the anolyte compartment, most likely due to adsorption of anolyte on the membrane.) Reproduced from reference 61. Copyright (2020) Royal Society of Chemistry.

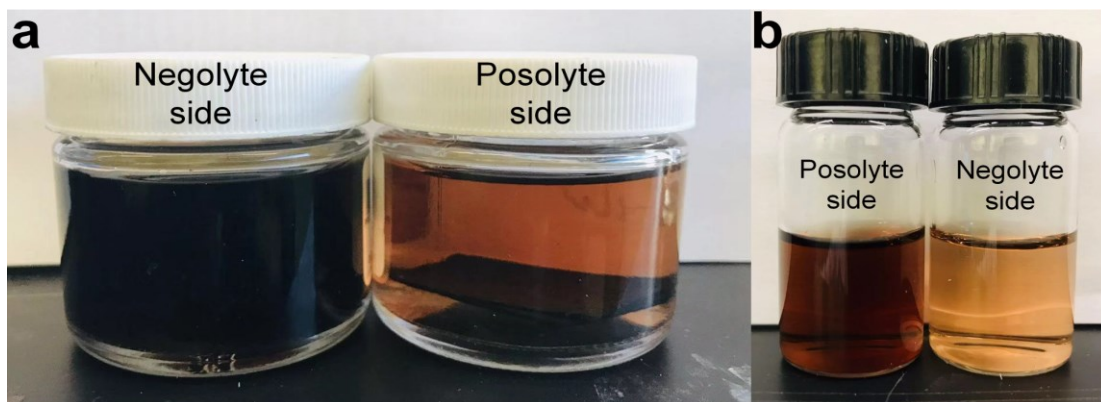


Figure 3.19. (a) Carbon papers removed from both catholyte and anolyte sides from the 10 mM BCPIP-Co(II) symmetric cell at pH 3.5 after 100 cycles, after soaking in ultrapure 18 M Ω cm water overnight. (b) The catholyte and anolyte solutions diluted 15x with ultrapure 18 M Ω cm water, from the 10 mM BCPIP-Co(II) symmetric cell at pH 3.5 after 100 cycles. Reproduced from reference 61. Copyright (2020) Royal Society of Chemistry.

To better understand the origins of the observed capacity fade, CV sweeps were performed to a high cutoff anodic potential of 1.5 V vs NHE (Figure 3.20). A clear irreversible anodic peak appears at 1.2 V, which shifts to higher potentials upon cycling and results in a significant decrease of peak currents for the Co(II)/Co(III) redox reactions, indicating that an electrochemically irreversible reaction occurs at higher potentials, possibly due to degradation of the BCPIP-Co complex. Assuming this side-reaction at higher voltages to be limited kinetically, the rate of membrane fouling will worsen with increasing concentrations of the cobalt complex. Then, a less concentrated solution, of 1 mM BCPIP-Co(II) at pH 3.5 was tested to minimize adsorption on the membrane and carbon paper electrodes. A pumped flow rate of 60 ml/min was applied, with a constant current density of 2 mA/cm². Charging was limited to a cutoff voltage of 1.13 V, which was found to achieve a reasonable balance between capacity and capacity fade; at high cutoff voltages, the initial capacity would increase, but it fades rapidly due the increased rates of the previously discussed side-reaction at higher voltages. As such, this voltage cutoff limited the capacity to only 41% of the theoretical value. The voltage and energy efficiencies were found to be 73.2% and 73.5%, respectively, and the Coulombic efficiency was ~99.0%, with a capacity retention of 89% after 100 cycles (Figure 3.16b). The energy density is 8.4 mWh/L for the whole cell, which is too low for real-world applications but is similar to that of other exploratory work that examined aqueous symmetric metal-ligand complexes.^[192]

Moreover, as shown in Figure 3.18a for 1 mM BCPIP-Co(II), there was a negligible change in the colour of the membrane after 100 cycles. As seen in Figure 3.16a, the galvanostatic charge–discharge profiles both show a plateau around 1 V, along with a volumetric capacity of 10.5 mAh/L, which is 41% of the theoretical value of 25.3 mAh/L. Due to the low concentration, it is difficult to keep a constant SOC and conduct polarization experiments. Future work needs to be done to achieve stable high concentration BCPIP-Co(II)-based symmetric ARFBs if one wishes to conduct polarization experiments.

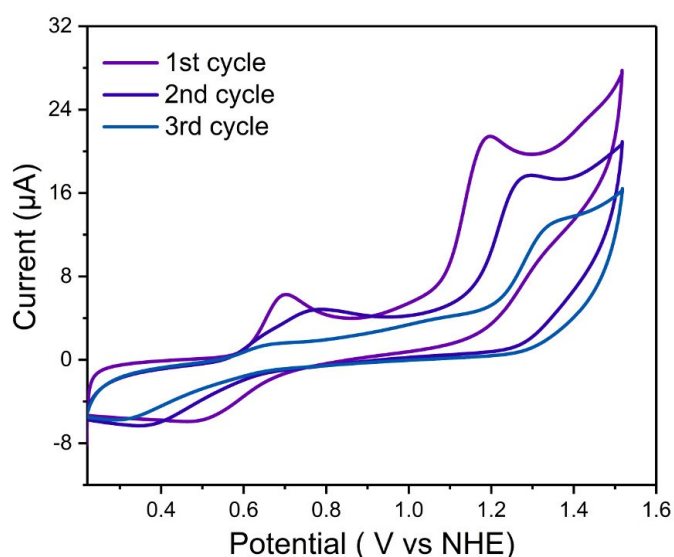


Figure 3.20. CV cycling of 1 mM of BCPIP-Co(II) in 0.5 M NaCl (aq) at pH 3.5 over an extended voltage window from 0.3 to 1.5 V vs NHE. Reproduced from reference 61. Copyright (2020) Royal Society of Chemistry.

3.3 Conclusions

A pH-responsive, water-soluble cobalt complex, BCPIP-Co(II), with two redox couples that fall within the window of water oxidation and reduction was investigated and tested in an aqueous symmetrical redox flow battery architecture. Within the range of pH of 1.5 to 5.5, the overall charges of the species present in solution range from +3 to –3, which affect characteristics such as redox potentials and adsorption properties on the electrode surface. The electrochemical analysis reveals fast kinetics for both the Co(II)/Co(I) and Co(II)/Co(III) redox couples. The symmetric aqueous RFB, using 1 mM BCPIP-Co(II) for both the anolyte and catholyte, displays a capacity retention of

ca. 89% over 100 cycles. Chemical functionalization of the BCPIP-Co(II) complex with more hydrophilic groups and manipulation of counterions may improve the solubility and electrochemical cycling performance of this anolyte further.^[75, 127]

3.4 Experimental Section

Chemicals and instruments. All the chemicals were purchased from Sigma-Aldrich or Alfa Aesar and used directly without further purification. Milli-Q water was sparged with Ar for 2 h before use. ¹H and ¹³C NMR spectra were recorded on an Agilent VNMRS (700 MHz) spectrometer and referenced to DMSO (δ 2.49 ppm) for ¹H NMR. UV-vis spectra were collected with a Perkin Elmer Lambda 1050 UV-Vis-NIR spectrophotometer (Figure 3.21d). A VWR Symphony SB70P pH meter was used for pH measurements. The SEM images were taken with a ZEISS SIGMA field emission scanning electron microscope. Mass spectra were obtained using an Agilent 6220 oaTOF in electrospray mode. Solution magnetic susceptibilities were measured by the Evans method.¹ The FTIR sample was prepared by spin-casting on the surface of a shard of a native oxide-capped silicon wafer. The FTIR spectra were obtained using a Nicolet Nexus 760 spectrometer with a liquid nitrogen-cooled MCT detector and a nitrogen-purged sample chamber in transmission mode. Elemental analysis was acquired on a Thermo Flash 2000 Elemental Analyzer. X-ray crystallographic details are described Section 3. All cyclic voltammograms were recorded with a Biologic Science Instruments VSP multichannel potentiostat using EC-Lab V11.20 software and referenced vs Ag/AgCl reference electrode (3 M NaCl). Detailed procedures for electrochemical kinetic study and redox flow battery cycling experiments are described below.

Synthesis of 2,6-Bis[1-(4-carboxyphenylimino)ethyl]pyridine (BCPIP). 2,6-Diacetylpyridine (2.7 g, 14.6 mmol) and *p*-aminobenzoic acid (5 g, 36.4 mmol) were dissolved in 300 ml of dry xylene. The reaction mixture was heated to reflux under Ar for 2 d, with constant stirring. A Dean–Stark trap was applied to remove water and 65 ml of xylene every 12 h (total 260 ml). After 2 d, the mixture was cooled to room temperature, and the residual solvent was removed under reduced pressure. The solid residue was washed with methanol to yield 5.99 g of a light-yellow powder after drying

under vacuum. The yield was ca. 93%. ^1H NMR (DMSO- d_6 , 499.801 MHz, 27 °C): δ (in ppm), 2.33 (s, 6H), 6.95 (d, 4H), 7.95 (d, 5H), 8.07 (t, 1H), 8.32 (d, 2H), 12.73 (s, 2H). ^{13}C NMR (DMSO- d_6 , 125.689 MHz, 27 °C): δ (in ppm), 16.16, 119.00, 122.68, 125.93, 130.56, 137.74, 154.40, 154.89, 166.84, 167.01. ESI-MS, m/z : 400 [BCPIP - H] $^-$.

Synthesis of 2,6-Bis[1-(4-carboxyphenylimino)ethyl]pyridine cobalt(II) chloride (BCPIP-Co). BCPIP (1 g, 2.49 mmol) and $\text{CoCl}_2 \cdot 6\text{H}_2\text{O}$ (0.295 g, 1.25 mmol) were combined in 75 ml of methanol and stirred at room temperature for 1 h. Then, the solvent was removed under reduced pressure. The dark red solid was washed with acetonitrile and vacuum-dried at room temperature. The yield was 95%. Anal. Calcd for $\text{C}_{46}\text{H}_{38}\text{CoN}_6\text{O}_8$: C = 59.25, H = 4.07, N = 9.01. Found: C = 58.86, H = 4.07, N = 8.87. ESI-MS, m/z : 430 [BCPIP-Co - 2 Cl] $^{+2}$, 860 [BCPIP-Co - 2 Cl] $^+$. Magnetic susceptibility (methanol- d_4 , 27 °C): $\mu_{\text{eff}} = 2.44 \mu_{\text{B}}$.

UV-vis studies. The UV-vis spectra of BCPIP-Co(II) under different pH values were taken with an aqueous solution of 0.02 mM of BCPIP-Co(II) in 0.5 M NaCl (aq). The pH values were adjusted using aqueous 0.1 M NaOH and 0.1 M HCl solutions. The solution, after adjustment, was allowed to equilibrate for at least 4 min.

Solubility tests. The solubility limit of BCPIP-Co(II) was measured by adding the BCPIP-Co(II) in water, at room temperature, until no further solid could be dissolved. The saturated solution was obtained by filtering the mixture through a 0.2 μm PTFE syringe filter. The saturated solution was diluted and evaluated by UV-vis spectrophotometer (PerkinElmer Lambda 1050 UV-Vis-Nir spectrophotometer). A pre-calibrated absorbance-concentration curve with a known concentration of BCPIP-Co(II) was used to calculate the maximum concentration (Figure 3.21).

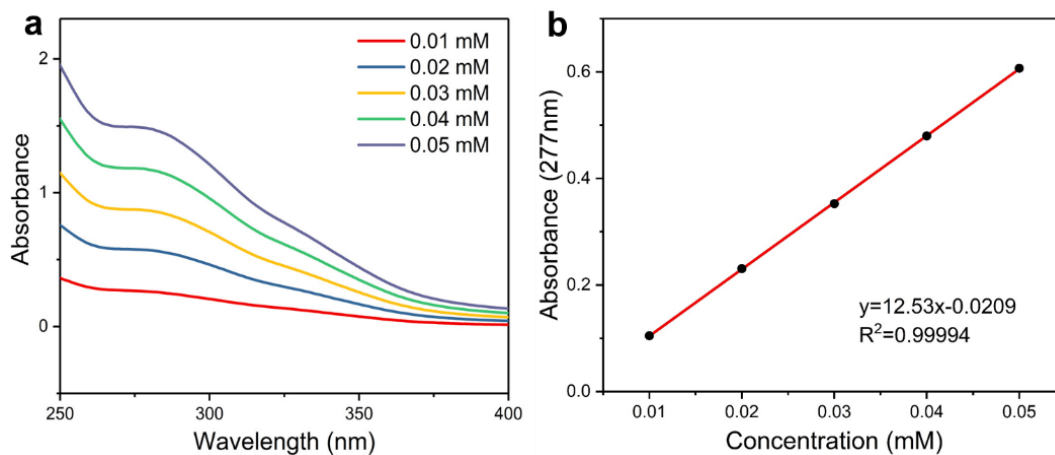


Figure 3.21. (a) UV-vis spectra of BCPIP-Co(II) at different concentrations. The solutions were prepared by using ultrapure 18 M Ω cm water, and the pH was not controlled (the ‘native’ pH). (b) Absorbance at 338 nm as a function of concentration. The solutions were prepared by using ultrapure 18 M Ω cm water, and the pH was not controlled (‘native’ pH). Reproduced from reference 61. Copyright (2020) Royal Society of Chemistry.

Electrochemical studies. Cyclic voltammetry (CV) and rotating disk electrode (RDE) tests were performed on Biologic Science Instruments VSP multichannel potentiostat using a three-electrode set-up with a glassy carbon electrode (3 mm for CV studies and 5 mm for RDE studies), a platinum counter electrode, and an Ag/AgCl reference electrode. All electrochemical studies were conducted in 0.5 M NaCl (aq) electrolyte solutions under an Ar atmosphere. The working electrode was polished with 1-micron and 0.05-micron alumina powder and rinsed with Milli-Q water before each experiment. CV curves were recorded at a sweep rate of 50 mV/s or specific rates, where indicated. The pH values were adjusted by aqueous HCl or NaOH solutions.

Reversibility. In order to investigate the reversibility of the protonation/deprotonation of the carboxylic acid groups for the BCPIP-Co(II) complex, the CV was run at pH 3, then the pH then increased to 5.5, followed by lowering it back down to pH 3.0. As shown in Figure 3.4, the CVs for the Co(II)/Co(I) and Co(II)/Co(III) redox reactions at pH 3.0 before and after raising the pH are superimposed. Thus, under these conditions, the complex is chemically and electrochemically stable upon deprotonation and protonation of the carboxylic acid/carboxylate groups in this range.

Full cell performance. These tests were carried out using a Biologic Science Instruments VSP multichannel potentiostat and a flow cell. The flow cell for BCPIP-

Co was constructed with a zero-gap flow cell from Fuel Cell Tech, comprised of POCO graphite flow plates with a serpentine flow pattern in combination with 10 cm² geometric surface area electrodes stacked of pieces of carbon paper (Sigracet SGL 29AA) on each side. The carbon paper was pretreated under oxygen plasma using plasma cleaner (Harrick PDC 32G, 18 W) at 0.8 Torr for 6 min to create a hydrophilic surface (Figures 3.11). Viton gaskets were used to achieve an ~20% compression of the carbon papers. A sheet of pretreated anion exchange membrane (fumasep FAS-30, Fumatech, Germany), which had been stored in 1 M NaCl (aq) overnight, was sandwiched between carbon papers. Two glass reservoirs were filled with 10 ml of 0.5 M NaCl (aq) electrolytes containing a certain concentration of active materials. A peristaltic pump (Cole-Parmer Masterflex L/S) was used to feed the electrolytes into the flow cell through Viton tubing at a rate of 60 ml/min. The specific capacity was calculated based on the mass of BCPIP-Co. Both reservoirs were purged with argon and sealed before cell cycling. The cell was galvanostatic charged/discharged between 1.13 V and 0 V at a current of 20 mA. EIS was conducted from 99 kHz to 6 Hz using a 10 mV sine perturbation at 50% SOC.

3.4.1 Determination of Kinetic Parameters

For RDE experiments, a Pine Instrument ASR rotator was used to control the rotation speed. Linear sweep voltammetry studies were carried out at a rate of 5 mV/s when the disk electrode was rotated at a specific speed. The limiting current $i_{l,a}$, measured at 0.86 V, was plotted versus the rotation rate (ω). The Levich plot showed a linear relationship between limiting current and square root rotation rate. The slope of the fitted line is defined by the Levich equation,

$$i_{l,a} = \left(0.62nFAD^{\frac{2}{3}}\nu^{-\frac{1}{6}}C_o\right)\sqrt{\omega} \quad 3.1$$

where n is the number of electrons involved, F is the Faraday's constant, A is the electrode area, C_o is the concentration of BCPIP-Co, and ν is the kinematic viscosity (0.01024 cm²/s for 0.5 M NaCl). The diffusion coefficient, D , of BCPIP-Co was calculated from the Levich equation.

A series of plots of reciprocal of square root rotation rate versus measured current at different overpotentials were extrapolated to infinite rotation rate to obtain kinetic current (i_k , without mass transfer effect), based on Koutecký–Levich equation,

$$\frac{1}{i_m} = \frac{1}{i_k} + \frac{1}{i_{l,a}} = \frac{1}{i_k} + \frac{1}{(0.62nFAD\frac{2}{3}v^{-\frac{1}{6}}C_0)\sqrt{\omega}} \quad 3.2$$

where i_m is the measured current, $i_{l,a}$ is the limiting current, as previously defined by Equation 3.1. Using these values of kinetic current as a function of overpotential, the rate constant k^0 is determined using the current-potential equation,²

$$\log_{10}(i_k) = -\frac{\alpha nF(E-E^0)}{RT} \log_{10}(e) + \log_{10}(nFAC_0^{\text{bulk}}k^0) \quad 3.3$$

where E is the electrode potential, E^0 is the formal electrode potential, α is the charge transfer coefficient (assumed to be equal to 0.5), n is the number of electrons involved in the reaction, F is Faraday's constant, R is the ideal gas constant, T is the temperature, A is the electrode area, and C_0^{bulk} is the bulk concentration of BCPIP-Co(II). The rate constant k^0 , is determined from the x -intercept of fitting a straight line through a plot of $\log_{10}(i_k)$ versus $E - E^0$. All the electrochemical experiments were performed three times at room temperature.

Nicholson's analysis is another classic and frequently used method to estimate rate constants for quasi-reversible systems. The peak to peak separation ΔE_p is only a function of a dimensionless kinetic parameter, ψ , when $0.3 < \alpha < 0.7$. The corresponding relations between ψ and ΔE_p can be obtained from the table in the original paper.³ Due to the discrete points in the table, for practical usage, Equation 3.4 is used to estimate ψ roughly.⁴

$$\psi = \frac{-0.6288 + 0.0021\Delta E_p}{1 - 0.017\Delta E_p} \quad 3.4$$

Following this, the Nicholson equation (Equation 3.5) was applied to calculate k^0 . It is assumed that $D_O = D_R$ and α .

$$\psi = \frac{(D_O/D_R)^{\alpha/2}k^0}{\sqrt{\pi D_O nFv/RT}} \quad 3.5$$

3.4.2 Crystallographic Data for BCPIP-Co

Purple crystals of BCPIP-Co(II) were grown by solvent diffusion of acetonitrile (top layer) into a concentrated methanol solution of BCPIP-Co(II). Thermal ellipsoid plots are shown in Figure 3.22. A purple crystal with the dimensions 0.63 x 0.29 x 0.24 mm³ was coated with a thin layer of hydrocarbon oil (Paratone-N) and then mounted on a

glass fiber before being quickly placed in a low-temperature stream of N₂ on the X-ray diffractometer.^[208] With the crystal cooled to -100 °C, all data were collected by Cu K α radiation on a Bruker D8 equipped with APEX II CCD detector. The data were corrected for absorption from the indexing of the crystal faces, based on Gaussian integration. The structures were solved by intrinsic phasing (SHELXT-2014)^[209] and refined using full-matrix least-squares on F² (SHELXL-2017).^[209] Non-hydrogen atoms are represented by Gaussian ellipsoids at the 30% probability level. The positions of hydrogen atoms were derived from attached carbon and oxygen atoms. The crystallographic experimental data are given in Table 3.2.

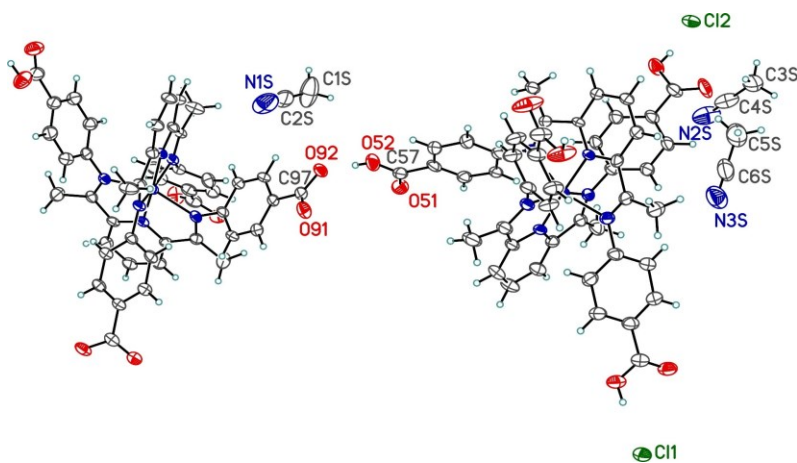


Figure 3.22. Perspective view of the whole contents of 2,6-Bis[1-(4-carboxyphenylimino)ethyl]pyridine cobalt(II) chloride, 2,6-Bis[1-(4-carboxyphenylimino)ethyl]pyridine cobalt(II) chloride acetonitrile solvate, showing the atom labelling scheme. Non-hydrogen atoms are represented by Gaussian ellipsoids at the 30% probability level. Hydrogen atoms are shown with arbitrarily small thermal parameters. Reproduced from reference 61. Copyright (2020) Royal Society of Chemistry.

Table 3.2. Crystallographic Experimental Details**A. Crystal Data**

CCDC	1954971
Formula	C150H130Cl4Co3N24O24
formula weight	2971.36
crystal dimensions (mm)	0.63 × 0.29 × 0.24
crystal system	orthorhombic
space group	Aba2 (No. 41)
unit cell parameters ^a	
a (Å)	13.2673(3)
b (Å)	66.3212(15)
c (Å)	19.2434(5)
V (Å ³)	16932.3(7)
Z	4
ρ_{calcd} (g cm ⁻³)	1.166
μ (mm ⁻¹)	3.406

B. Data Collection and Refinement Conditions

diffractometer	Bruker D8/APEX II CCD ^b
radiation (λ [Å])	Cu K α (1.54178) (microfocus source)
temperature (°C)	-100
scan type	ω and ϕ scans (1.0°) (5-20-40 s exposures) ^c
data collection 2θ limit (deg)	157.92
total data collected	95826 ($-16 \leq h \leq 16$, $-80 \leq k \leq 82$, $-23 \leq l \leq 23$)
independent reflections	15815 ($R_{\text{int}} = 0.0750$)
number of observed reflections	13322 [$F_o^2 \geq 2\sigma(F_o^2)$]
structure solution method	intrinsic phasing (SHELXT-2014 ^d)
refinement method	full-matrix least-squares on F^2 (SHELXL-2017 ^{e,f})
absorption correction method	Gaussian integration (face-indexed)
range of transmission factors	0.1042–0.0152
data/restraints/parameters	15815 / 1 / 937
Flack absolute structure parameter ^g	0.240(6)
goodness-of-fit (S) ^h [all data]	1.052
final R indices ⁱ	
R_1 [$F_o^2 \geq 2\sigma(F_o^2)$]	0.061
wR_2 [all data]	0.1446
largest difference peak and hole	0.532 and -0.581 e Å ⁻³

^aObtained from least-squares refinement of 9459 reflections with $5.32^\circ < 2\theta < 145.10^\circ$.

^bPrograms for diffractometer operation, data collection, data reduction and absorption correction were those supplied by Bruker.

^cData were collected with the detector set at three different positions. Low-angle (detector $2\theta = -33^\circ$) data frames were collected using a scan time of 5 s, medium-angle (detector $2\theta = 75^\circ$) frames using a scan time of 20 s, and high-angle (detector $2\theta = 117^\circ$) frames using a scan time of 40 s.

^dSheldrick, G. M. *Acta Crystallogr.* **2015**, *A71*, 3–8. (SHELXT-2014)

^eSheldrick, G. M. *Acta Crystallogr.* **2015**, *C71*, 3–8. (SHELXL-2017)

^fAttempts to refine peaks of residual electron density as disordered or partial-occupancy solvent oxygen or carbon atoms were unsuccessful. The data were corrected for disordered electron density through use of the SQUEEZE procedure as implemented in PLATON (Spek, A. L. *Acta Crystallogr.* **2015**, *C71*, 9–18. PLATON - a multipurpose crystallographic tool. Utrecht University, Utrecht, The Netherlands). A total solvent-accessible void volume of 831 Å³ with a total electron count of 170 (consistent with 9.5 molecules of solvent methanol, or 0.8 molecules per formula unit of solvent methanol molecule) was found in the unit cell.

^gFlack, H. D. *Acta Crystallogr.* **1983**, *A39*, 876–881; Flack, H. D.; Bernardinelli, G. *Acta Crystallogr.* **1999**, *A55*, 908–915; Flack, H. D.; Bernardinelli, G. *J. Appl. Cryst.* **2000**, *33*, 1143–1148. The Flack parameter will refine to a value near zero if the structure is in the correct configuration and will refine to a value near one for the inverted configuration. The value observed herein is indicative of racemic twinning, and was accommodated during the refinement (using the SHELXL-2014 TWIN instruction [see reference e]). Thus, the Flack parameter is provided for informational purposes only.

^h $S = [\sum w(F_o^2 - F_c^2)^2 / (n - p)]^{1/2}$ (n = number of data; p = number of parameters varied; $w = [\sigma^2(F_o^2) + (0.0413P)^2 + 34.3199P]^{-1}$ where $P = [\text{Max}(F_o^2, 0) + 2F_c^2] / 3$).

ⁱ $R_1 = \sum |F_o| - |F_c| / \sum |F_o|$; $wR_2 = [\sum w(F_o^2 - F_c^2)^2 / \sum w(F_o^4)]^{1/2}$.

Chapter 4

Molecular Engineering of a Biomimetic Phenazine-based Anolyte for Neutral Aqueous Redox Flow Batteries

4.1 Introduction

Phenazine and its derivatives are common in biological systems, as they are involved in a myriad of electron-transfer reactions.^[210] The phenazine moiety is sufficiently stable to be capable of undergoing two-electron reversible redox reactions (Figure 4.1a).^[211] Inspired by its vast structural diversity and various synthetic routes,^[210] its derivatives have started to be examined as the redox-active electrolyte in RFBs.^[78, 212, 213] [14] Though it is known to undergo reversible redox reactions,^[211] its intrinsic insolubility in water limits its applications in ARFBs. Recently, there have been efforts to increase the solubility of this molecule via the introduction of hydroxyl groups. In strongly basic solution, the OH group is deprotonated and ionized, thus increasing solubility. Alkaline or acid solutions could, however, lead to decomposition of anolytes and catholytes in ARFBs; therefore, we wished to avoid these pH extremes.^[173]

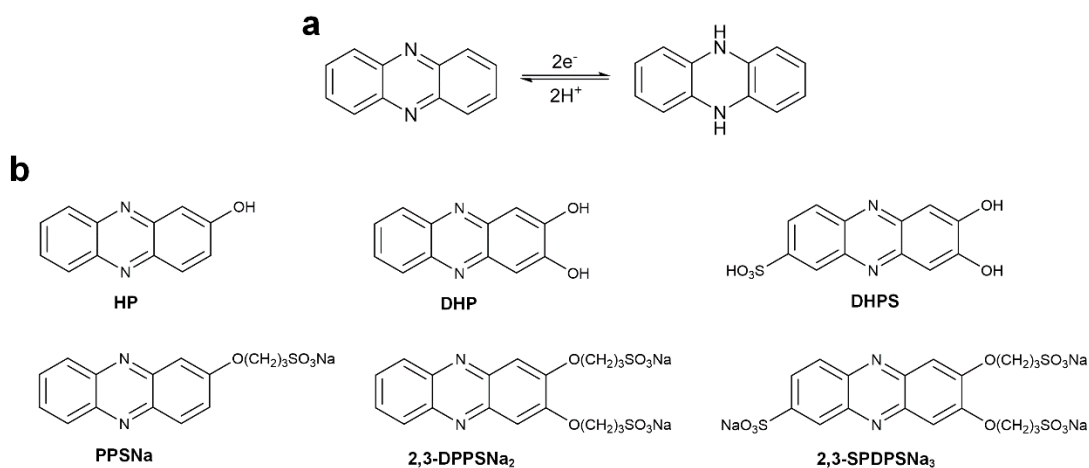


Figure 4.1. (a) Phenazine two-electron electrochemical redox reaction. (b) The molecular structures of the synthesized phenazine derivatives.

Here, we describe the design and synthesis of 3 phenazine-based electrolyte components functionalized with short flexible carbon chains that have been terminated with hydrophilic sulfonated groups, including sodium 3-(phenazin-2-yloxy)propane-1-sulfonate (PPSNa), sodium 3,3'-(phenazine-2,3-diylbis(oxy))bis(propane-1-sulfonate) (2,3-DPPSNa₂), and sodium 3,3'-((7-sulfonatophenazine-2,3-diyl)bis(oxy))bis(propane-1-sulfonate) (2,3-SPDPSNa₃) as anolytes in neutral ARFBs (Figure 4.1a). As will be described here, the substitutions of the phenazine backbone have obvious effects on both redox potential and solubility. Of these three phenazine derivatives, the PPSNa derivative showed the best characteristics for an RFB application, including a redox potential of -0.41 V vs standard hydrogen electrode (SHE) and a high solubility of 1.27 M in neutral water. Its redox potential is pH-tunable, which affects its electrochemical profiles. When coupled with ferrocyanide as the catholyte, the full cell showed good stability, as will be described here.

4.2 Results and Discussion

The 2-hydroxyphenazine (HP), 2,3-dihydroxyphenazine (DHP), and 7,8-dihydroxyphenazine-2-sulfonic acid (DHPS) derivatives were synthesized from low-cost precursors, benzoquinone and diaminobenzene, in aqueous solution.^[78, 79] The three phenazine derivatives, sodium 3-(phenazin-2-yloxy)propane-1-sulfonate (PPSNa), sodium 3,3'-(phenazine-2,3-diylbis(oxy))bis(propane-1-sulfonate) (2,3-DPPSNa₂), and sodium 3,3'-((7-sulfonatophenazine-2,3-diyl)bis(oxy))bis(propane-1-sulfonate) (2,3-SPDPSNa₃), were synthesized from HP, DHP, and DHPS, respectively. The hydroxy groups in the hydroxyphenazine derivatives react with 1,3-propanesultone to yield PPSNa, 2,3-DPPSNa₂, and 2,3-SPDPSNa₃ under mild conditions in high yield, as detailed in the Experiment Section. The formation of these three molecules was confirmed by NMR (¹H and ¹³C) (Figure 4.2 to Figure 4.7) and electrospray ionization mass spectrometry (ESI-MS).

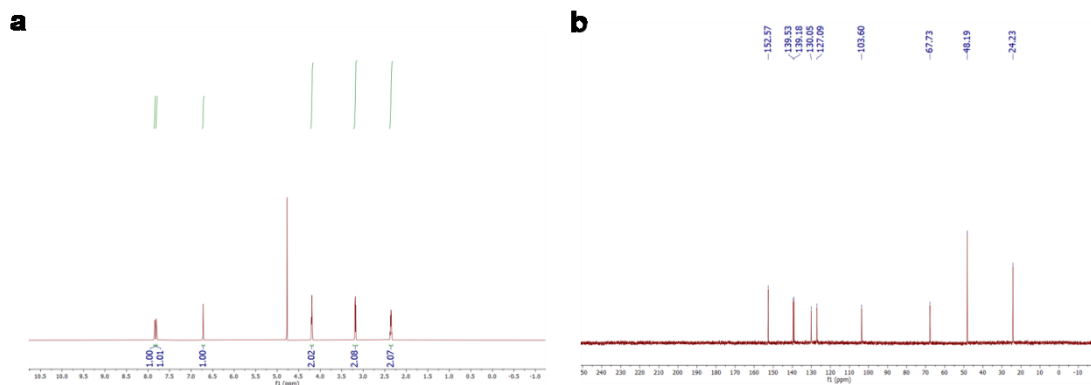


Figure 4.5. (a) ^1H NMR spectrum of the 2,3-DPPSNa₂ (D₂O, 27 °C). (b) ^{13}C NMR spectrum of the 2,3-DPPSNa₂ (D₂O, 27 °C). (See details about peak assignments in the Experimental Section)

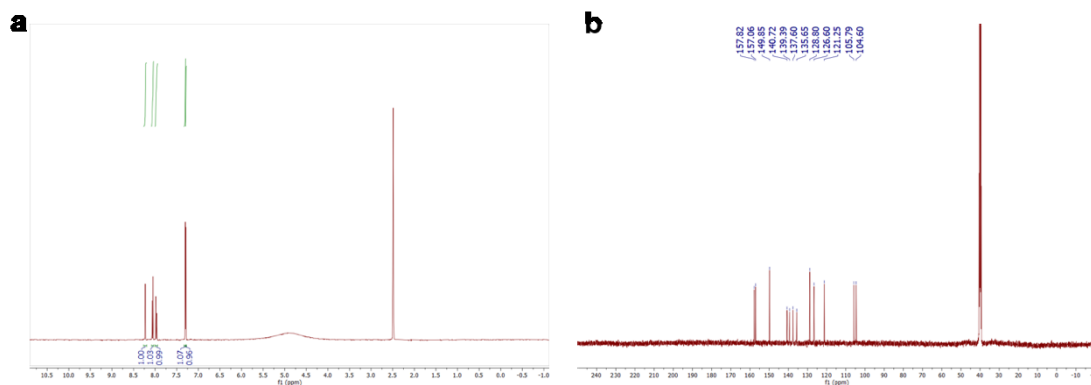


Figure 4.6. (a) ^1H NMR spectrum of the DHPS (DMSO-d₆, 27 °C). (b) ^{13}C NMR spectrum of the DHPS (DMSO-d₆, 27 °C). (See details about peak assignments in the Experimental Section)

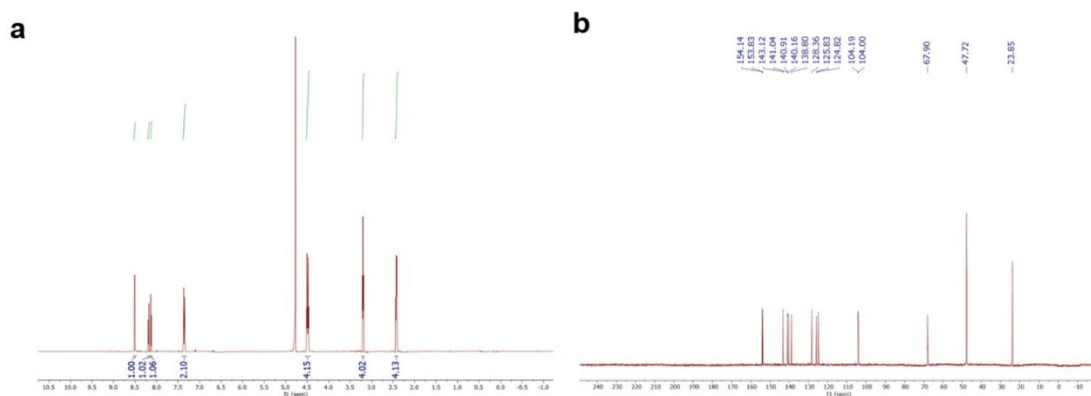


Figure 4.7. (a) ^1H NMR spectrum of the 2,3-SPDPSNa₃ (D₂O, 27 °C). (b) ^{13}C NMR spectrum of the 2,3-SPDPSNa₃ (D₂O, 27 °C). (See details about peak assignments in the Experimental Section)

The electrochemical properties of these phenazine derivatives in neutral aqueous solution were characterized by cyclic voltammograms (CVs) (Figure 4.8b).

HP shows a single two-electron process, with a formal redox potential of -0.40 V vs NHE. By introducing an electron-donating group, a hydroxyl group, DHP shows a lower formal redox potential of -0.62 V vs NHE. Despite the sulfonate group that helps to increase the solubility of DHPS in neutral water (Table 4.1), the DHPS derivative features two pairs of redox peaks with insufficient electrochemical kinetics (peak separation $\Delta E_p > 200$ mV). The two pairs of redox peaks could indicate that the redox reaction proceeds in two successive one-electron processes.^[214] When these phenazine molecules were modified further with short flexible carbon chains terminated with hydrophilic sulfonated groups (Figure 4.8a), their solubility greatly improves in neutral water (Table 4.1). The CVs of PPSNa, 2,3-DPPSNa₂, and 2,3-SPDPSNa₃ all display single two-electron redox reactions, with formal redox potentials of -0.41 , -0.48 , and -0.41 vs NHE, respectively. Therefore, considering the electrochemical properties and solubility of these six phenazine derivatives, the PPSNa derivative was chosen for the following studies.

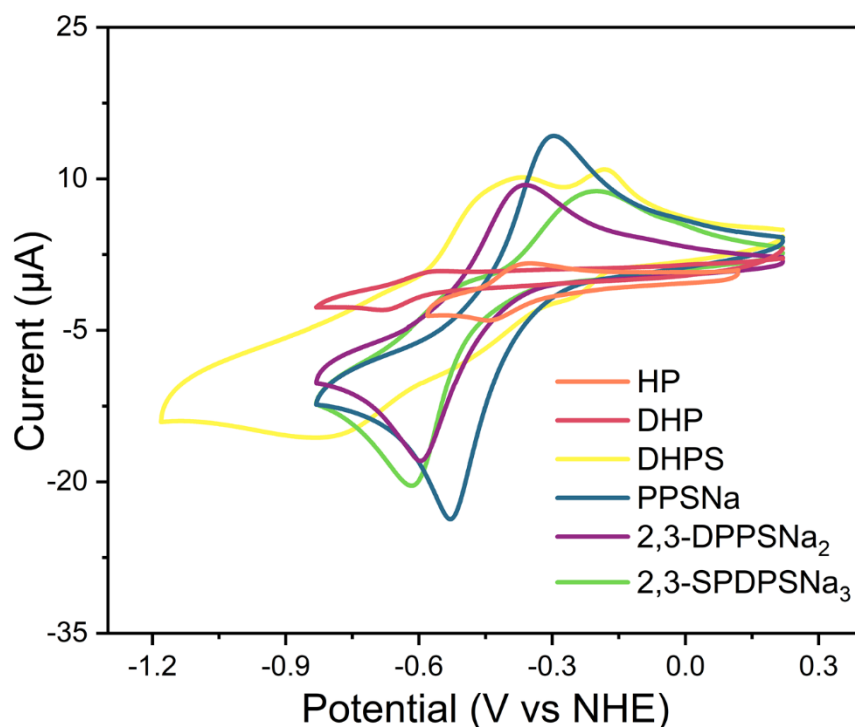


Figure 4.8. (a) The molecular structures of the synthesized phenazine derivatives. (b) CV curves of 2 mM HP, DHP, DHPS, PPSNa, 2,3-DPPSNa₂, and 2,3-SPDPSNa₃ in 0.5 M NaCl (aq) at pH 7 acquired at a scan rate of 50 mV s⁻¹. HP and DHP were measured in a saturated solution at pH 7.

Table 4.1. Solubility of Different Phenazine Derivatives at Nearly Neutral Solution

Substance	Solubility
HP	<0.01M ^a
DHP	<0.01M ^a
DHPS	0.04 M ^b
PPSNa	1.27M
2,3-DPPSNa ₂	0.53M
2,3-SPDPSNa ₃	0.68M

^aDue to the hydroxy group, the solution is weakly acid. Dissolution was achieved in buffer solution (pH 7). ^bThe DHPS was pre-neutralized to a near-neutral pH before dissolving in buffer solution (pH 7) to measure the solubility.

It is well known that the electrochemistry of phenazine involves the transfer of two electrons with a differing number of protons, known as the proton-coupled electron transfer (PCET) reaction (Figure 4.1a), which was reported recently for phenazine-based RFBS.^[78, 79, 214, 215] The redox potential of the PCET redox reaction of phenazine molecules is well known to be pH-dependent over a broad pH range.^{14, 16, 17} To investigate the PCET behaviour of PPSNa, cyclic voltammograms were conducted under various values of pH (Figure 4.9a). PPSNa shows a similar single two-electron redox process. Compared to phenazine derivatives used in basic conditions,^[78, 79] the redox potential of PPSNa is less negative, making its reduced state tend to be less reactive with oxygen. The reduction potential of O₂ vs NHE on a glassy carbon electrode is ~ -0.2 V; thus, the more negative the reduction potential of the phenazine derivative, the more readily it would be expected to react with oxygen.^[216] The Pourbaix diagram was calculated by measuring the redox potential of PPSNa at different pH values, as shown in Figure 4.9b. To our surprise, we found that the redox potential of PPSNa shows pH-independent redox potentials over a pH range of 4 to 10. These results suggest that the redox reaction is not coupled with protons in this pH

region. Above pH 11, however, the redox potential of PPSNa shifted to more negative, with a slope of 58.5 mV/pH, which is consistent with a transfer of $2\text{ H}^+/2\text{ e}^-$ process.

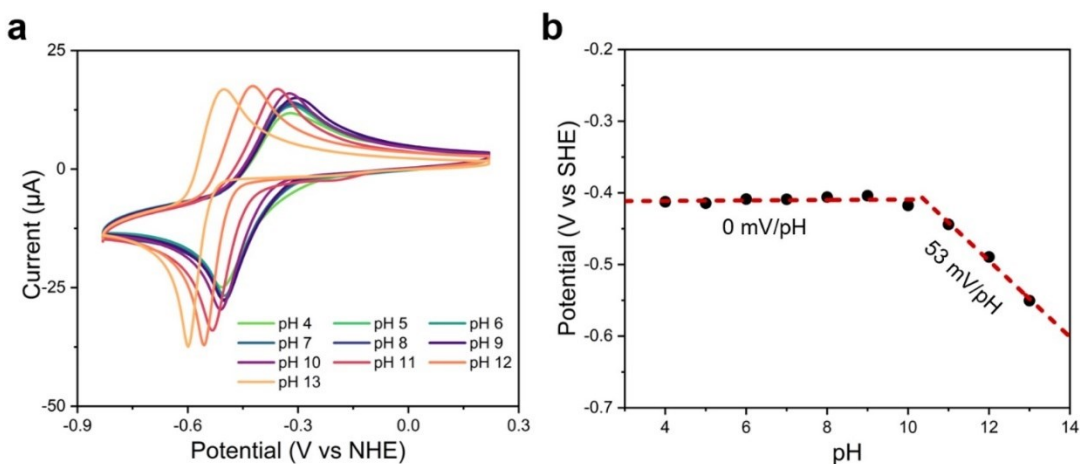


Figure 4.9. (a) Cyclic voltammograms of 2 mM PPSNa as a function of pH in 0.5 M NaCl (aq) at 50 mV s^{-1} . (b) Pourbaix diagram of PPSNa in 0.5 M NaCl (aq).

The electrochemical kinetics of PPSNa were analyzed by linear sweep voltammetry (LSV) using a glassy carbon-equipped rotating disk electrode (RDE). Figure 4.10a shows LSV curves with a scan rate at 5 mV s^{-1} under different rotating speeds, ranging from 300 rpm to 2300 rpm. According to the Levich equation, the diffusion coefficient was calculated to be $2.26 \times 10^{-6}\text{ cm}^2\text{ s}^{-1}$ from the slope of the Levich plot (Figure 4.10b, eq 1 in the Experimental Section in the Supporting Information), which is comparable to other organic and metal complexes used as analytes in RFBs.^[54, 61, 217]

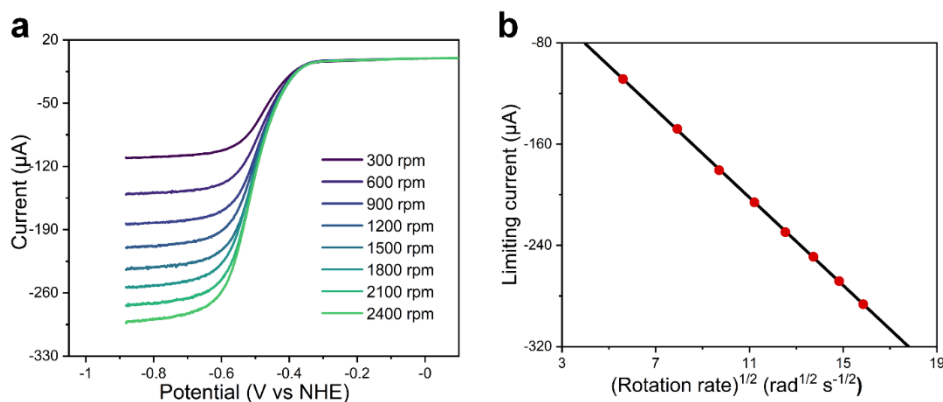


Figure 4.10. (a) Linear sweep voltammograms of 2 mM PPSNa in 0.5 M NaCl (aq); (b) Levich plots of the limiting current vs the square root of rotation rates for PPSNa.

The performance of the PPSNa in a full cell was investigated with PPSNa and $\text{K}_4\text{Fe}(\text{CN})_6$ as the anolyte and catholyte, respectively (see Supporting Information for details). The pH of the cell was adjusted to 7 before starting the test. The electrolyte was pumped into the flow battery comprised of two graphite flow plates and pieces of carbon papers on each side, separated by a Nafion 212 membrane. The proof of the concept cell was cycled at a constant current density of 20 mA cm^{-2} using voltage cutoffs between 0.1 and 1.28 V (Figure 4.11a). In the cycling test, the cell has high and stable Coulombic efficiencies (CE) near 100% (Figure 4.11b). The cell showed a capacity fade rate of 0.011% per cycle, which indicates a very stable cycling performance. Excess catholyte allows us to focus our attention on stability of the anolyte side, thus, the good capacity retention can be ascribed to the high stability of the capacity-limited PPSNa anolyte side.

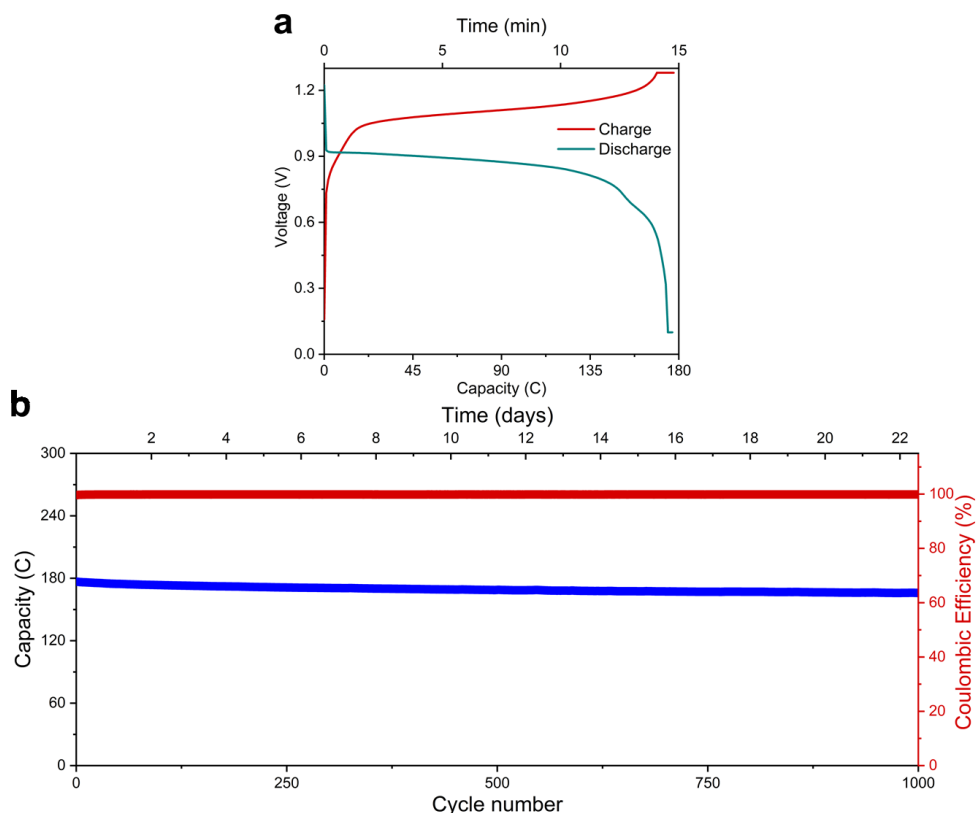
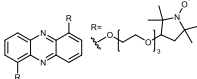
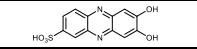
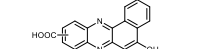
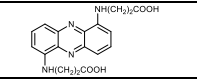
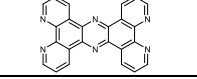
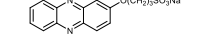


Figure 4.11. (a) Charge–discharge profile of the 0.1 M PPSNa|| $\text{K}_4\text{Fe}(\text{CN})_6$ ARFB in 1 M KCl (aq) at pH 7 at a current density of 20 mA cm^{-2} . (b) Cycling stability and Coulombic efficiency of 0.1 M PPSNa|| $\text{K}_4\text{Fe}(\text{CN})_6$ ARFB in 1 M KCl (aq) at pH 7 at a current density of 20 mA cm^{-2} .

Recently, promising anolytes using phenazine derivatives for aqueous solutions were designed and synthesized and involve the introduction of various functional groups, such as oxyethylenyl, hydroxyl, and carboxylic acids (Table 4.2). Most of these redox-active species showed a two-electron electrochemical reduction process. Nonionizable hydrophilic groups on the phenazine lead to relatively low solubilities, and with carboxylic acids, more basic conditions are required for high solubility.

Table 4.2. Overview of Phenazine Derivatives as Anolyte for Aqueous Organic RFB

Anolyte	Catholyte	Solubility	pH of the cell	Cell Capacity *	No. of Cycles	Capacity Retention per Cycle (%)	Capacity Retention per Day (%)	Ref
	Same molecule as anolyte	-	7	4.5 C	1851	-	-	[190]
	K ₄ Fe(CN) ₆	1.45 M in 1 M NaOH	13	187 C	1500	99.9921	99.07	[78]
				1224 C	500	99.9805	99.32	
	K ₄ Fe(CN) ₆	1.55 M in 1 M KOH	14	932 C	1305	99.9975	99.92	[79]
	K ₄ Fe(CN) ₆	1.005 M in water (pH 12)	12	121 C	330	99.99993	99.9976	[215]
			8	594 C	90	99.999998	99.9985	
	K ₄ Fe(CN) ₆	Insoluble in 1 M KOH	14	1.35 C	1200	99.9975	-	[218]
				2.55 C	1200	99.9980	-	
	K ₄ Fe(CN) ₆	1.27 M in water (pH 7)	7	180 C	1000	99.9937	99.72	This work

*Estimated from the cycling discharge capacity figures in the reference.

The second/double rows in the table indicate the RFBs that have been tested using different concentrations of anolytes, with different cell capacities.

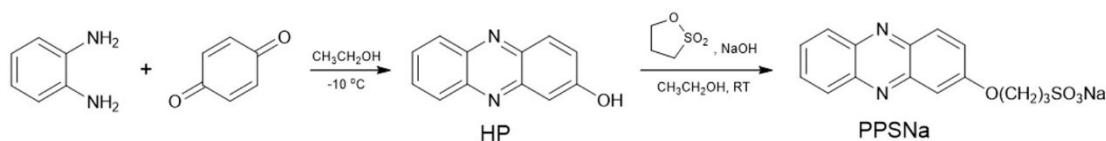
Due to the excellent chemical and electrochemical stability of the phenazine backbone, these cells all demonstrated good cycling stability. Since functionalizing the different positions on the phenazine backbone affects the solubility, redox potential, kinetics, PCET phenomenon, and chemical and electrochemical stability of the phenazine derivatives and their reduced state, it is necessary to design the molecule carefully to achieve high-performance aqueous organic flow batteries.

In summary, the phenazine derivative synthesized in this work exhibits both high solubility and a large range of pH-independent redox potentials, which is an example of a true neutral aqueous redox flow battery when coupled with a ferrocyanide catholyte. The synthesis of phenazine derivatives is convenient and, presumably, scalable. The introduction of sulfonate groups increases solubility in neutral water.

Paired with ferrocyanide catholyte, the PPSNa||K₄Fe(CN)₆ shows excellent cycling stability, which indicates a new pathway to utilize phenazine compounds for neutral ARFBs.

4.3 Experimental Section

Chemicals and instruments. 3,4-Diaminobenzenesulfonic acid was bought from A2B Chem. All other reagents and solvents were purchased from Sigma-Aldrich or Fisher Scientific and used as received. Buffer solution (dihydrogen potassium phosphate-sodium phosphate dibasic, pH 7) was bought from Fisher Chemical. Milli-Q water was purged with Argon for 2 h before use. ¹H and ¹³C NMR spectra were obtained on an Agilent VNMRS (700 MHz, 500 MHz or 400 MHz) spectrometer. UV-vis spectra were recorded using a Perkin Elymer Lambda 1050 UV-Vis-Nir spectrophotometer from 300 to 700 nm. The pH measurements were conducted with a VWR Symphony SB70P pH meter. The mass spectrum was collected using an Agilent 6220 oaTOF in electrospray mode. All cyclic voltammogram curves were taken with a Biologic Science Instruments VSP multichannel potentiostat using EC-Lab software and an Ag/AgCl electrode as reference electrode (soaked in 3 M NaCl).

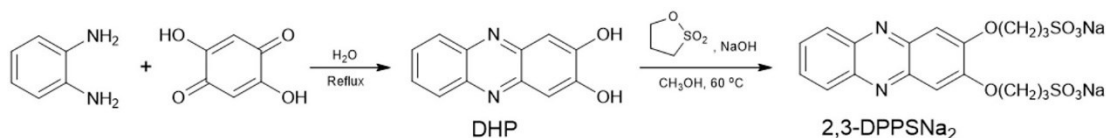


Synthesis of 2-Hydroxyphenazine (HP). *o*-Diaminobenzene (4.32 g, 40 mmol) was added slowly into a solution of benzoquinone (4.32 g, 40 mmol) in 400 mL anhydrous ethanol solution at 10 °C under Ar. After 2.5 h, the mixture was filtered and the filtrate was concentrated to 30 mL under reduced pressure. Then, 200 mL of water were added, and the suspension was filtered. The residue was purified further by column chromatography (silica gel, ethyl acetate: n-hexane = 30:70). This yield was about 67%. ¹H NMR (DMSO-d₆, 699.766 MHz, 27 °C): δ (in ppm), 10.89 (s, 1H), 8.17 (dd, 1H), 8.12(m, 2H), 7.88(m, 1H), 7.82(m, 1H), 7.58(dd, 1H), 7.34(d, 1H). ¹³C NMR (DMSO-d₆, 125.689 MHz, 27 °C): δ (in ppm), 160.04, 145.25, 143.38,

141.39, 139.96, 131.27, 131.13, 129.81, 129.40, 129.01, 126.96, 107.50. ESI-MS, m/z: 195 [HP - H]⁻.

Synthesis of sodium 3-(phenazin-2-yloxy)propane-1-sulfonate (PPSNa).

1,3-Propanesultone (1.87 g, 15.3 mmol) was added to the solution of 2-hydroxyphenazine (3 g, 15.3 mmol) and sodium hydroxide (0.612 g, 15.3 mmol) in 90 mL anhydrous ethanol solution under Ar. The reaction mixture was stirred overnight, and the precipitate was collected and washed with ethanol. The residue was dried under vacuum, and the yield is about 90%. ¹H NMR (DMSO-d₆, 699.766 MHz, 27 °C): δ (in ppm), 8.21 (dd, 1H), 8.18(dd, 1H), 8.13(dd, 1H), 7.92(m, 1H), 7.86(m, 1H), 7.64(dd, 1H), 7.47(d, 1H), 4.35(t, 2H), 2.63(t, 2H), 2.13(M, 2H). ¹³C NMR (DMSO-d₆, 125.686 MHz, 27 °C): δ (in ppm), 160.66, 145.06, 143.22, 141.63, 140.44, 131.24, 130.95, 129.82, 129.74, 129.06, 127.12, 105.53, 68.12, 48.27, 25.44. ESI-MS, m/z: 317 [PPSNa - Na]⁻.



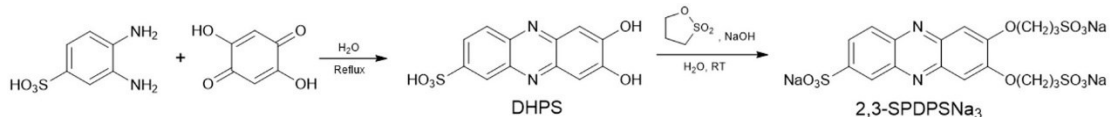
Synthesis of 2,3-dihydroxyphenazine (DHP).

2,5-Dihydroxy-1,4-benzoquinone (7.08 g, 52 mmol) and 1,2-phenylenediamine (5.06 g, 46.8 mmol) were added to 390 mL water under Ar. The reaction mixture was refluxed overnight, and the suspension was filtered, washed with water, and dried under vacuum. The yield is about 95%. ¹H NMR (DMSO-d₆, 699.766 MHz, 27 °C): δ (in ppm), 10.91(s, 2H), 8.05(s, 2H), 7.73(s, 2H), 7.29(s, 2H). ¹³C NMR (DMSO-d₆, 125.686 MHz, 27 °C): δ (in ppm), 153.80, 141.92, 141.32, 128.88, 107.61. ESI-MS, m/z: 211 [DHP - H]⁻.

Synthesis of sodium 3,3'-(phenazine-2,3-diylbis(oxy))bis(propane-1-sulfonate) (2,3-DPPSNa₂).

1,3-Propanesultone (8.06 g, 66 mmol) was added to the solution of 2-hydroxyphenazine (7 g, 33 mmol) and sodium hydroxide (2.64 g, 66 mmol) in 110 mL anhydrous methanol solution under Ar. The solution was heated at 60 °C overnight. The precipitate was collected, washed with methanol, and dried under vacuum. The yield is about 65%. ¹H NMR (D₂O, 699.764 MHz, 27 °C): δ (in ppm), 7.86–7.83(m, 2H), 7.81(m, 2H), 6.72(s, 2H), 4.19(t, 4H), 3.18(t, 4H), 2.35(m,

4H). ^{13}C NMR (D_2O , 100.540 MHz, 27 °C): δ (in ppm), 152.57, 139.53, 139.18, 130.05, 127.09, 103.60, 67.73, 48.19, 24.23. ESI-MS, m/z : 227 $[\text{2,3-DPPSNa}_2 - 2\text{Na}]^-$, 455 $[\text{2,3-DPPSNa}_2 - 2\text{Na} + \text{H}]^-$, 477 $[\text{2,3-DPPSNa}_2 - \text{Na}]^-$.



Synthesis of 7,8-dihydroxyphenazine-2-sulfonic acid (DHPS). 2,5-Dihydroxy-1,4-benzoquinone (24.51 g, 180 mmol) was added to a flask with 390 mL of water under Ar. When it warmed to 107 °C, 3,4-diaminobenzenesulfonic acid (33.88g 180 mmol) was added over a 6 min period. After the mixture was fluxed overnight and cooled to room temperature, 600 mL of acetone were added, and the precipitate was collected, washed with water and acetone, and dried under vacuum. The yield is about 96%. ^1H NMR (DMSO-d_6 , 399.796 MHz, 27 °C): δ (in ppm), 8.23(d, 1H), 8.06(d, 1H), 7.97(dd, 1H), 7.30 (s, 1H), 7.29(s, 1H). ^{13}C NMR (DMSO-d_6 , 100.586 MHz, 27 °C): δ (in ppm), 157.82, 157.06, 149.85, 140.72, 138.39, 137.60, 135.65, 128.80, 126.60, 121.25, 105.79, 104.60. ESI-MS, m/z : 291 $[\text{DHPS-H}]^-$.

Synthesis of sodium 3,3'-((7-sulfonatophenazine-2,3-diyl)bis(oxy))bis(propylsulfonate) (2,3-SPDPSNa₃). 1,3-Propanesultone (6.40 g, 52.4 mmol) was added to the solution of 2-hydroxyphenazine (7.63 g, 26.1 mmol) and sodium hydroxide (3.14 g, 78.5 mmol) in 20 mL water under Ar. The solution was stirred overnight, then the mixture was poured into 500 mL methanol. The precipitate was collected, washed with methanol, and dried under vacuum. The yield is about 70%. ^1H NMR (D_2O , 699.764 MHz, 27 °C): δ (in ppm), 8.51 (s, 1H), 8.19 (d, 1H), 8.13 (dd, 1H), 7.36 (d, 2H), 4.49 (dt, 4H), 3.20 (m, 4H), 2.42 (dt, 4H). ^{13}C NMR (D_2O , 125.686 MHz, 27 °C): δ (in ppm), 154.14, 153.83, 143.12, 141.04, 140.91, 140.16, 138.80, 128.36, 125.83, 124.82, 104.19, 104, 67.9, 47.72, 23.85. ESI-MS, m/z : 177 $[\text{2,3-SPDPSNa}_3 - 3\text{Na}]^{-3}$, 267 $[\text{2,3-SPDPSNa}_3 - 3\text{Na} + \text{H}]^{-2}$, 278 $[\text{2,3-SPDPSNa}_3 - 2\text{Na}]^{-2}$, 535 $[\text{2,3-SPDPSNa}_3 - 3\text{Na} + 2\text{H}]^-$.

Solubility studies. Samples were added to a small portion of water or buffer solution until no further solid could be dissolved. The saturated solution was obtained

by filtering the suspension through an 0.2 μm PTFE syringe filter. Then, the saturated solution was diluted by a known amount and measured with PerkinElmer Lambda 1050 UV-Vis-Nir spectrophotometer. Precalibrated absorbance-concentration curves obtained from standard solution were used to calculate the solubility. The results are shown in Figure 4.12 to Figure 4.15.

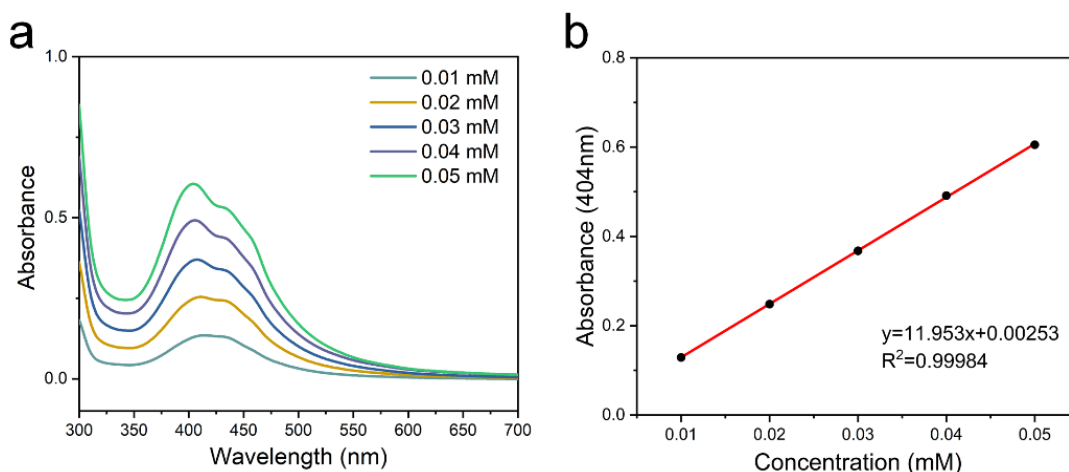


Figure 4.12. (a) UV-vis spectra of DHPS in buffer solution (pH 7) at different concentrations. (b) Absorbance at 404 nm as a function of concentration.

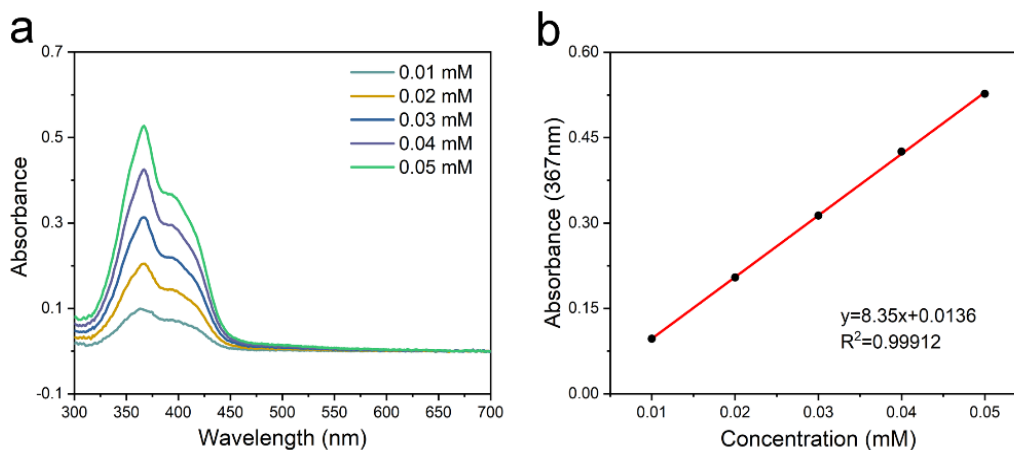


Figure 4.13. (a) UV-vis spectra of PPSNa in water at different concentrations (pH 7). (b) Absorbance at 367 nm as a function of concentration.

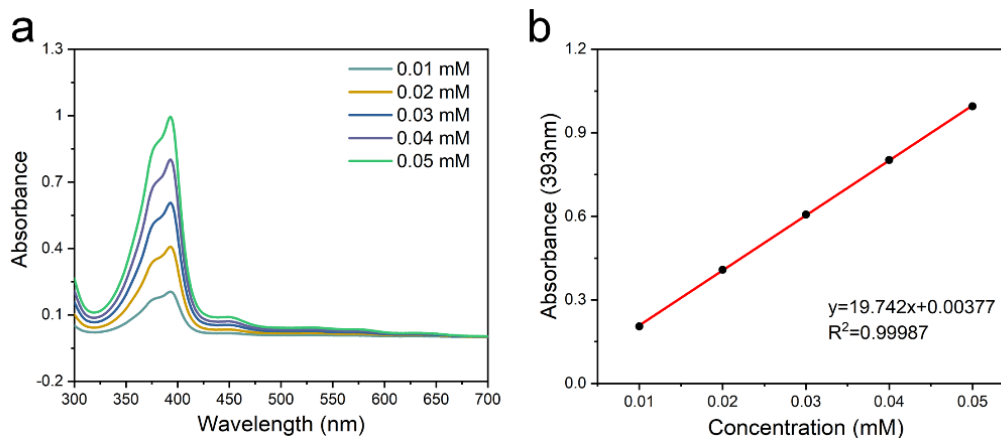


Figure 4.14. (a) UV-vis spectra of 2,3-DPPSN₂ in water at different concentrations (pH 7). (b) Absorbance at 393 nm as a function of concentration.

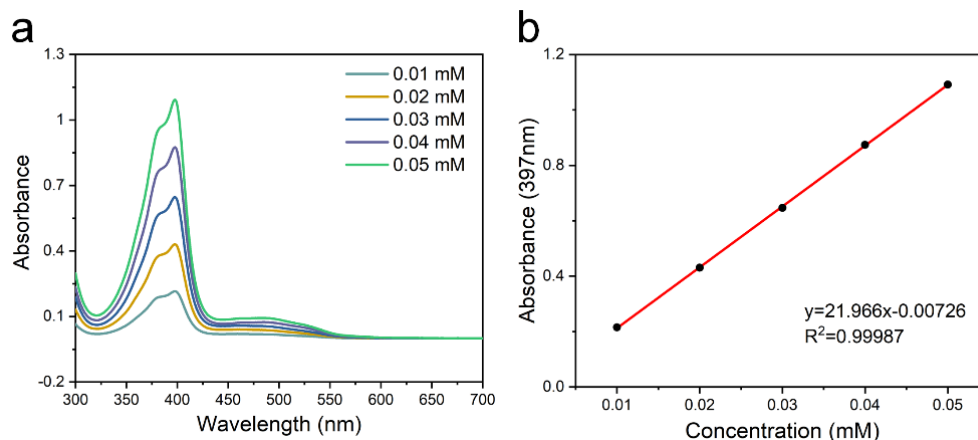


Figure 4.15. (a) UV-vis spectra of 2,3-SPDPSNa₃ in water at different concentrations (pH is 7). (b) Absorbance at 397 nm as a function of concentration.

Electrochemical tests. Rotating disk electrode (RDE) and cyclic voltammetry (CV) were conducted with a Biologic Science Instruments VSP multichannel potentiostat using a platinum counter electrode, Ag/AgCl reference electrode, and glassy carbon working electrode (5 mm for RDE test and 3 mm for CV test). The glass carbon working electrode was polished before use. All the electrochemical tests were performed in 0.5 M NaCl solution under Ar. CV was recorded with a scan speed of 50 mV/s, unless otherwise specified. The RDE experiments were carried out using a Pine Instrument ASR rotator equipped with a 5 mm glassy carbon working electrode. Linear sweep voltammetry studies were conducted at a rate of 5 mV/s with a working electrode

rotating at a certain speed. The limiting current $i_{l,a}$ was recorded at -0.74 V. The Levich equation was used to calculate the diffusion coefficient D .

$$i_{l,a} = \left(0.62nFAD^{\frac{2}{3}}\nu^{-\frac{1}{6}}C_o\right)\sqrt{\omega} \quad 4.1$$

where n is the transferred electron number; F is the Faraday's constant; A is the electrode area; ν is the kinematic viscosity (0.01024 cm²/s for 0.5 M NaCl), and C_o is the concentration of PPSNa.

Full cell performance. The flow battery was assembled with a zero-gap cell. Pieces of carbon papers (Sigracet SGL 29AA) were preheated in the air at 400 °C for 24 h on each side and pressed with POCO graphite flow plates (serpentine flow pattern) in combination with a 10 cm² geometric surface area, separated by the Nafion 212 membrane. The Nafion membrane was pretreated first in boiled 3% H₂O₂ solution for 1 h and then heated in 1 M H₂SO₄ solution for another 1 h, washed with deionized water, and finally soaked in 2 M NaCl for further use. Two glass reservoirs containing 10 mL 0.1 M of PPSNa and vitamin B3 in 1 M KCl and 60 ml 0.1 M K₄Fe(CN)₆ and 0.02 M K₃Fe(CN)₆ in 1 M KCl were used as anolyte and catholyte, respectively. When employed in galvanostatic charging/discharging, the cutoff voltage is between 0.01 and 1.28 V. To fully charge and discharge the cell, once the predefined potential cutoffs were reached, the cell was held on that voltage until the charging/discharging current had decreased to 1 mA cm⁻². A peristaltic pump (Cole-Parmer Masterflex L/S) was chosen to pump the anolyte and catholyte into the center cell through viton tubing at a rate of 60 ml/min. Once the flow cell was assembled, the two reservoir were purged with argon, and the cell was placed in an Ar-filled glove bag.

Chapter 5

Thesis Summary and Outlook

5.1 Thesis Summary

The main goal of this thesis was to develop new electrochemical analytical methods and redox-active molecules and, subsequently, to determine and understand their chemical and electrochemical properties for the next generation of redox flow batteries. The relationship between the structure and properties of the molecules and the performance of the flow batteries also have been analyzed and discussed. In this final chapter, summaries of each chapters and perspectives on future research are provided in the following sections.

5.1.1 Chapter 1

Chapter 1 provided a short background of redox flow batteries and their applications in energy storage systems. The chapter began with a discussion of the current challenges facing energy storage of intermittent renewable energy as well as the advantages of redox flow batteries for large-scale (grid-scale) stationary energy storage. Next, the general working principles, performance criteria, including capacity, energy/power density, coulombic/energy efficiency and cycle life, along with research and development of different materials for electrolytes, membranes, and electrodes, were introduced and reviewed. As a crucial factor in determining the performance of the flow batteries, important physicochemical parameters of the electrolyte and their influence on the full cell performance were analyzed. Some typical ex-situ and in-situ electrochemical analytical methods to probe electrochemical properties of electrolyte were introduced. Finally, the design principles and guidelines to improve parameters for high-performance flow batteries were outlined.

5.1.2 Chapter 2

Based on simulation analysis, Chapter 2 firstly reviewed the advantages and limitations of various methods that have been developed to evaluate the kinetics and to acquire the kinetic parameters in flow batteries quantitatively. By introducing the Levich equation

to the current-overpotential equation for quasireversible-type systems, a new equation was obtained to determine rate constants and diffusion coefficients for both reduced and oxidized species by simply using a rotating disk electrode. Next, effects of electrochemical kinetics parameters on the performance of the flow batteries were simulated and analyzed. Regardless of diffusion coefficients, all redox systems, whether they are electrochemically reversible, quasireversible, or irreversible, can be analyzed for their performance for RFBs. Finally, a new and overarching electrochemical protocol was outlined to enable future researchers to define the kinetics of their RFBs systems.

5.1.3 Chapter 3

In Chapter 3, we reported the synthesis, characterization, and testing of water-soluble 2,6-bis[1-(4-carboxyphenylimino)ethyl]pyridine cobalt dichloride, termed BCPIP-Co(II), as an analyte for symmetric aqueous RFBs. The four appended -COOH groups on the ligand periphery help to increase the water solubility from virtually insoluble to more than 0.5 M (pH > 6.3). The complex displays BCPIP-Co(II-III) and BCPIP-Co(II-I) reversible redox couples within the water splitting window, with fast kinetics. Due to deprotonation and ionization of the carboxylic acid moieties, the overall charge of the complex can vary from +3 to -3, affecting the donor character of the ligand and resulting in pH-switchable potentials up to 0.69 and -0.45 V vs NHE for catholyte [BCPIP-Co(II)/Co(III)] and anolyte [BCPIP-Co(II)/Co(I)], respectively. The symmetric aqueous RFB demonstrate high capacity retention of 99.9% per cycle over 100 cycles shed light on a symmetric aqueous RFB based on metal-coordination complexes.

5.1.4 Chapter 4

In Chapter 4, we reported the synthesis and characterization a series of phenazine derivatives as promising redox-active compounds for neutral aqueous redox flow batteries. We systematically studied the physiochemical and electrochemical properties of these materials. The electrochemical performance of PPSNa at different pH values also was investigated; it exhibited surprising pH-independent behavior from pH 4 to pH 10. When coupled with ferrocyanide as a catholyte, the first phenazine based neutral

aqueous redox flow battery showed good capacity retention of 99.999% per cycle over 400, with a stable coulombic efficiency near 100%. These results provide a means to modify phenazine derivatives for future neutral aqueous redox flow batteries with organic active materials.

5.2 Future work

5.2.1 Evaluation of Phenazine-based Anolyte for Redox Flow Batteries: Impact of Function Group Structure on Solubility and Electrochemistry

The phenazine moiety is capable of undergoing stable two-electron reversible redox reactions.^[211] Inspired by its vast structural diversity (thousands of compounds have been prepared, mainly for biological research) and various synthetic routes,^[210] their derivatives have started to be examined as electrolytes in RFBs.^[78, 212, 213]

In Chapter 4, we designed a phenazine-based electrolyte functionalized with hydrophilic substituents to apply in both aqueous and organic RFB systems. Phenazine with hydroxyl groups has been proven to have good solubility only in strongly basic solutions.^[78, 79] To avoid the use of basic conditions, hydroxyl-terminated phenazine was prepared, reacted with 1,3-propanesultone, and covalently bound to a number of hydrophilic substituents. For instance, a hydrophilic sulfonate group with a short chain was incorporated to enhance solubility in the pH-neutral aqueous electrolyte by asymmetric charge distribution^[78] and frustrated crystallization.^[66] The use of pH neutral solutions has the added benefit of mitigating problems of corrosion that occur under strong acid/base conditions. However, as shown in Figure 5.1, there are many variables with respect to the phenazine derivatives, including various functional groups (e.g., carboxylic, phosphonic, ammonium and PEG) and different positions on the phenazine core, as well as chain length and counter ions (such as ammonium, tetra-hydroxyethyl ammonium, and tetra-hydroxymethyl phosphonium that are non-chelatable and very hygroscopic) with respect to the functional groups R₁ to R₈, and others that can be slotted in synthetically and optimized. Different functional groups with various chain length under different positions of phenazine will affect the solubility, redox potential, and stability of the phenazine. Studying these effects could

lead to a new class of organic electrolytes for high performance RFBs in a neutral aqueous system.

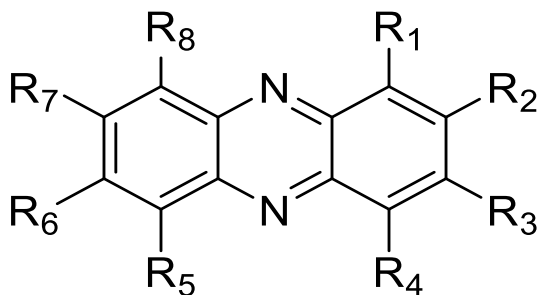


Figure 5.1. Molecular structure of phenazine derivatives.

5.2.2 Stability and Mechanism of Capacity Decay of Phenazine-based Aqueous Flow Batteries

Redox flow batteries based on phenazine-bearing electrolytes have emerged as candidates for aqueous flow batteries. Organic redox-active compounds are prone to decomposition, which can lead to continuous capacity loss during cycling. To increase the cycling stability of phenazine-based aqueous flow batteries further, it is of importance to investigate their stability and any possible decomposition pathways. Many studies have proposed different pathways for organic molecular decomposition, such as nucleophilic/electrophilic substitution,^[58, 128, 219] Michael addition,^[81, 220] ring-opening,^[74] dimerization,^[221] and disproportionation.^[70, 222] However, to the best of our knowledge, none of them studied the chemical and electrochemical stability and possible decomposition pathways of phenazine in aqueous flow batteries. The use of analytical techniques, such as NMR, HPLC, LC-MS, to monitor and analyze the composition of the electrolyte during charging and discharging can help to unveil decomposition pathways and provide insights for further modification through molecular engineering.

5.2.3 Air Stable Aqueous Redox Flow Batteries

One of the reasons that could cause the decrease of the capacity retention is oxygen permeation. For example, methyl viologen dichloride (MV) usually is used as an anolyte in aqueous organic RFBs. During charging, the dication MV^{2+} is reduced to the radical $MV^{\bullet+}$. Like most organic radicals, it is sensitive to the oxygen and can be

oxidized back to MV^{2+} , which leads to the decrease of the state of charge of the anolyte. The oxygen also will be reduced to OH^- , leading to an increase of the pH. Another example is ferrocene derivatives, which are used widely as catholytes in RFBs due to their excellent chemical and electrochemical stability in acidic-to-neutral water. However, its oxidized form (ferrocenium) decomposes in the presence of oxygen. The decomposition mechanism involves an unstable dimer of two ferrocenium species bridged by an oxygen. Therefore, the design and preparation of redox-active molecules with air-stable properties could help to increase the cycle life, simplify the deployment, and lower the system cost.

Ohsaka et al. studied the catalytic reduction of O_2 by pyrazine derivatives. They found that the voltammograms of phenazine are independent with respect to the absence or presence of oxygen (Figure 5.2, curves 5 and 5') in DMF [20% (v/v)] aqueous solutions, indicating that the reduced form of phenazine does not react with oxygen, as shown in Figure 5.2^[214] On the basis of this result, it would be interesting to investigate an aqueous organic RFB using a phenazine derivative as the anolyte and ferrocyanide as the catholyte and to study its performance in the presence and absence of air.

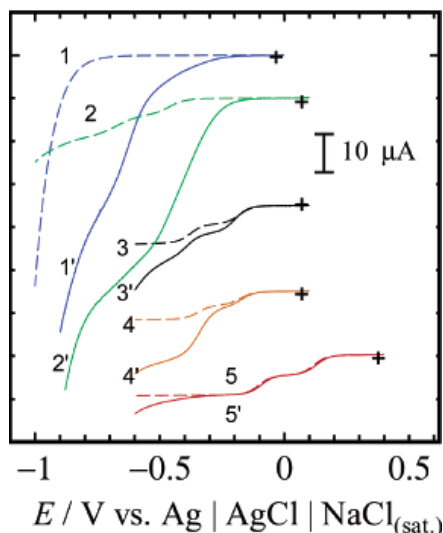


Figure 5.2. Linear sweep voltammograms of 0.132 mM of (2) 2,3,5,6-tetramethylpyrazine, (3) 2,3-dimethylquinoxaline, (4) 2,3-diphenyl -quinoxaline, (5) 0.132 mM phenazine at 1600 rpm of RDE in 0.08 M $NaClO_4$ and $HClO_4$ DMF [20% (v/v)]-water solutions. (---) and (-) represent N_2 and air-saturated solution, respectively. Reprinted with permission from 214. Copyright (2004) American Chemical Society.

5.2.4 All Phenazine Non-aqueous Redox Flow Battery

There are only a few examples of RFBs that use phenazine as either a catholyte or anolyte in flow batteries. [78, 79, 190, 212] Among them, most focus on aqueous RFBs, while little attention has been paid to non-aqueous systems. [212] Recently, Andreas et al. performed a systematic computational investigation on various phenazine derivatives in non-aqueous systems via high-throughput DFT modeling. [223] They found that the redox potentials of phenazine compounds should be modifiable from -0.65 V to $+2.25$ V compared with the parent phenazine by attaching different electron-donating or -withdrawing groups, as shown in Figure 5.3. Based on previous studies on phenazine derivatives in aqueous systems, functionalized phenazine with electro-donating groups (for the anolyte) and electro-withdrawing groups (for the catholyte) can be studied to screen for non-aqueous redox flow batteries.

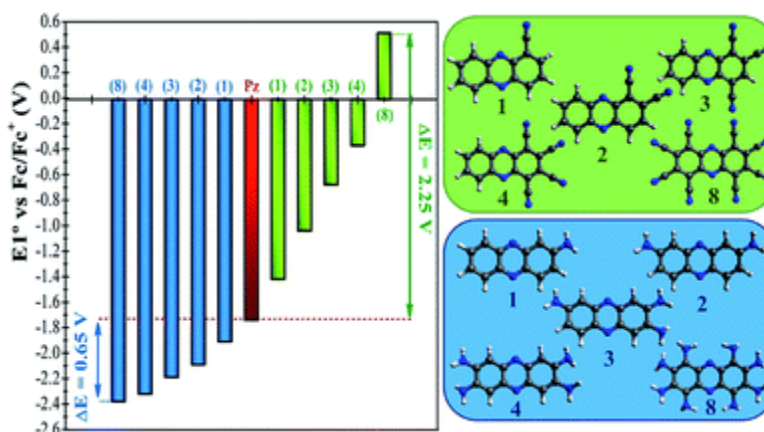


Figure 5.3. Redox potential (vs Fc/Fc^+) of phenazine functionalized with different number of cyano groups (green) and amino groups (blue). For reproduction of material from all other RSC journals: 223 Copyright (2020) Royal Society of Chemistry.

5.2.5 Investigate structure of BCPIP-Co(I) and possible absorption mechanism to develop symmetric ARFBs with high capacity

Due to the weak interaction between the BCPIP-Co(I) complex with the electrode and membrane surfaces, good RFB performance is only observed at 1 mM (aq) concentration. Therefore, by electrochemically or chemically reducing BCPIP-Co(II) to BCPIP-Co(I), a full characterization could be initiated, including the use of UV-visible spectroscopy, NMR, XPS or single-crystal XRD to investigate the structure of BCPIP-Co(I). Could adsorption be avoided via modulating the structure of the

molecule? If so, a new molecular engineering strategy could be applied to achieve high-capacity symmetric ARFBs. Then, comprehensive electrochemical studies such high concentration cycling and polarization experiments could be conducted.

References

- [1] DOE-EIA International Energy Outlook 2019. <https://www.eia.gov/outlooks/ieo/pdf/ieo2019.pdf>.
- [2] Soloveichik, G. L., Flow Batteries: Current Status and Trends. *Chem. Rev.* **2015**, *115* (20), 11533-11558.
- [3] Winsberg, J.; Hagemann, T.; Janoschka, T.; Hager, M. D.; Schubert, U. S., Redox-Flow Batteries: From Metals to Organic Redox-Active Materials. *Angew. Chem., Int. Ed.* **2017**, *56* (3), 686-711.
- [4] Rastler, D., *Electricity energy storage technology options: a white paper primer on applications, costs and benefits*. Electric Power Research Institute: 2010.
- [5] Ding, Y.; Zhang, C.; Zhang, L.; Zhou, Y.; Yu, G., Pathways to Widespread Applications: Development of Redox Flow Batteries Based on New Chemistries. *Chem* **2019**, *5* (8), 1964-1987.
- [6] Gür, T. M., Review of electrical energy storage technologies, materials and systems: challenges and prospects for large-scale grid storage. *Energy & Environmental Science* **2018**, *11* (10), 2696-2767.
- [7] Rapier, R., Why Vanadium Flow Batteries May Be The Future Of Utility-Scale Energy Storage. *Forbes* 2020.
- [8] Argyrou, M. C.; Christodoulides, P.; Kalogirou, S. A., Energy storage for electricity generation and related processes: Technologies appraisal and grid scale applications. *Renewable and Sustainable Energy Reviews* **2018**, *94*, 804-821.
- [9] Yang, Z.; Zhang, J.; Kintner-Meyer, M. C.; Lu, X.; Choi, D.; Lemmon, J. P.; Liu, J., Electrochemical energy storage for green grid. *Chem Rev* **2011**, *111* (5), 3577-613.
- [10] Wang, H.; Sayed, S. Y.; Luber, E. J.; Olsen, B. C.; Shirurkar, S. M.; Venkatakrishnan, S.; Tefashe, U. M.; Farquhar, A. K.; Smotkin, E. S.; McCreery, R. L.; Buriak, J. M., Redox Flow Batteries: How to Determine Electrochemical Kinetic Parameters. *ACS Nano* **2020**, *14* (3), 2575-2584.
- [11] Ke, X.; Prahl, J. M.; Alexander, J. I. D.; Wainright, J. S.; Zawodzinski, T. A.; Savinell, R. F., Rechargeable redox flow batteries: flow fields, stacks and design considerations. *Chem Soc Rev* **2018**, *47* (23), 8721-8743.
- [12] Tong, L.; Goulet, M.-A.; Tabor, D. P.; Kerr, E. F.; De Porcellinis, D.; Fell, E. M.; Aspuru-Guzik, A.; Gordon, R. G.; Aziz, M. J., Molecular Engineering of an Alkaline Naphthoquinone Flow Battery. *ACS Energy Lett.* **2019**, *4* (8), 1880-1887.
- [13] Ji, Y.; Goulet, M. A.; Pollack, D. A.; Kwabi, D. G.; Jin, S.; Porcellinis, D.; Kerr, E. F.; Gordon, R. G.; Aziz, M. J., A Phosphonate-Functionalized Quinone Redox Flow Battery at Near-Neutral pH with Record Capacity Retention Rate. *Adv. Energy Mater.* **2019**, *9* (12).
- [14] Luo, J.; Hu, B.; Hu, M.; Zhao, Y.; Liu, T. L., Status and Prospects of Organic Redox Flow Batteries toward Sustainable Energy Storage. *ACS Energy Lett.* **2019**, *4* (9), 2220-2240.
- [15] Dinesh, A.; Olivera, S.; Venkatesh, K.; Santosh, M. S.; Priya, M. G.; Inamuddin; Asiri, A. M.; Muralidhara, H. B., Iron-based flow batteries to store renewable energies. *Environmental Chemistry Letters* **2018**.
- [16] Singh, P., Application of non-aqueous solvents to batteries. *J. Power Sources* **1984**, *11* (1), 135-142.

- [17] Matsuda, Y.; Tanaka, K.; Okada, M.; Takasu, Y.; Morita, M.; Matsumura-Inoue, T., A rechargeable redox battery utilizing ruthenium complexes with non-aqueous organic electrolyte. *Journal of Applied Electrochemistry* **1988**, *18* (6), 909-914.
- [18] Yamamura, T.; Shiokawa, Y.; Yamana, H.; Moriyama, H., Electrochemical investigation of uranium β -diketonates for all-uranium redox flow battery. *Electrochim. Acta* **2002**, *48* (1), 43-50.
- [19] Liu, Q.; Sleightholme, A. E. S.; Shinkle, A. A.; Li, Y.; Thompson, L. T., Non-aqueous vanadium acetylacetonate electrolyte for redox flow batteries. *Electrochemistry Communications* **2009**, *11* (12), 2312-2315.
- [20] Noack, J.; Roznyatovskaya, N.; Herr, T.; Fischer, P., The Chemistry of Redox-Flow Batteries. *Angew. Chem., Int. Ed.* **2015**, *54* (34), 9776-809.
- [21] Gong, K.; Fang, Q.; Gu, S.; Li, S. F. Y.; Yan, Y., Nonaqueous redox-flow batteries: organic solvents, supporting electrolytes, and redox pairs. *Energy & Environmental Science* **2015**, *8* (12), 3515-3530.
- [22] Darling, R. M.; Gallagher, K. G.; Kowalski, J. A.; Ha, S.; Brushett, F. R., Pathways to low-cost electrochemical energy storage: a comparison of aqueous and nonaqueous flow batteries. *Energy & Environmental Science* **2014**, *7* (11), 3459-3477.
- [23] Liu, W.; Lu, W.; Zhang, H.; Li, X., Aqueous Flow Batteries: Research and Development. *Chemistry* **2018**.
- [24] Kangro, W. Method for storing electrical energy. DE914264C, 1949.
- [25] Hagedorn, N. H. *NASA redox storage system development project. Final Report*; National Aeronautics and Space Administration, Cleveland, OH (USA). Lewis ...: 1984.
- [26] Winsberg, J.; Janoschka, T.; Morgenstern, S.; Hagemann, T.; Muench, S.; Hauffman, G.; Gohy, J. F.; Hager, M. D.; Schubert, U. S., Poly(TEMPO)/Zinc Hybrid-Flow Battery: A Novel, "Green," High Voltage, and Safe Energy Storage System. *Adv Mater* **2016**, *28* (11), 2238-43.
- [27] Huang, Z.; Zhang, P.; Gao, X.; Henkensmeier, D.; Passerini, S.; Chen, R., Unlocking Simultaneously the Temperature and Electrochemical Windows of Aqueous Phthalocyanine Electrolytes. *ACS Applied Energy Materials* **2019**, *2* (5), 3773-3779.
- [28] Sun, N.; Lu, F.; Yu, Y.; Su, L.; Gao, X.; Zheng, L., Alkaline Double-Network Hydrogels with High Conductivities, Superior Mechanical Performances, and Antifreezing Properties for Solid-State Zinc-Air Batteries. *ACS Applied Materials & Interfaces* **2020**, *12* (10), 11778-11788.
- [29] Vellacheri, R.; Al-Haddad, A.; Zhao, H.; Wang, W.; Wang, C.; Lei, Y., High performance supercapacitor for efficient energy storage under extreme environmental temperatures. *Nano Energy* **2014**, *8*, 231-237.
- [30] Dunn, B.; Kamath, H.; Tarascon, J.-M., Electrical Energy Storage for the Grid: A Battery of Choices. *Science* **2011**, *334* (6058), 928-935.
- [31] Park, M.; Ryu, J.; Wang, W.; Cho, J., Material design and engineering of next-generation flow-battery technologies. *Nat. Rev. Mater.* **2016**, *2* (1), 16080.
- [32] Wei, X.; Pan, W.; Duan, W.; Hollas, A.; Yang, Z.; Li, B.; Nie, Z.; Liu, J.; Reed, D.; Wang, W.; Sprenkle, V., Materials and Systems for Organic Redox Flow Batteries: Status and Challenges. *ACS Energy Lett.* **2017**, *2* (9), 2187-2204.
- [33] Tan, R.; Wang, A.; Malpass-Evans, R.; Williams, R.; Zhao, E. W.; Liu, T.; Ye, C.; Zhou, X.; Darwich, B. P.; Fan, Z.; Turcani, L.; Jackson, E.; Chen, L.; Chong, S. Y.; Li, T.; Jelfs, K. E.; Cooper, A. I.; Brandon, N. P.; Grey, C. P.; McKeown, N. B.; Song, Q., Hydrophilic

- microporous membranes for selective ion separation and flow-battery energy storage. *Nat Mater* **2020**, *19* (2), 195-202.
- [34] Cathro, K. J., Performance of zinc/bromine cells having a propionitrile electrolyte. *J. Power Sources* **1988**, *23* (4), 365-383.
- [35] Nikiforidis, G.; Berlouis, L.; Hall, D.; Hodgson, D., Charge/discharge cycles on Pt and Pt-Ir based electrodes for the positive side of the Zinc-Cerium hybrid redox flow battery. *Electrochim. Acta* **2014**, *125*, 176-182.
- [36] Cheng, J.; Zhang, L.; Yang, Y.-S.; Wen, Y.-H.; Cao, G.-P.; Wang, X.-D., Preliminary study of single flow zinc–nickel battery. *Electrochemistry Communications* **2007**, *9* (11), 2639-2642.
- [37] Hruska, L. W., Investigation of Factors Affecting Performance of the Iron-Redox Battery. *J. Electrochem. Soc.* **1981**, *128* (1), 18.
- [38] Cheng, J.; Zhang, H. M.; Wen, Y. H.; Cao, G. P.; Yang, Y. S. In *Study on a Cd-Fe Redox Flow Battery in a Sulphuric Acid Electrolyte*, Advanced Materials Research, Trans Tech Publ: 2012; pp 1519-1523.
- [39] Hazza, A.; Pletcher, D.; Wills, R., A novel flow battery: A lead acid battery based on an electrolyte with soluble lead(ii) Part I. Preliminary studies. *Physical Chemistry Chemical Physics* **2004**, *6* (8), 1773-1778.
- [40] Savinell, R. F., Discharge Characteristics of a Soluble Iron-Titanium Battery System. *J. Electrochem. Soc.* **1979**, *126* (3), 357.
- [41] Sanz, L.; Lloyd, D.; Magdalena, E.; Palma, J.; Kontturi, K., Description and performance of a novel aqueous all-copper redox flow battery. *J. Power Sources* **2014**, *268*, 121-128.
- [42] Chao, D.; Zhou, W.; Ye, C.; Zhang, Q.; Chen, Y.; Gu, L.; Davey, K.; Qiao, S. Z., An Electrolytic Zn-MnO₂ Battery for High-Voltage and Scalable Energy Storage. *Angew. Chem., Int. Ed.* **2019**, *58* (23), 7823-7828.
- [43] Ma, D.; Hu, B.; Wu, W.; Liu, X.; Zai, J.; Shu, C.; Tadesse Tsega, T.; Chen, L.; Qian, X.; Liu, T. L., Highly active nanostructured CoS₂/CoS heterojunction electrocatalysts for aqueous polysulfide/iodide redox flow batteries. *Nat Commun* **2019**, *10* (1), 3367.
- [44] Skyllas-Kazacos, M.; Rychick, M.; Robins, R., All-vanadium redox battery. Google Patents: 1988.
- [45] Shi, Y.; Eze, C.; Xiong, B.; He, W.; Zhang, H.; Lim, T. M.; Ukil, A.; Zhao, J., Recent development of membrane for vanadium redox flow battery applications: A review. *Applied Energy* **2019**, *238*, 202-224.
- [46] Sánchez-Díez, E.; Ventosa, E.; Guarnieri, M.; Trovò, A.; Flox, C.; Marcilla, R.; Soavi, F.; Mazur, P.; Aranzabe, E.; Ferret, R., Redox flow batteries: Status and perspective towards sustainable stationary energy storage. *J. Power Sources* **2021**, *481*.
- [47] Singh, V.; Kim, S.; Kang, J.; Byon, H. R., Aqueous organic redox flow batteries. *Nano Research* **2019**, *12* (9), 1988-2001.
- [48] Ding, Y.; Zhang, C.; Zhang, L.; Zhou, Y.; Yu, G., Molecular engineering of organic electroactive materials for redox flow batteries. *Chem Soc Rev* **2018**, *47* (1), 69-103.
- [49] Viswanathan, V.; Crawford, A.; Stephenson, D.; Kim, S.; Wang, W.; Li, B.; Coffey, G.; Thomsen, E.; Graff, G.; Balducci, P.; Kintner-Meyer, M.; Sprenkle, V., Cost and performance model for redox flow batteries. *J. Power Sources* **2014**, *247*, 1040-1051.
- [50] Cheng, L.; Assary, R. S.; Qu, X.; Jain, A.; Ong, S. P.; Rajput, N. N.; Persson, K.; Curtiss, L. A., Accelerating Electrolyte Discovery for Energy Storage with High-Throughput Screening. *The Journal of Physical Chemistry Letters* **2015**, *6* (2), 283-291.

- [51] Gong, K.; Xu, F.; Grunewald, J. B.; Ma, X.; Zhao, Y.; Gu, S.; Yan, Y., All-Soluble All-Iron Aqueous Redox-Flow Battery. *ACS Energy Lett.* **2016**, *1* (1), 89-93.
- [52] Lin, K.; Chen, Q.; Gerhardt, M. R.; Tong, L.; Kim, S. B.; Eisenach, L.; Valle, A. W.; Hardee, D.; Gordon, R. G.; Aziz, M. J.; Marshak, M. P., Alkaline quinone flow battery. *Science* **2015**, *349* (6255), 1529-1532.
- [53] Chen, Y.; Zhou, M.; Xia, Y.; Wang, X.; Liu, Y.; Yao, Y.; Zhang, H.; Li, Y.; Lu, S.; Qin, W.; Wu, X.; Wang, Q., A Stable and High-Capacity Redox Targeting-Based Electrolyte for Aqueous Flow Batteries. *Joule* **2019**, *3* (9), 2255-2267.
- [54] DeBruler, C.; Hu, B.; Moss, J.; Liu, X.; Luo, J.; Sun, Y.; Liu, T. L., Designer Two-Electron Storage Viologen Anolyte Materials for Neutral Aqueous Organic Redox Flow Batteries. *Chem* **2017**, *3* (6), 961-978.
- [55] Hu, B.; DeBruler, C.; Rhodes, Z.; Liu, T. L., Long-Cycling Aqueous Organic Redox Flow Battery (AORFB) toward Sustainable and Safe Energy Storage. *J. Am. Chem. Soc.* **2017**, *139* (3), 1207-1214.
- [56] Hong, J.; Kim, K., Neutral Red and Ferriox as Reversible and Rapid Redox Materials for Redox Flow Batteries. *ChemSusChem* **2018**, *11* (11), 1866-1872.
- [57] Tsitovich, P. B.; Kosswattarachchi, A. M.; Crawley, M. R.; Tittiris, T. Y.; Cook, T. R.; Morrow, J. R., An Fe(III) Aza-macrocyclic Complex as pH-Tunable Catholyte and Anolyte for Redox-Flow Battery Applications. *Chemistry* **2017**.
- [58] Beh, E. S.; De Porcellinis, D.; Gracia, R. L.; Xia, K. T.; Gordon, R. G.; Aziz, M. J., A Neutral pH Aqueous Organic-Organometallic Redox Flow Battery with Extremely High Capacity Retention. *ACS Energy Lett.* **2017**, *2* (3), 639-644.
- [59] Arroyo-Curras, N.; Hall, J. W.; Dick, J. E.; Jones, R. A.; Bard, A. J., An Alkaline Flow Battery Based on the Coordination Chemistry of Iron and Cobalt. *J. Electrochem. Soc.* **2014**, *162* (3), A378-A383.
- [60] Freeman, M. B.; Wang, L.; Jones, D. S.; Bejger, C. M., A cobalt sulfide cluster-based catholyte for aqueous flow battery applications. *J. Mater. Chem. A* **2018**, *6* (44), 21927-21932.
- [61] Wang, H.; Sayed, S. Y.; Zhou, Y.; Olsen, B. C.; Lubner, E. J.; Buriak, J. M., Water-soluble pH-switchable cobalt complexes for aqueous symmetric redox flow batteries. *Chem. Commun.* **2020**, *56* (25), 3605-3608.
- [62] Ding, Y.; Zhang, C.; Zhang, L.; Wei, H.; Li, Y.; Yu, G., Insights into Hydrotropic Solubilization for Hybrid Ion Redox Flow Batteries. *ACS Energy Lett.* **2018**, *3* (11), 2641-2648.
- [63] Robb, B. H.; Farrell, J. M.; Marshak, M. P., Chelated Chromium Electrolyte Enabling High-Voltage Aqueous Flow Batteries. *Joule* **2019**, *3* (10), 2503-2512.
- [64] Jin, S.; Jing, Y.; Kwabi, D. G.; Ji, Y.; Tong, L.; De Porcellinis, D.; Goulet, M.-A.; Pollack, D. A.; Gordon, R. G.; Aziz, M. J., A Water-Miscible Quinone Flow Battery with High Volumetric Capacity and Energy Density. *ACS Energy Lett.* **2019**, 1342-1348.
- [65] Cao, J.; Tao, M.; Chen, H.; Xu, J.; Chen, Z., A highly reversible anthraquinone-based anolyte for alkaline aqueous redox flow batteries. *J. Power Sources* **2018**, *386*, 40-46.
- [66] Kwabi, D. G.; Lin, K.; Ji, Y.; Kerr, E. F.; Goulet, M.-A.; De Porcellinis, D.; Tabor, D. P.; Pollack, D. A.; Aspuru-Guzik, A.; Gordon, R. G.; Aziz, M. J., Alkaline Quinone Flow Battery with Long Lifetime at pH 12. *Joule* **2018**, *2* (9), 1894-1906.
- [67] Janoschka, T.; Martin, N.; Hager, M. D.; Schubert, U. S., An Aqueous Redox-Flow Battery with High Capacity and Power: The TEMPTMA/MV System. *Angew. Chem., Int. Ed.* **2016**, *55* (46), 14427-14430.

- [68] Huang, J.; Yang, Z.; Murugesan, V.; Walter, E.; Hollas, A.; Pan, B.; Assary, R. S.; Shkrob, I. A.; Wei, X.; Zhang, Z., Spatially Constrained Organic Diquat Anolyte for Stable Aqueous Flow Batteries. *ACS Energy Lett.* **2018**, *3* (10), 2533-2538.
- [69] DeBruler, C.; Hu, B.; Moss, J.; Luo, J.; Liu, T. L., A Sulfonate-Functionalized Viologen Enabling Neutral Cation Exchange, Aqueous Organic Redox Flow Batteries toward Renewable Energy Storage. *ACS Energy Lett.* **2018**, *3* (3), 663-668.
- [70] Hu, B.; Tang, Y.; Luo, J.; Grove, G.; Guo, Y.; Liu, T. L., Improved radical stability of viologen anolytes in aqueous organic redox flow batteries. *Chem. Commun.* **2018**, *54* (50), 6871-6874.
- [71] Luo, J.; Hu, B.; Debruler, C.; Liu, T. L., A pi-Conjugation Extended Viologen as a Two-Electron Storage Anolyte for Total Organic Aqueous Redox Flow Batteries. *Angew. Chem., Int. Ed.* **2018**, *57* (1), 231-235.
- [72] Liu, T.; Wei, X.; Nie, Z.; Sprenkle, V.; Wang, W., A Total Organic Aqueous Redox Flow Battery Employing a Low Cost and Sustainable Methyl Viologen Anolyte and 4-HO-TEMPO Catholyte. *Adv. Energy Mater.* **2016**, *6* (3), 1501449.
- [73] Carretero-González, J.; Castillo-Martínez, E.; Armand, M., Highly water-soluble three-redox state organic dyes as bifunctional analytes. *Energy & Environmental Science* **2016**, *9* (11), 3521-3530.
- [74] Lin, K.; Gómez-Bombarelli, R.; Beh, E. S.; Tong, L.; Chen, Q.; Valle, A.; Aspuru-Guzik, A.; Aziz, M. J.; Gordon, R. G., A redox-flow battery with an alloxazine-based organic electrolyte. *Nat. Energy* **2016**, *1* (9), 16102.
- [75] Orita, A.; Verde, M. G.; Sakai, M.; Meng, Y. S., A biomimetic redox flow battery based on flavin mononucleotide. *Nat Commun* **2016**, *7*, 13230.
- [76] Hagemann, T.; Winsberg, J.; Häupler, B.; Janoschka, T.; Gruber, J. J.; Wild, A.; Schubert, U. S., A bipolar nitronyl nitroxide small molecule for an all-organic symmetric redox-flow battery. *NPG Asia Materials* **2017**, *9* (1), e340-e340.
- [77] Zhang, C.; Niu, Z.; Peng, S.; Ding, Y.; Zhang, L.; Guo, X.; Zhao, Y.; Yu, G., Phenothiazine-Based Organic Catholyte for High-Capacity and Long-Life Aqueous Redox Flow Batteries. *Adv Mater* **2019**, e1901052.
- [78] Hollas, A.; Wei, X.; Murugesan, V.; Nie, Z.; Li, B.; Reed, D.; Liu, J.; Sprenkle, V.; Wang, W., A biomimetic high-capacity phenazine-based anolyte for aqueous organic redox flow batteries. *Nat. Energy* **2018**, *3* (6), 508-514.
- [79] Wang, C.; Li, X.; Yu, B.; Wang, Y.; Yang, Z.; Wang, H.; Lin, H.; Ma, J.; Li, G.; Jin, Z., Molecular Design of Fused-Ring Phenazine Derivatives for Long-Cycling Alkaline Redox Flow Batteries. *ACS Energy Lett.* **2020**, 411-417.
- [80] Huskinson, B.; Marshak, M. P.; Suh, C.; Er, S.; Gerhardt, M. R.; Galvin, C. J.; Chen, X.; Aspuru-Guzik, A.; Gordon, R. G.; Aziz, M. J., A metal-free organic-inorganic aqueous flow battery. *Nature* **2014**, *505* (7482), 195-8.
- [81] Tabor, D. P.; Gómez-Bombarelli, R.; Tong, L.; Gordon, R. G.; Aziz, M. J.; Aspuru-Guzik, A., Mapping the frontiers of quinone stability in aqueous media: implications for organic aqueous redox flow batteries. *J. Mater. Chem. A* **2019**, *7* (20), 12833-12841.
- [82] Janoschka, T.; Martin, N.; Martin, U.; Friebe, C.; Morgenstern, S.; Hiller, H.; Hager, M. D.; Schubert, U. S., An aqueous, polymer-based redox-flow battery using non-corrosive, safe, and low-cost materials. *Nature* **2015**, *527* (7576), 78-81.

- [83] Janoschka, T.; Morgenstern, S.; Hiller, H.; Friebe, C.; Wolkersdörfer, K.; Häupler, B.; Hager, M. D.; Schubert, U. S., Synthesis and characterization of TEMPO- and viologen-polymers for water-based redox-flow batteries. *Polymer Chemistry* **2015**, *6* (45), 7801-7811.
- [84] Hagemann, T.; Strumpf, M.; Schröter, E.; Stolze, C.; Grube, M.; Nischang, I.; Hager, M. D.; Schubert, U. S., (2,2,6,6-Tetramethylpiperidin-1-yl)oxyl-Containing Zwitterionic Polymer as Catholyte Species for High-Capacity Aqueous Polymer Redox Flow Batteries. *Chemistry of Materials* **2019**.
- [85] Hofmann, J. D.; Pfanschilling, F. L.; Krawczyk, N.; Geigle, P.; Hong, L.; Schmalisch, S.; Wegner, H. A.; Mollenhauer, D.; Janek, J.; Schröder, D., Quest for Organic Active Materials for Redox Flow Batteries: 2,3-Diaza-anthraquinones and Their Electrochemical Properties. *Chemistry of Materials* **2018**, *30* (3), 762-774.
- [86] Mukhopadhyay, A.; Yang, Y.; Li, Y.; Chen, Y.; Li, H.; Natan, A.; Liu, Y.; Cao, D.; Zhu, H., Mass Transfer and Reaction Kinetic Enhanced Electrode for High-Performance Aqueous Flow Batteries. *Advanced Functional Materials* **2019**.
- [87] Jiang, H. R.; Shyy, W.; Zeng, L.; Zhang, R. H.; Zhao, T. S., Highly efficient and ultra-stable boron-doped graphite felt electrodes for vanadium redox flow batteries. *J. Mater. Chem. A* **2018**, *6* (27), 13244-13253.
- [88] Etesami, M.; Abouzari-Lotf, E.; Sha'rani, S. S.; Miyake, M.; Moozarm Nia, P.; Ripin, A.; Ahmad, A., Self-assembled heteropolyacid on nitrogen-enriched carbon nanofiber for vanadium flow batteries. *Nanoscale* **2018**, *10* (27), 13212-13222.
- [89] Ma, Q.; Zeng, X. X.; Zhou, C.; Deng, Q.; Wang, P. F.; Zuo, T. T.; Zhang, X. D.; Yin, Y. X.; Wu, X.; Chai, L. Y.; Guo, Y. G., Designing High-Performance Composite Electrodes for Vanadium Redox Flow Batteries: Experimental and Computational Investigation. *ACS Appl Mater Interfaces* **2018**, *10* (26), 22381-22388.
- [90] Kim, S.; Choi, J.; Choi, C.; Heo, J.; Kim, D. W.; Lee, J. Y.; Hong, Y. T.; Jung, H. T.; Kim, H. T., Pore-Size-Tuned Graphene Oxide Frameworks as Ion-Selective and Protective Layers on Hydrocarbon Membranes for Vanadium Redox-Flow Batteries. *Nano Lett* **2018**, *18* (6), 3962-3968.
- [91] Shinde, D. B.; Vlassioug, I. V.; Talipov, M. R.; Smirnov, S. N., Exclusively Proton Conductive Membranes Based on Reduced Graphene Oxide Polymer Composites. *ACS Nano* **2019**, *13* (11), 13136-13143.
- [92] Liu, J.; Yu, L.; Cai, X.; Khan, U.; Cai, Z.; Xi, J.; Liu, B.; Kang, F., Sandwiching h-BN Monolayer Films between Sulfonated Poly(ether ether ketone) and Nafion for Proton Exchange Membranes with Improved Ion Selectivity. *ACS Nano* **2019**, *13* (2), 2094-2102.
- [93] Yu, L.; Yu, L.; Wang, L.; Wang, L.; Qiu, X.; Xi, J., Bilayer Designed Hydrocarbon Membranes for All-Climate Vanadium Flow Batteries To Shield Catholyte Degradation and Mitigate Electrolyte Crossover. *ACS Appl Mater Interfaces* **2019**, *11* (14), 13285-13294.
- [94] Yuan, Z.; Liu, X.; Xu, W.; Duan, Y.; Zhang, H.; Li, X., Negatively charged nanoporous membrane for a dendrite-free alkaline zinc-based flow battery with long cycle life. *Nat Commun* **2018**, *9* (1), 3731.
- [95] Qiao, L.; Zhang, H.; Lu, W.; Xiao, C.; Fu, Q.; Li, X.; Vankelecom, I. F. J., Advanced porous membranes with slit-like selective layer for flow battery. *Nano Energy* **2018**, *54*, 73-81.
- [96] Dai, Q.; Liu, Z.; Huang, L.; Wang, C.; Zhao, Y.; Fu, Q.; Zheng, A.; Zhang, H.; Li, X., Thin-film composite membrane breaking the trade-off between conductivity and selectivity for a flow battery. *Nat Commun* **2020**, *11* (1), 13.

- [97] Chang, N.; Yin, Y.; Yue, M.; Yuan, Z.; Zhang, H.; Lai, Q.; Li, X., A Cost-Effective Mixed Matrix Polyethylene Porous Membrane for Long-Cycle High Power Density Alkaline Zinc-Based Flow Batteries. *Advanced Functional Materials* **2019**.
- [98] Wang, C.; Lai, Q.; Xu, P.; Zheng, D.; Li, X.; Zhang, H., Cage-Like Porous Carbon with Superhigh Activity and Br₂⁻-Complex-Entrapping Capability for Bromine-Based Flow Batteries. *Adv Mater* **2017**, *29* (22).
- [99] Navalpotro, P.; Palma, J.; Anderson, M.; Marcilla, R., A Membrane-Free Redox Flow Battery with Two Immiscible Redox Electrolytes. *Angew. Chem., Int. Ed.* **2017**.
- [100] Barton, A. F. M., Solubility parameters. *Chem. Rev.* **1975**, *75* (6), 731-753.
- [101] Takanabe, K., Photocatalytic Water Splitting: Quantitative Approaches toward Photocatalyst by Design. *ACS Catalysis* **2017**, *7* (11), 8006-8022.
- [102] Taheri, A.; Carr, C. R.; Berben, L. A., Electrochemical Methods for Assessing Kinetic Factors in the Reduction of CO₂ to Formate: Implications for Improving Electrocatalyst Design. *ACS Catalysis* **2018**, *8* (7), 5787-5793.
- [103] Fang, G.; Zhou, J.; Pan, A.; Liang, S., Recent Advances in Aqueous Zinc-Ion Batteries. *ACS Energy Lett.* **2018**, 2480-2501.
- [104] Gewirth, A. A.; Varnell, J. A.; DiAscro, A. M., Nonprecious Metal Catalysts for Oxygen Reduction in Heterogeneous Aqueous Systems. *Chem. Rev.* **2018**, *118* (5), 2313-2339.
- [105] Zhu, Y.; Gao, T.; Fan, X.; Han, F.; Wang, C., Electrochemical Techniques for Intercalation Electrode Materials in Rechargeable Batteries. *Accounts of Chemical Research* **2017**, *50* (4), 1022-1031.
- [106] Lee, K. J.; Elgrishi, N.; Kandemir, B.; Dempsey, J. L., Electrochemical and spectroscopic methods for evaluating molecular electrocatalysts. *Nature Reviews Chemistry* **2017**, *1* (5).
- [107] Gandomi, Y. A.; Aaron, D. S.; Houser, J. R.; Daugherty, M. C.; Clement, J. T.; Pezeshki, A. M.; Ertugrul, T. Y.; Moseley, D. P.; Mench, M. M., Critical Review—Experimental Diagnostics and Material Characterization Techniques Used on Redox Flow Batteries. *J. Electrochem. Soc.* **2018**, *165* (5), A970-A1010.
- [108] Liu, Y.; Lu, S.; Wang, H.; Yang, C.; Su, X.; Xiang, Y., An Aqueous Redox Flow Battery with a Tungsten-Cobalt Heteropolyacid as the Electrolyte for both the Anode and Cathode. *Adv. Energy Mater.* **2017**, *7* (8).
- [109] Friedl, J.; Lebedeva, M. A.; Porfyrakis, K.; Stimming, U.; Chamberlain, T. W., All-Fullerene-Based Cells for Nonaqueous Redox Flow Batteries. *J. Am. Chem. Soc.* **2018**, *140* (1), 401-405.
- [110] Hirschorn, B.; Orazem, M. E.; Tribollet, B.; Vivier, V.; Frateur, I.; Musiani, M., Determination of effective capacitance and film thickness from constant-phase-element parameters. *Electrochim. Acta* **2010**, *55* (21), 6218-6227.
- [111] Hsu, C. H.; Mansfeld, F., Technical Note: Concerning the Conversion of the Constant Phase Element Parameter Y₀ into a Capacitance. *Corrosion* **2001**, *57* (09), 2.
- [112] Brug, G. J.; van den Eeden, A. L. G.; Sluyters-Rehbach, M.; Sluyters, J. H., The analysis of electrode impedances complicated by the presence of a constant phase element. *Journal of Electroanalytical Chemistry and Interfacial Electrochemistry* **1984**, *176* (1), 275-295.
- [113] Orazem, M. E.; Tribollet, B., *Electrochemical impedance spectroscopy*. John Wiley & Sons: 2017.
- [114] Bard, A.; Faulkner, L., *Electrochemical Methods: Fundamentals and Applications*. John Wiley & Sons, Inc: 2001.
- [115] Zoski, C. G., *Handbook of electrochemistry*. Elsevier: 2006.

- [116] Yuan, X. Z.; Song, C.; Platt, A.; Zhao, N.; Wang, H.; Li, H.; Fatih, K.; Jang, D., A review of all - vanadium redox flow battery durability: Degradation mechanisms and mitigation strategies. *International Journal of Energy Research* **2019**.
- [117] Gong, K.; Ma, X.; Conforti, K. M.; Kuttler, K. J.; Grunewald, J. B.; Yeager, K. L.; Bazant, M. Z.; Gu, S.; Yan, Y., A zinc–iron redox-flow battery under \$100 per kW h of system capital cost. *Energy & Environmental Science* **2015**, *8* (10), 2941-2945.
- [118] Li, Z.; Lu, Y.-C., Redox Flow Batteries: Want More Electrons? Go Organic! *Chem* **2018**, *4* (9), 2020-2021.
- [119] Doris, S. E.; Ward, A. L.; Baskin, A.; Frischmann, P. D.; Gavvalapalli, N.; Chénard, E.; Sevov, C. S.; Prendergast, D.; Moore, J. S.; Helms, B. A., Macromolecular Design Strategies for Preventing Active-Material Crossover in Non-Aqueous All-Organic Redox-Flow Batteries. *Angewandte Chemie International Edition* **2017**, *56* (6), 1595-1599.
- [120] Kuleshova, L. N.; Hofmann, D. W. M.; Boese, R., Lattice energy calculation – A quick tool for screening of cocrystals and estimation of relative solubility. Case of flavonoids. *Chemical Physics Letters* **2013**, *564*, 26-32.
- [121] Schmid, R., Recent Advances in the Description of the Structure of Water, the Hydrophobic Effect, and the Like-Dissolves-Like Rule. In *Highlights in Solute-Solvent Interactions*, Linert, W., Ed. Springer Vienna: Vienna, 2002; pp 59-90.
- [122] Polarity of Organic Compounds.
- [123] Hu, B.; Luo, J.; Hu, M.; Yuan, B.; Liu, T. L., A pH-Neutral, Metal-Free Aqueous Organic Redox Flow Battery Employing an Ammonium Anthraquinone Anolyte. *Angewandte Chemie* **2019**, *0* (0).
- [124] Han, K. S.; Rajput, N. N.; Vijayakumar, M.; Wei, X.; Wang, W.; Hu, J.; Persson, K. A.; Mueller, K. T., Preferential Solvation of an Asymmetric Redox Molecule. *The Journal of Physical Chemistry C* **2016**, *120* (49), 27834-27839.
- [125] Teoh, W. H.; Mammucari, R.; Foster, N. R., Solubility of organometallic complexes in supercritical carbon dioxide: A review. *Journal of Organometallic Chemistry* **2013**, *724*, 102-116.
- [126] Sevov, C. S.; Fisher, S. L.; Thompson, L. T.; Sanford, M. S., Mechanism-Based Development of a Low-Potential, Soluble, and Cyclable Multielectron Anolyte for Nonaqueous Redox Flow Batteries. *J. Am. Chem. Soc.* **2016**, *138* (47), 15378-15384.
- [127] Luo, J.; Hu, B.; Debruler, C.; Bi, Y.; Zhao, Y.; Yuan, B.; Hu, M.; Wu, W.; Liu, T. L., Unprecedented Capacity and Stability of Ammonium Ferrocyanide Catholyte in pH Neutral Aqueous Redox Flow Batteries. *Joule* **2019**, *3* (1), 149-163.
- [128] Wedege, K.; Drazevic, E.; Konya, D.; Bientien, A., Organic Redox Species in Aqueous Flow Batteries: Redox Potentials, Chemical Stability and Solubility. *Sci Rep* **2016**, *6*, 39101.
- [129] Han, C.; Li, H.; Shi, R.; Zhang, T.; Tong, J.; Li, J.; Li, B., Organic quinones towards advanced electrochemical energy storage: recent advances and challenges. *J. Mater. Chem. A* **2019**.
- [130] Burgess, M.; Moore, J. S.; Rodriguez-Lopez, J., Redox Active Polymers as Soluble Nanomaterials for Energy Storage. *Acc Chem Res* **2016**, *49* (11), 2649-2657.
- [131] Montoto, E. C.; Nagarjuna, G.; Hui, J.; Burgess, M.; Sekerak, N. M.; Hernandez-Burgos, K.; Wei, T. S.; Kneer, M.; Grolman, J.; Cheng, K. J.; Lewis, J. A.; Moore, J. S.; Rodriguez-Lopez, J., Redox Active Colloids as Discrete Energy Storage Carriers. *J. Am. Chem. Soc.* **2016**, *138* (40), 13230-13237.
- [132] Luo, J.; Wu, W.; Debruler, C.; Hu, B.; Hu, M.; Liu, T. L., A 1.51 V pH neutral redox flow battery towards scalable energy storage. *J. Mater. Chem. A* **2019**, *7* (15), 9130-9136.

- [133] Wei, X.; Xu, W.; Vijayakumar, M.; Cosimbescu, L.; Liu, T.; Sprenkle, V.; Wang, W., TEMPO-based catholyte for high-energy density nonaqueous redox flow batteries. *Adv Mater* **2014**, *26* (45), 7649-53.
- [134] Chai, J.; Lashgari, A.; Wang, X.; Williams, C. K.; Jiang, J. J., All-PEGylated redox-active metal-free organic molecules in non-aqueous redox flow battery. *J. Mater. Chem. A* **2020**.
- [135] Yan, Y.; Robinson, S. G.; Sigman, M. S.; Sanford, M. S., Mechanism-Based Design of a High-Potential Catholyte Enables a 3.2 V All-Organic Nonaqueous Redox Flow Battery. *J. Am. Chem. Soc.* **2019**, *141* (38), 15301-15306.
- [136] Tian, Y.; Wu, K. H.; Cao, L.; Saputera, W. H.; Amal, R.; Wang, D. W., Unlocking high-potential non-persistent radical chemistry for semi-aqueous redox batteries. *Chem. Commun.* **2019**, *55* (15), 2154-2157.
- [137] Hogue, R. W.; Armstrong, C. G.; Toghill, K. E., Dithiolene Complexes of First-Row Transition Metals for Symmetric Nonaqueous Redox Flow Batteries. *ChemSusChem* **2019**, *12* (19), 4506-4515.
- [138] Sevov, C. S.; Brooner, R. E.; Chenard, E.; Assary, R. S.; Moore, J. S.; Rodriguez-Lopez, J.; Sanford, M. S., Evolutionary Design of Low Molecular Weight Organic Anolyte Materials for Applications in Nonaqueous Redox Flow Batteries. *J. Am. Chem. Soc.* **2015**, *137* (45), 14465-72.
- [139] Antoni, P. W.; Bruckhoff, T.; Hansmann, M. M., Organic Redox Systems Based on Pyridinium-Carbene Hybrids. *J. Am. Chem. Soc.* **2019**, *141* (24), 9701-9711.
- [140] Tao, M.; Wang, Z.; Gong, J.; Hao, H.; Wang, J., Determination of the Solubility, Dissolution Enthalpy, and Entropy of Pioglitazone Hydrochloride (Form II) in Different Pure Solvents. *Industrial & Engineering Chemistry Research* **2013**, *52* (8), 3036-3041.
- [141] Mukhopadhyay, A.; Zhao, H.; Li, B.; Hamel, J.; Yang, Y.; Cao, D.; Natan, A.; Zhu, H., Abundant Organic Dye as an Anolyte for Aqueous Flow Battery with Multi-Electron Transfer. *ACS Applied Energy Materials* **2019**.
- [142] Miao, L.; Liu, L.; Shang, Z.; Li, Y.; Lu, Y.; Cheng, F.; Chen, J., The structure-electrochemical property relationship of quinone electrodes for lithium-ion batteries. *Phys Chem Chem Phys* **2018**, *20* (19), 13478-13484.
- [143] Sanchez-Lengeling, B.; Aspuru-Guzik, A., Inverse molecular design using machine learning: Generative models for matter engineering. *Science* **2018**, *361* (6400), 360-365.
- [144] Milshtein, J. D.; Kaur, A. P.; Casselman, M. D.; Kowalski, J. A.; Modekrutti, S.; Zhang, P. L.; Harsha Attanayake, N.; Elliott, C. F.; Parkin, S. R.; Risko, C.; Brushett, F. R.; Odom, S. A., High current density, long duration cycling of soluble organic active species for non-aqueous redox flow batteries. *Energy Environ. Sci.* **2016**, *9* (11), 3531-3543.
- [145] Elgrishi, N.; Rountree, K. J.; McCarthy, B. D.; Rountree, E. S.; Eisenhart, T. T.; Dempsey, J. L., A Practical Beginner's Guide to Cyclic Voltammetry. *Journal of Chemical Education* **2018**, *95* (2), 197-206.
- [146] Heinze, J., Cyclic Voltammetry—"Electrochemical Spectroscopy". *New Analytical Methods* (25). *Angewandte Chemie International Edition in English* **1984**, *23* (11), 831-847.
- [147] Diamond, P. S.; Denman, R. F., *Laboratory Techniques in Chemistry and Biochemistry*. Butterworths: 1973.
- [148] Brownson, D. A.; Banks, C. E., Interpreting electrochemistry. In *The Handbook of Graphene Electrochemistry*, Springer: 2014; pp 23-77.

- [149] Matsuda, H.; Ayabe, Y., Zur Theorie der Randles-Sevcik'schen Kathodenstrahl-Polarographie. *Zeitschrift für Elektrochemie, Berichte der Bunsengesellschaft für physikalische Chemie* **1955**, *59* (6), 494-503.
- [150] Ozkan, S. A.; Kauffmann, J.-M.; Zuman, P., Electroanalysis in biomedical and pharmaceutical sciences. *Voltammetry, Amperometry, Biosensors, Applications* **2015**.
- [151] Sawant, T. V.; McKone, J. R., Flow Battery Electroanalysis. 2. Influence of Surface Pretreatment on Fe(III/II) Redox Chemistry at Carbon Electrodes. *The Journal of Physical Chemistry C* **2019**, *123* (1), 144-152.
- [152] Wei, C.; Rao, R. R.; Peng, J.; Huang, B.; Stephens, I. E. L.; Risch, M.; Xu, Z. J.; Shao-Horn, Y., Recommended Practices and Benchmark Activity for Hydrogen and Oxygen Electrocatalysis in Water Splitting and Fuel Cells. *Advanced Materials* **2019**, *31* (31), 1806296.
- [153] Li, D.; Wang, C.; Tripkovic, D.; Sun, S.; Markovic, N. M.; Stamenkovic, V. R., Surfactant Removal for Colloidal Nanoparticles from Solution Synthesis: The Effect on Catalytic Performance. *ACS Catalysis* **2012**, *2* (7), 1358-1362.
- [154] van der Vliet, D.; Strmcnik, D. S.; Wang, C.; Stamenkovic, V. R.; Markovic, N. M.; Koper, M. T. M., On the importance of correcting for the uncompensated Ohmic resistance in model experiments of the Oxygen Reduction Reaction. *Journal of Electroanalytical Chemistry* **2010**, *647* (1), 29-34.
- [155] Izquierdo, J.; Kranz, C., Electrochemical techniques for investigating redox active macromolecules. *European Polymer Journal* **2016**, *83*, 428-449.
- [156] Hendriks, K. H.; Robinson, S. G.; Braten, M. N.; Sevov, C. S.; Helms, B. A.; Sigman, M. S.; Minter, S. D.; Sanford, M. S., High-Performance Oligomeric Catholytes for Effective Macromolecular Separation in Nonaqueous Redox Flow Batteries. *ACS Central Science* **2018**, *4* (2), 189-196.
- [157] El-Deab, M. S.; Ohsaka, T., Quasi-reversible two-electron reduction of oxygen at gold electrodes modified with a self-assembled submonolayer of cysteine. *Electrochemistry Communications* **2003**, *5* (3), 214-219.
- [158] Koryta, J.; Dvorak, J.; Kavan, L., *Principles of Electrochemistry*. Wiley: 1993.
- [159] Lee, K. J.; Gruninger, C. T.; Lodaya, K. M.; Qadeer, S.; Griffith, B. E.; Dempsey, J. L., Analysis of multi-electron, multi-step homogeneous catalysis by rotating disc electrode voltammetry: theory, application, and obstacles. *Analyst* **2020**, *145* (4), 1258-1278.
- [160] Rice, R. J.; Pontikos, N. M.; McCreery, R. L., Quantitative correlations of heterogeneous electron-transfer kinetics with surface properties of glassy carbon electrodes. *Journal of the American Chemical Society* **1990**, *112* (12), 4617-4622.
- [161] Kneten, K. R.; McCreery, R. L., Effects of redox system structure on electron-transfer kinetics at ordered graphite and glassy carbon electrodes. *Anal. Chem.* **1992**, *64* (21), 2518-2524.
- [162] Cook, S. K.; Horrocks, B. R., Heterogeneous Electron-Transfer Rates for the Reduction of Viologen Derivatives at Platinum and Bismuth Electrodes in Acetonitrile. *ChemElectroChem* **2017**, *4* (2), 320-331.
- [163] Wightman, R. M.; Wipf, D. O., High-speed cyclic voltammetry. *Accounts of Chemical Research* **1990**, *23* (3), 64-70.
- [164] Wipf, D. O.; Wightman, R. M., Submicrosecond measurements with cyclic voltammetry. *Anal. Chem.* **1988**, *60* (22), 2460-2464.
- [165] Wipf, D. O.; Wightman, R. M., Voltammetry with microvoltammetric electrodes in resistive solvents under linear diffusion conditions. *Anal. Chem.* **1990**, *62* (2), 98-102.

- [166] Andrieux, C. P.; Garreau, D.; Hapiot, P.; Pinson, J.; Savéant, J. M., Fast sweep cyclic voltammetry at ultra-microelectrodes: Evaluation of the method for fast electron-transfer kinetic measurements. *Journal of Electroanalytical Chemistry and Interfacial Electrochemistry* **1988**, *243* (2), 321-335.
- [167] Wipf, D. O.; Kristensen, E. W.; Deakin, M. R.; Wightman, R. M., Fast-scan cyclic voltammetry as a method to measure rapid heterogeneous electron-transfer kinetics. *Anal. Chem.* **1988**, *60* (4), 306-310.
- [168] Fortgang, P.; Amatore, C.; Maisonhaute, E.; Schöllhorn, B., Microchip for ultrafast voltammetry. *Electrochemistry Communications* **2010**, *12* (7), 897-900.
- [169] Robinson, R. S.; McCreery, R. L., Submicrosecond spectroelectrochemistry applied to chlorpromazine cation radical charge transfer reactions. *Journal of Electroanalytical Chemistry and Interfacial Electrochemistry* **1985**, *182* (1), 61-72.
- [170] Forster, R. J.; Faulkner, L. R., Electrochemistry of Spontaneously Adsorbed Monolayers. Equilibrium Properties and Fundamental Electron Transfer Characteristics. *Journal of the American Chemical Society* **1994**, *116* (12), 5444-5452.
- [171] Wang, W.; Fan, X.; Liu, J.; Yan, C.; Zeng, C., Temperature-related reaction kinetics of the vanadium(iv)/(v) redox couple in acidic solutions. *RSC Advances* **2014**, *4* (61), 32405-32411.
- [172] Nicholson, R. S., Theory and Application of Cyclic Voltammetry for Measurement of Electrode Reaction Kinetics. *Anal. Chem.* **1965**, *37* (11), 1351-1355.
- [173] Luo, J.; Sam, A.; Hu, B.; DeBruler, C.; Wei, X.; Wang, W.; Liu, T. L., Unraveling pH dependent cycling stability of ferricyanide/ferrocyanide in redox flow batteries. *Nano Energy* **2017**, *42*, 215-221.
- [174] Lavagnini, I.; Antiochia, R.; Magno, F., An Extended Method for the Practical Evaluation of the Standard Rate Constant from Cyclic Voltammetric Data. *Electroanalysis* **2004**, *16* (6), 505-506.
- [175] Rheinländer, P. J.; Herranz, J.; Durst, J.; Gasteiger, H. A., Kinetics of the Hydrogen Oxidation/Evolution Reaction on Polycrystalline Platinum in Alkaline Electrolyte Reaction Order with Respect to Hydrogen Pressure. *J. Electrochem. Soc.* **2014**, *161* (14), F1448-F1457.
- [176] Ding, Y.; Zhao, Y.; Li, Y.; Goodenough, J. B.; Yu, G., A high-performance all-metallocene-based, non-aqueous redox flow battery. *Energy Environ. Sci.* **2017**, *10* (2), 491-497.
- [177] Mirkin, M. V.; Bard, A. J., Simple analysis of quasi-reversible steady-state voltammograms. *Anal. Chem.* **1992**, *64* (19), 2293-2302.
- [178] Aaron, D. S.; Liu, Q.; Tang, Z.; Grim, G. M.; Papandrew, A. B.; Turhan, A.; Zawodzinski, T. A.; Mench, M. M., Dramatic performance gains in vanadium redox flow batteries through modified cell architecture. *J. Power Sources* **2012**, *206*, 450-453.
- [179] Aaron, D.; Tang, Z.; Papandrew, A. B.; Zawodzinski, T. A., Polarization curve analysis of all-vanadium redox flow batteries. *Journal of Applied Electrochemistry* **2011**, *41* (10), 1175.
- [180] Milshtein, J. D.; Tenny, K. M.; Barton, J. L.; Drake, J.; Darling, R. M.; Brushett, F. R., Quantifying Mass Transfer Rates in Redox Flow Batteries. *J. Electrochem. Soc.* **2017**, *164* (11), E3265-E3275.
- [181] Tucker, M. C.; Phillips, A.; Weber, A. Z., All-Iron Redox Flow Battery Tailored for Off-Grid Portable Applications. *ChemSusChem* **2015**, *8* (23), 3996-4004.
- [182] Liu, W.; Liu, Y.; Zhang, H.; Xie, C.; Shi, L.; Zhou, Y. G.; Li, X., A highly stable neutral viologen/bromine aqueous flow battery with high energy and power density. *Chem. Commun.* **2019**, *55* (33), 4801-4804.

- [183] Potash, R. A.; McKone, J. R.; Conte, S.; Abruña, H. D., On the Benefits of a Symmetric Redox Flow Battery. *J. Electrochem. Soc.* **2015**, *163* (3), A338-A344.
- [184] Hendriks, K. H.; Sevov, C. S.; Cook, M. E.; Sanford, M. S., Multielectron Cycling of a Low-Potential Anolyte in Alkali Metal Electrolytes for Nonaqueous Redox Flow Batteries. *ACS Energy Lett.* **2017**, 2430-2435.
- [185] Ma, T.; Pan, Z.; Miao, L.; Chen, C.; Han, M.; Shang, Z.; Chen, J., Porphyrin-Based Symmetric Redox-Flow Batteries towards Cold-Climate Energy Storage. *Angew. Chem., Int. Ed.* **2018**, *57* (12), 3158-3162.
- [186] VanGelder, L. E.; Kosswattaarachchi, A. M.; Forrestel, P. L.; Cook, T. R.; Matson, E. M., Polyoxovanadate-alkoxide clusters as multi-electron charge carriers for symmetric non-aqueous redox flow batteries. *Chem Sci* **2018**, *9* (6), 1692-1699.
- [187] Duan, W.; Vemuri, R. S.; Milshtein, J. D.; Laramie, S.; Dmello, R. D.; Huang, J.; Zhang, L.; Hu, D.; Vijayakumar, M.; Wang, W.; Liu, J.; Darling, R. M.; Thompson, L.; Smith, K.; Moore, J. S.; Brushett, F. R.; Wei, X., A symmetric organic-based nonaqueous redox flow battery and its state of charge diagnostics by FTIR. *J. Mater. Chem. A* **2016**, *4* (15), 5448-5456.
- [188] Cabrera, P. J.; Yang, X.; Suttill, J. A.; Brooner, R. E. M.; Thompson, L. T.; Sanford, M. S., Evaluation of Tris-Bipyridine Chromium Complexes for Flow Battery Applications: Impact of Bipyridine Ligand Structure on Solubility and Electrochemistry. *Inorg. Chem.* **2015**, *54* (21), 10214-10223.
- [189] Pratt, H. D.; Hudak, N. S.; Fang, X.; Anderson, T. M., A polyoxometalate flow battery. *J. Power Sources* **2013**, *236*, 259-264.
- [190] Winsberg, J.; Stolze, C.; Muench, S.; Liedl, F.; Hager, M. D.; Schubert, U. S., TEMPO/Phenazine Combi-Molecule: A Redox-Active Material for Symmetric Aqueous Redox-Flow Batteries. *ACS Energy Lett.* **2016**, *1* (5), 976-980.
- [191] Janoschka, T.; Friebe, C.; Hager, M. D.; Martin, N.; Schubert, U. S., An Approach Toward Replacing Vanadium: A Single Organic Molecule for the Anode and Cathode of an Aqueous Redox-Flow Battery. *ChemistryOpen* **2017**, *6* (2), 216-220.
- [192] Tsitovich, P. B.; Kosswattaarachchi, A. M.; Crawley, M. R.; Tittiris, T. Y.; Cook, T. R.; Morrow, J. R., An FeIII Azamacrocyclic Complex as a pH-Tunable Catholyte and Anolyte for Redox-Flow Battery Applications. *Chem.: Eur. J.* **2017**, *23* (61), 15327-15331.
- [193] Schmidt, V. A.; Hoyt, J. M.; Margulieux, G. W.; Chirik, P. J., Cobalt-Catalyzed $[2\pi + 2\pi]$ Cycloadditions of Alkenes: Scope, Mechanism, and Elucidation of Electronic Structure of Catalytic Intermediates. *Journal of the American Chemical Society* **2015**, *137* (24), 7903-7914.
- [194] Friedfeld, M. R.; Shevlin, M.; Margulieux, G. W.; Campeau, L.-C.; Chirik, P. J., Cobalt-Catalyzed Enantioselective Hydrogenation of Minimally Functionalized Alkenes: Isotopic Labeling Provides Insight into the Origin of Stereoselectivity and Alkene Insertion Preferences. *Journal of the American Chemical Society* **2016**, *138* (10), 3314-3324.
- [195] Krautwald, S.; Bezdek, M. J.; Chirik, P. J., Cobalt-Catalyzed 1,1-Diboration of Terminal Alkynes: Scope, Mechanism, and Synthetic Applications. *Journal of the American Chemical Society* **2017**, *139* (10), 3868-3875.
- [196] Schonbuch, G.; Streckas, T., Oxidation of a mixed spin cobalt (II) complex. *Inorg. Nucl. Chem. Lett.* **1977**, *13* (11), 591-593.
- [197] Araujo, C. M.; Doherty, M. D.; Konezny, S. J.; Luca, O. R.; Usyatinsky, A.; Grade, H.; Lobkovsky, E.; Soloveichik, G. L.; Crabtree, R. H.; Batista, V. S., Tuning redox potentials of bis(imino)pyridine cobalt complexes: an experimental and theoretical study involving solvent and ligand effects. *Dalton Trans* **2012**, *41* (12), 3562-73.

- [198] Armstrong, C. G.; Toghill, K. E., Cobalt(II) complexes withazole-pyridine type ligands for non-aqueous redox-flow batteries: Tunable electrochemistry via structural modification. *J. Power Sources* **2017**, *349*, 121-129.
- [199] Stauber, J. M.; Zhang, S.; Gvozdk, N.; Jiang, Y.; Avena, L.; Stevenson, K. J.; Cummins, C. C., Cobalt and Vanadium Trimetaphosphate Polyanions: Synthesis, Characterization, and Electrochemical Evaluation for Non-aqueous Redox-Flow Battery Applications. *J. Am. Chem. Soc.* **2018**, *140* (2), 538-541.
- [200] Kosswattaarachchi, A. M.; Cook, T. R., Concentration-dependent charge-discharge characteristics of non-aqueous redox flow battery electrolyte combinations. *Electrochim. Acta* **2018**, *261*, 296-306.
- [201] Benazzi, E.; Cristino, V.; Caramori, S.; Meda, L.; Boaretto, R.; Bignoz, C. A., Electrochemical characterization of polypyridine iron(II) and cobalt(II) complexes for organic redox flow batteries. *Polyhedron* **2018**, *140*, 99-108.
- [202] Yang, C.; Nikiforidis, G.; Park, J. Y.; Choi, J.; Luo, Y.; Zhang, L.; Wang, S.-C.; Chan, Y.-T.; Lim, J.; Hou, Z.; Baik, M.-H.; Lee, Y.; Byon, H. R., Designing Redox-Stable Cobalt-Polypyridyl Complexes for Redox Flow Batteries: Spin-Crossover Delocalizes Excess Charge. *Adv. Energy Mater.* **2018**, *8* (14), 1702897.
- [203] Xing, X.; Zhang, D.; Li, Y., A non-aqueous all-cobalt redox flow battery using 1,10-phenanthrolinecobalt(II) hexafluorophosphate as active species. *J. Power Sources* **2015**, *279*, 205-209.
- [204] Evans, D. F., 400. The determination of the paramagnetic susceptibility of substances in solution by nuclear magnetic resonance. *J. Chem. Soc.* **1959**, (0), 2003-2005.
- [205] de Bruin, B.; Bill, E.; Bothe, E.; Weyhermüller, T.; Wieghardt, K., Molecular and Electronic Structures of Bis(pyridine-2,6-diimine)metal Complexes [ML₂](PF₆)_n (n = 0, 1, 2, 3; M = Mn, Fe, Co, Ni, Cu, Zn). *Inorg. Chem.* **2000**, *39* (13), 2936-2947.
- [206] Ranganathan, S.; Kuo, T.-C.; McCreery, R. L., Facile Preparation of Active Glassy Carbon Electrodes with Activated Carbon and Organic Solvents. *Anal. Chem.* **1999**, *71* (16), 3574-3580.
- [207] McCreery, R. L.; Cline, K. K.; McDermott, C. A.; McDermott, M. T., Control of reactivity at carbon electrode surfaces. *Colloid. Surf. A, Physicochem. Eng. Asp.* **1994**, *93*, 211-219.
- [208] X-Ray Crystallography: A Fast, First-Resort Analytical Tool. In *Progress in Inorganic Chemistry*, pp 1-19.
- [209] Sheldrick, G., SHELXT - Integrated space-group and crystal-structure determination. *Acta Crystallographica Section A* **2015**, *71* (1), 3-8.
- [210] Laursen, J. B.; Nielsen, J., Phenazine Natural Products: Biosynthesis, Synthetic Analogues, and Biological Activity. *Chem. Rev.* **2004**, *104* (3), 1663-1686.
- [211] Lim, H.-D.; Lee, B.; Zheng, Y.; Hong, J.; Kim, J.; Gwon, H.; Ko, Y.; Lee, M.; Cho, K.; Kang, K., Rational design of redox mediators for advanced Li-O₂ batteries. *Nat. Energy* **2016**, *1* (6), 16066.
- [212] Kwon, G.; Lee, S.; Hwang, J.; Shim, H.-S.; Lee, B.; Lee, M. H.; Ko, Y.; Jung, S.-K.; Ku, K.; Hong, J.; Kang, K., Multi-redox Molecule for High-Energy Redox Flow Batteries. *Joule* **2018**, *2* (9), 1771-1782.
- [213] Kwon, G.; Lee, K.; Lee, M. H.; Lee, B.; Lee, S.; Jung, S.-K.; Ku, K.; Kim, J.; Park, S. Y.; Kwon, J. E.; Kang, K., Bio-inspired Molecular Redesign of a Multi-redox Catholyte for High-Energy Non-aqueous Organic Redox Flow Batteries. *Chem* **2019**, *5* (10), 2642-2656.

- [214] Wang, R.; Okajima, T.; Kitamura, F.; Kawauchi, S.; Matsumoto, N.; Thiemann, T.; Mataka, S.; Ohsaka, T., Catalytic Reduction of O₂ by Pyrazine Derivatives. *The Journal of Physical Chemistry A* **2004**, *108* (11), 1891-1899.
- [215] Pang, S.; Wang, X.; Wang, P.; Ji, Y., Biomimetic Amino Acid Functionalized Phenazine Flow Batteries with Long Lifetime at Near-Neutral pH. *Angew. Chem., Int. Ed.* **2021**, *60* (10), 5289-5298.
- [216] Wu, J.; Wang, Y.; Zhang, D.; Hou, B., Studies on the electrochemical reduction of oxygen catalyzed by reduced graphene sheets in neutral media. *J. Power Sources* **2011**, *196* (3), 1141-1144.
- [217] Wang, C.; Yang, Z.; Wang, Y.; Zhao, P.; Yan, W.; Zhu, G.; Ma, L.; Yu, B.; Wang, L.; Li, G.; Liu, J.; Jin, Z., High-Performance Alkaline Organic Redox Flow Batteries Based on 2-Hydroxy-3-carboxy-1,4-naphthoquinone. *ACS Energy Lett.* **2018**, *3* (10), 2404-2409.
- [218] Zhang, Y.; Cao, J.; Chen, Z.; Xu, J.; Yu, C., An organic-based aqueous hybrid flow battery with high power and long cycle life: a tetrapyrrophenazine/ferrocyanide system. *J. Mater. Chem. A* **2020**.
- [219] Murali, A.; Nirmalchandar, A.; Krishnamoorthy, S.; Hooper-Burkhardt, L.; Yang, B.; Soloveichik, G.; Prakash, G. K. S.; Narayanan, S. R., Understanding and Mitigating Capacity Fade in Aqueous Organic Redox Flow Batteries. *J. Electrochem. Soc.* **2018**, *165* (7), A1193-A1203.
- [220] Xu, Y.; Wen, Y. H.; Cheng, J.; Cao, G. P.; Yang, Y. S. In *Electrochemical reaction mechanism of tiron in acidic aqueous solution*, Advanced Materials Research, Trans Tech Publ: 2012; pp 1730-1735.
- [221] Goulet, M. A.; Tong, L.; Pollack, D. A.; Tabor, D. P.; Odom, S. A.; Aspuru-Guzik, A.; Kwan, E. E.; Gordon, R. G.; Aziz, M. J., Extending the Lifetime of Organic Flow Batteries via Redox State Management. *J. Am. Chem. Soc.* **2019**, *141* (20), 8014-8019.
- [222] Orita, A.; Verde, M. G.; Sakai, M.; Meng, Y. S., The impact of pH on side reactions for aqueous redox flow batteries based on nitroxyl radical compounds. *J. Power Sources* **2016**, *321*, 126-134.
- [223] de la Cruz, C.; Molina, A.; Patil, N.; Ventosa, E.; Marcilla, R.; Mavrandonakis, A., New insights into phenazine-based organic redox flow batteries by using high-throughput DFT modelling. *Sustainable Energy & Fuels* **2020**, *4* (11), 5513-5521.